

ABSTRACT

O'BRIEN, CHRISTOPHER JOHN. First-Principles Informed Thermodynamics of CRUD Deposition. (Under the direction of Donald W. Brenner.)

The recent emphasis in the United States on developing abundant domestic sources of energy, together with an increasing awareness of the environmental hazards of fossil fuels, has led to a fresh look at the challenges of nuclear energy within the science and engineering community. One of these challenges is controlling the precipitation of porous oxide deposits onto the nuclear fuel rod cladding from the primary coolant during operation of pressurized light-water reactors (PWRs). These deposits, called CRUD (an acronym for Chalk River Unidentified Deposits), are a major concern to reactor operation because they reduce fuel lifetime and efficiency by reducing heat transfer to the coolant, promote corrosion, and depress neutron flux. This dissertation provides fundamental insights into the process by which CRUD is formed in PWRs by providing a framework linking the results of first-principles calculations to experimental data. The technique developed to facilitate the investigation is referred to as Density Functional Theory (DFT) referenced semi-empirical thermodynamics; It links 0K first-principles calculations with high temperature thermodynamics by redefining the reference chemical potentials of the constituent elements. The technique permits aqueous chemistry to be incorporated into thermodynamic calculations and allows for the prediction of temperature and pressure dependent free energies of materials that are experimentally inaccessible or have not yet been measured. The ability to extend accurate first-principles calculations to high temperatures and aqueous environments allows the stability of crystal surfaces, calculated with DFT techniques, to be predicted at conditions representative of an operating PWR. Accurate values of surface energies are used in fulfilling the principal goal of this dissertation, which is to investigate the aqueous thermodynamics of formation of nickel oxide (NiO) and nickel ferrite (NiFe₂O₄) crystallites as representative CRUD components. Specifically, this dissertation investigates the thermodynamics of the homogeneous nucleation of crystallites and proposes a mechanism for their agglomeration. This work also contributes to a more complete

understanding of CRUD by generating improved thermodynamic data to enable modeling of the incorporation of boron into CRUD through the formation of Bonaccordite (Ni_2FeBO_5) which has formed in PWRs operating at high-power conditions.

© Copyright 2013 Christopher J. O'Brien

All Rights Reserved

First-Principles Informed Thermodynamics of CRUD Deposition

by
Christopher John O'Brien

A dissertation submitted to the Graduate Faculty of
North Carolina State University
in partial fulfillment of the
requirements for the Degree of
Doctor of Philosophy

Materials Science and Engineering

Raleigh, North Carolina

2013

APPROVED BY:

Dr. Donald W. Brenner
Committee Chair

Dr. Douglas L. Irving
Committee Co-Chair

Dr. K. L. Murty

Dr. John-Paul Maria

DEDICATION

In honor of my grandparents...

Carmello Cirincione "Pap" a source of indefatigable encouragement

...and to the memory of those who will miss my graduation

Caroline O'Brien "Nana"

Marianne G. Cirincione "Mag"

John O'Brien "Grandpa"

BIOGRAPHY

The author was born and raised in a suburb of Pittsburgh, Pennsylvania. After high school, he attended The Pennsylvania State University at the turn of the millennium. Inspired by the futurist Erick K. Drexler's "The Engines of Creation" he was motivated to enter the new field of nanotechnology. He completed a thesis applying nanostructured thin films to humidity detection to earn his bachelor's degree, with honors, in Engineering Science in the Spring of 2004.

Chris then went on to earn a Master's degree in Materials Science and Engineering at Rensselaer Polytechnic Institute in the Spring of 2006 by completing a thesis involving the synthesis of magnetic nanoparticles.

He returned to Penn State to be involved in the computer simulation of the mechanical properties of materials at the nanoscale. This experience marked a turning point in his career where he shifted from the experimental study to computer modeling of materials.

He then furthered his knowledge of first-principles modeling of materials while earning a doctorate in Materials Science and Engineering at the North Carolina State University.

ACKNOWLEDGMENTS

In chronological order, I would like to thank certain individuals who helped me to advance my career:

Dr. Akhlesh Lakhtakia (Penn State University, Engineering Science and Mechanics), my undergraduate academic advisor and the man who taught me the power of numerical methods.

Dr. Mutsuhiro Shima (formerly of Rensselaer Polytechnic Institute, Materials Science and Engineering).

Dr. Sulin Zhang (Penn State University, Engineering Science and Mechanics), who gave me the opportunity to pursue my interest in materials modeling at the nanoscale.

Drs. Gary Gray and Francesco Costanzo (Penn State University, Engineering Science and Mechanics), who fundamentally shaped my teaching philosophy and awakened a love of teaching.

Dr. Donald Brenner (North Carolina State University, Materials Science and Engineering), who devoted resources and valuable time to mentoring me and providing me with research opportunities which challenged me and gave me the opportunity to explore the complexity insights which first-principles modeling can provide in very complex chemical and materials environments.

This research was primarily supported by the Consortium for Advanced Simulation of Light Water Reactors (<http://www.casl.gov>), an Energy Innovation Hub (<http://www.energy.gov/hubs>) for Modeling and Simulation of Nuclear Reactors under U.S. Department of Energy Contract No. DE-AC05-00OR22725.

TABLE OF CONTENTS

LIST OF TABLES	vii
LIST OF FIGURES	x
1 Introduction and Literature Review	1
1.1 Objective & Scope.....	2
1.2 Corrosion Product Build-up in Nuclear Reactors.....	3
1.2.1 Boron Incorporation in CRUD.....	4
1.2.2 Particulate Corrosion Products in Nuclear Reactor Coolant.....	6
1.3 Density Functional Theory Applied to Metal Oxides.....	7
1.4 Metal Oxide Thermodynamics from First-Principles Calculations	8
1.5 Roadmap.....	11
2 Methodology	13
2.1 Bulk Structure Calculations	14
2.2 Surface Structure Calculations	15
2.3 DFT Referenced Semi-empirical Thermodynamics.....	16
2.4 Calculation of Surface Energies of Metal Oxides	18
2.4.1 Nickel Oxide Surface Energies with Solid Chemical Potentials.....	18
2.4.2 Nickel Ferrite Surface Energies with Solid Chemical Potentials	19
2.4.3 Nickel Ferrite Surface Energies with Aqueous Chemical Potentials.....	21
2.5 Summary.....	24
3 Calculation of the Structure of Oxides and their Surfaces	25
3.1 Bulk Structure of Binary Oxides & Spinels	25
3.1.1 Binary Oxides.....	26
3.1.2 Ferrite Spinels	31
3.2 Calculating Effective Chemical Potentials.....	36
3.2.1 Validation	38
3.3 Survey of Prior Work Investigating the Surface Structure of Spinels and Oxides	40
3.3.1 Survey of Nickel Oxide Surface Investigations.....	40
3.3.2 Survey of Spinel Surface Investigations.....	41

3.4	Present Investigation into the Surface Structure of Nickel Oxide and Nickel Ferrite	43
3.4.1	Nickel Oxide.....	44
3.4.2	Nickel Ferrite	46
3.5	Environment Dependent Surface Energies	56
3.5.1	Nickel Oxide.....	56
3.5.2	Nickel Ferrite	62
4	Understanding CRUD Deposition	67
4.1	Origin of Particles in Reactor Coolant and CRUD.....	67
4.1.1	Morphology of NiO and NiFe ₂ O ₄ Crystallites.....	70
4.1.2	Homogeneous Nucleation.....	72
4.1.3	Agglomeration and Deposition.....	77
4.2	Thermodynamics of Boron Incorporation in CRUD	79
4.2.1	Calculations on Bulk Bonaccordite	80
4.2.2	Thermodynamics of Bonaccordite Formation	86
4.2.3	Formation of Lithium Borates in CRUD	89
	APPENDIX.....	107
	Appendix A Effective Chemical Potentials	108

LIST OF TABLES

Table 3.1 Comparison of properties determined in this study and reported values of key structural, magnetic, and electrical properties of NiO obtained from DFT calculations.	26
Table 3.2 Comparison of properties determined in this study and reported values of key structural, magnetic, and electrical properties of cobalt oxide (Co_3O_4) obtained from DFT calculations.....	27
Table 3.3 Comparison of values determined in this study and reported values obtained from DFT calculations of some properties of ZnO.....	28
Table 3.4 Comparison of properties determined in this study and reported values of key structural, magnetic, and electrical properties of Hematite ($\alpha\text{Fe}_2\text{O}_3$) obtained from DFT calculations.....	29
Table 3.5 Comparison of properties determined in this study and reported values of key structural, magnetic, and electrical properties of the Magnetite (Fe_3O_4) obtained from DFT calculations.....	31
Table 3.6 Comparison of properties determined in this study and reported values of key structural, magnetic, and electrical properties of Goethite ($\text{FeO}(\text{OH})$) obtained from DFT calculations.....	31
Table 3.7 Comparison of properties determined in this study and reported values of key structural, magnetic, and electrical properties of the inverse spinel nickel ferrite obtained from DFT calculations.....	33
Table 3.8 Comparison of properties determined in this study and reported values of key structural, magnetic, and electrical properties of the normal spinel zinc ferrite (ZnFe_2O_4) obtained from DFT calculations.	34
Table 3.9 Comparison of properties determined in this study and reported values of key structural, magnetic, and electrical properties of the <i>inverse</i> spinel cobalt ferrite (CoFe_2O_4) obtained from DFT calculations are placed according to Fig. 3.4.....	35
Table 3.10 Comparison of properties determined in this study and reported values of key structural, magnetic, and electrical properties of cobalt ferrite (CoFe_2O_4) in the <i>normal</i> spinel configuration obtained from DFT calculations.....	35
Table 3.11 The minimum energies of the structures calculated with the GGA+U approach at 0K, along with the k-space mesh density used.	36
Table 3.12 Comparison of the error incurred using the two fitting approaches to test the transferability of the first-principles results from single species metal oxides to mixed metal oxides. MAE is the maximum absolute error of the fit. The source of experimental data for the Gibbs free energy of formation is indicated by superscript number after the material name: (1) JANAF [112]; (2) Pankratz [113]; (3) Barin [114]; (4) Knacke [115].	38
Table 3.13 The energy of adsorption (Eq. (3.5)) for water on various nickel ferrite surfaces with respect to the energy of an isolated water molecule at 0K, where	

	$E_{\text{H}_2\text{O}}(0\text{K}) = -14.2188\text{eV}$, or a water molecule in liquid at 298.15K ($\mu_{\text{H}_2\text{O}}(298\text{K})$).	52
Table 3.14	Data for calculations of NiO surface energies including k-point mesh densities, type (MP=Monkhorst-Pack, Γ =Gamma-centered), in-plane surface super-cell dimensions, and internal angle between super-cell vectors.	57
Table 3.15	Critical data needed for evaluating various denuded nickel oxide surfaces including total DFT+U energy and the number of formula units of NiO and water. Note that the surface unit cell for the (111)OH-planar termination has $p(1 \times 1)$ symmetry, meaning that the unit cell has edges half the length of all other surface unit cells.	57
Table 3.16	Surface energies of all NiO surfaces studied in liquid water at 155bar. The surface energies are calculated with Eq. (3.6). Only those surfaces that are terminated have environment dependent surface energies.	58
Table 3.17	Energies of various NiO surfaces with multiple terminations in vacuum at 0K. ^a TPSSh and (PBE0) functionals with 12.5% exact exchange [124]; ^b Simulation [130]; ^c GGA+U ($U_{\text{eff}}=6.3\text{eV}$) [85]; ^d Hybrid-Meta-GGA B3LYP exchange-correlation functional [151]; ^e Estimated from reported binding energies [85].	60
Table 3.19	Critical data needed for evaluating various denuded nickel ferrite surfaces including total DFT+U energy and the number and type of atomic species. Stoichiometric surfaces are also provided and identified as the S surface cut. ...	63
Table 3.20	Critical data needed for evaluating various terminated nickel ferrite surfaces including total DFT+U energy and the number and type of atomic species.	64
Table 3.21	Data for calculations of nickel ferrite surface energies including k-point mesh densities, type (MP=Monkhorst-Pack, Γ =Gamma-centered), in-plane surface super-cell dimensions, and internal angle between super-cell vectors.	64
Table 3.22	Surface energies of denuded nickel ferrite surfaces at conditions representative of PWR coolant. The average and standard deviation of the equivalent (110) surfaces are provided separately from the stoichiometric (011) surface.	65
Table 3.23	Surface energies of terminated nickel ferrite surfaces at conditions representative of PWR coolant. The average and standard deviation of the equivalent (110)-1ML surfaces are provided separately from those of the partially terminated surfaces which are provided for each plane separately.	66
Table 4.1	Concentrations of species and conditions representative of various environments in operating PWRs are drawn Ref. [11] and reported in molal units at 473K. The conditions representing thick CRUD are obtained from Refs. [11,12]. These conditions are predicted to exist at a depth of 40 μm from the coolant-side CRUD with a total thickness of 60 μm .	68
Table 4.2	Scaled illustration of the Wulff construction for the equilibrium shapes of NiO crystallites in liquid and steam. The hydroxyl terminated (111) surface is grey and the denuded (100) surface is red.	72

Table 4.3 Scaled illustration of the Wulff construction for the equilibrium shapes of NiFe ₂ O ₄ particles in liquid and steam. The denuded (111)C surface is brown....	72
Table 4.4 Summary of detailed magnetic information and relative stability of calculated Bonaccordite structures with the five magnetic structures described in the text.	82
Table 4.5 Comparison of physical, electrical, and magnetic properties of Bonaccordite between this work and experimental values. References values are taken from Fernandes, <i>et al.</i> [162].	83
Table 4.6 Comparison of physical, electrical, and magnetic properties of lithium and boron oxides calculated in this work with experimental values. Superscript letters indicate the reference: ^a [164], ^b [165], ^c [166], ^d [167], ^e [168], ^f [169], ^g calculated value using GGA with exact exchange (experiment unavailable) [170], ^h calculated [171]. The data for lithium containing compounds were provided by A. D. Andersson at Los Alamos National Lab.	84
Table 4.7 This table supplements Table 3.11 by adding oxides containing boron and lithium.	84
Table 4.8 The first seven rows contain coefficients for Eq. (4.15) that have been fit to the elemental effective chemical potentials derived above. The bottom row contains coefficients for Eq. (4.15) that are fit to the calculated free energy of formation of Bonaccordite calculated using Eq. (4.14).	85

LIST OF FIGURES

- Figure 3.1 Depiction of the spinel structure showing the stacking sequence of sites along the [111] direction. A (tetrahedral) sites lie in T_1 and T_2 layers where the sites contain blue colored atoms. B (octahedral) sites lie in O_1 and O_2 layers where the sites contain brown colored atoms. 26
- Figure 3.2 The figures show the orientation of spin magnetic moments of Co (blue), or Ni (silver) layers separated by layers of O (red) in (a) nickel oxide (NiO), (b) cobalt oxide (Co_3O_4). The non-magnetic bulk structure of (c) zinc oxide (ZnO) is shown for completeness. Note that the arrows indicate only the relative orientation of the spins (parallel or antiparallel) between the layers not their crystallographic alignment. 28
- Figure 3.3 The figures show the orientation of spin magnetic moments of Fe (brown) layers separated by layers of O (red) in (a) Goethite ($\text{FeO}(\text{OH})$), (b) Hematite (Fe_2O_3), and (c) Magnetite (Fe_3O_4). Note that the arrows indicate only the relative orientation of the spins (parallel or antiparallel) between the layers not their crystallographic alignment. 30
- Figure 3.4 This figure shows the distribution of divalent metal cations (M^{+2}) in grey, trivalent iron (Fe^{+3}) in brown, and oxygen in red on 001 planes in an inverse spinel. The location of the plane along the c axis is indicated above each layer. Only planes that contain metal ions with octahedral coordination (B-sites) are shown. 32
- Figure 3.5 Prediction of the free energies of formation for zinc, cobalt, and nickel ferrite are plotted as determined from the partial and global fit with experimental values as a reference (see Table 3.12). The resulting fits for both $U_{\text{eff}}(\text{Fe}) = 3.5\text{eV}$ (left) and $U_{\text{eff}}(\text{Fe}) = 4.5\text{eV}$ (right) are plotted. 38
- Figure 3.6 Comparison of the predicted (solid lines) and measured (dashed lines) first solubility constants of various metal oxides according to Eqns.(3.1)–(3.4). 39
- Figure 3.7 Structures of the (100) surfaces of NiO are illustrated in the (a) denuded case and (b) with a full monolayer of water that has dissociated. Nickel atoms are colored silver, oxygen is red, and hydrogen is white. 44
- Figure 3.8 Surface structures of the (100) surfaces of NiO are illustrated with (a) 1, (b) 0.5, and (c) 0.25 monolayers of molecular water associatively adsorbed on the surface. Nickel atoms are colored silver, oxygen is red, and hydrogen is white. 45
- Figure 3.9 Structures of the (110) surfaces of NiO are illustrated in the (a) denuded case and (b) with a full monolayer of water that has dissociated. Nickel atoms are colored silver, oxygen is red, and hydrogen is white. 45
- Figure 3.10 Reconstructed NiO (111) surfaces are illustrated with various reconstructions as described in the text. Nickel atoms are colored silver, oxygen is red, and hydrogen is white. Surfaces (a, b, d-f) exhibit the $p(2 \times 2)$ -type reconstruction, while (c) has $p(1 \times 1)$ surface symmetry. 46

Figure 3.11 Views parallel to the NiFe_2O_4 surfaces investigated herein showing the planes where surfaces are generated. The planes investigated are the (a) (001), (b) (110), (c) (011), (d) (101), (e) (111). Surfaces are identified by both a plane index and a letter (A-E), which indicates the surface cut. The Ni^{+2} (grey), $\text{Fe}^{+2}/\text{Fe}^{+3}$ (brown), and O^{-2} (red) spheres represent the position of the ions.....	47
Figure 3.12 Denuded (001) surfaces of NiFe_2O_4 with terminations defined by Fig. 3.11a: (a) A, (b) B, and (c) is the stoichiometric surface.....	48
Figure 3.13 Denuded (011) surfaces (a) A, (b) B, as defined in Fig. 3.11c, and (c) is the stoichiometric surface.	48
Figure 3.14 Denuded (110) of NiFe_2O_4 with terminations defined by Fig. 3.11b: (a) A, and (b) is B.	49
Figure 3.15 Denuded (101) surfaces of NiFe_2O_4 with terminations defined by Fig. 3.11d: (a) A, (b) B, and (c) D.....	49
Figure 3.16 Denuded (111) surfaces of NiFe_2O_4 where Fe (brown), or Ni (gray) layers are separated by layers of O (red), as described in the text. Terminations are defined by Fig. 3.11e: (a) A, (b) A', (c) Stoichiometric, (d) B, (e) C, (f) D, and (g) E.	51
Figure 3.17 This figure shows all of the terminated (011) (a) A with 4 H_2O and 2 H_2 molecules, (b) A with one monolayer of water.	52
Figure 3.18 This figure shows all of the terminated (110) (a) A with one monolayer, (b) B with 4 H_2O and 2 excess O_2 molecules, and (c) B with one monolayer of water.	54
Figure 3.19 This figure shows all of the terminated (101) (a) B with 4 excess H_2 , and (b) B with one monolayer.....	55
Figure 3.20 This figure shows all stable terminated (111) surfaces of NiFe_2O_4 where Fe (brown), or Ni (gray) layers are separated by layers of O (red) terminated with H (pink), as described in the text. Surface terminations are defined by Fig. 3.11e: (a) A, (b) A', (c) B, (d) D, (e) E.....	55
Figure 3.21 The environment dependent surface energies for the investigated surfaces of NiO in liquid water at 155bar. Terminated surfaces are plotted as dashed lines, and denuded surfaces are plotted as solid lines. The (111) surfaces are plotted in green, (110) in blue, and (100) in red. The numbered labels correspond to the three variants of the (111)-OH surfaces illustrated in Fig. 3.10(d-f).....	59
Figure 3.22 Plot of surface energy versus temperature for NiO (100) surfaces at 10^{-10} bar.....	62
Figure 3.23 The (110) (blue), (111) (green), and (100) (red) surfaces of nickel ferrite are shown as a function of temperature in the presence of ions at concentrations typical of PWR coolant. Denuded surfaces are shown in the plot at left, and terminated surfaces are shown on the other plot. The energies of the denuded (111)A and (111)A' surfaces are not shown.	66
Figure 4.1 The free energy reaction for forming nickel oxide (left) from ions (Eq. (4.1)) and hydroxides (Eq. (4.2)) are plotted as solid and dashed lines, respectively.	

The free energy of reaction for forming nickel ferrite (right) from ions (Eq. (4.3)) and hydroxides (Eq. (4.4)) are plotted as solid and dashed lines, respectively. Lines marked with circles represent the reactions with concentrations increased a hundred-fold with $\text{pH} = 7.8$, approximating the conditions deep within CRUD. 70

Figure 4.2 The free energy reaction for forming nickel oxide (left) from ions (Eq. (4.1)) and hydroxides (Eq. (4.2)) are plotted as solid and dashed lines, respectively. The free energy of reaction for forming nickel ferrite (right) from ions (Eq. (4.3)) and hydroxides (Eq. (4.4)) are plotted as solid and dashed lines, respectively. Unmarked lines indications reactions occurring at $\text{pH} = 7.2$, while lines marked with circles are for $\text{pH} = 7.8$, both with concentrations unchanged from the bulk coolant..... 70

Figure 4.3 The lowest energy surfaces of (a) NiO and (b) NiFe₂O₄ are plotted. The (111) surface terminated with hydroxyl groups is the only surface which is dependent on the phase of the water. 71

Figure 4.4 Illustration of the definition of the characteristic width, a , of a regular octahedron, and those of a truncated octahedron, b and c 73

Figure 4.5 The free energy of the reaction, defined by Eq. (4.7), for forming a NiO particle (with characteristic length b) is plotted. The reaction is plotted for a pH of 7.2 (left) and 7.8 (right) with divalent cations at coolant concentrations. 74

Figure 4.6 Plot of the free energy of the reaction, given by Eq. (4.8), forming an octahedral NFO particle (with characteristic length a) from divalent cations at a pH of 7.2 (left) and 7.8 (right). 77

Figure 4.7 Plot of the free energy of the reaction, given by Eq. (4.8), forming an octahedral NFO particle (with characteristic length a) from divalent cations under the conditions specified by the deep CRUD conditions listed in Table 4.1. 77

Figure 4.8 Schematic diagram illustrating the proposed mechanism of particle generation in CRUD..... 79

Figure 4.9 Illustration of the structure of the (111) plane of Bonaccordite (Ni₂FeBO₅). Nickel and iron sites are shown as grey (A-H) and brown (I-L) octahedrons, respectively. The unit cell is indicated by a fine dotted line. 81

Figure 4.10 The predicted standard Gibbs free energy of formation of Bonaccordite (Eq. (4.14)) is plotted as a solid line that corresponds to the energy scale on the right. Dotted lines denote the new Gibbs Free energy for possible synthesis reactions in PWRs that are denoted by Eqns. (4.16)–(4.19). Numbers labeling lines on the plot correspond to the reactions given in Eqn. (4.14), and (4.16)–(4.19) Concentrations of aqueous species are taken to be the observed values in the coolant at a pressure of 155bar..... 87

Figure 4.11 Possible synthesis reactions in PWR CRUD (Eqns. (4.16)–(4.19)). Numbers labeling lines on the plot correspond to the reactions given in Eqns. (4.16)–(4.19). Concentrations of aqueous species are taken to be the values predicted by the CRUD models of EPRI and Henshaw, *et al.* at a depth of 40 μm in 60 μm CRUD

assuming a bulk coolant pressure of 155bar. The temperature predicted in these models is in excess of that included in the aqueous species database used to parameterize the current work..... 89

Figure 4.12 A plot of the reactions given by Eqns. (4.17), and (4.20)–(4.22) illustrates the relative free energies of some possible mechanisms for boron incorporation into CRUD. Concentrations of aqueous species are taken to be the values predicted by the CRUD models of EPRI and Henshaw, *et al.* at a depth of 40µm in 60µm thick CRUD assuming a bulk coolant pressure of 155bar. The temperature predicted by these models is in excess of that included in the aqueous species database used to parameterize the current work. 90

1 Introduction and Literature Review

The recent emphasis in the United States on developing abundant domestic sources of energy, together with an increasing awareness of the environmental hazards of fossil fuels, has led to a renewed interest in overcoming challenges to more extensive use of nuclear energy within the science and engineering community [1]. One of these challenges is controlling the precipitation of porous oxide deposits onto the nuclear fuel rod cladding from the primary coolant during operation of pressurized light-water reactors (PWRs) [2]. These deposits, called CRUD (an acronym for Chalk River Unidentified Deposits), are a major concern to reactor operation because they reduce fuel lifetime and efficiency by reducing heat transfer to the coolant, promoting corrosion, and depressing neutron flux [2–4]. The latter leads to what is called CRUD Induced Power Shift (CIPS), which is due to the presence of neutron-adsorbing boron trapped in the CRUD. Uncontrolled release of radioactive species from CRUD as the CRUD dissolves during reactor shut-down can also increase the levels of radiation in areas which may be accessed by plant personnel performing specialized maintenance activities.

This dissertation is intended to enable a more detailed understanding of how CRUD can grow in a nuclear reactor environment while adding predictive capabilities not present in continuum thermodynamic approaches to modeling CRUD growth. For example, present models do not account for the differing growth rates and stabilities of CRUD surfaces but simply assume isotropy. This may produce acceptable results within current operating regimes but is not extensible to future reactor designs or operating conditions significantly different from historical operating regimes. The reliance on empirical data slows the development process for new reactor designs and hinders engineers' ability to innovate with existing designs. This does not downplay the role of experiment but rather changes its role to validating models. If the nuclear renaissance is to continue and assure future generations safe, carbon-free electrical generation capability, advanced modeling and simulation capabilities must be developed to build an understanding of the factors that limit the performance of nuclear fuels or reduce their lifetime. Unless a predictive understanding is developed which allows for new

phenomena to be explored in alternative reactor designs, the scale and pace of future nuclear power development will be limited.

To usher in the nuclear renaissance the U.S. Department of Energy (DOE) funded the Consortium for Advanced Simulation of Light-water reactors (CASL)¹ Innovation Hub. The DOE Innovation Hubs are designed to enable research and development in energy solutions for meeting the demands for energy security, low-carbon generation, and increasing national competitiveness in the energy industry. The ultimate goal of CASL is to establish a predictive model of PWRs. The resulting 'Virtual Reactor' will include thermal hydraulics, neutronics, degradation mechanisms of critical materials, and uncertainty quantification. Well-developed models from industry, academia, and national labs are being incorporated as elements of the virtual reactor, but development of new models and methods will be required as well.

This work will contribute to the goal of the Materials Processing and Optimization (MPO) focus area with the goal of developing materials physics-based constitutive models for use in the Virtual Reactor. CASL's CRUD model has four primary goals [3]:

1. Compute CRUD thickness and composition versus time
2. Compute species release/absorption rate into coolant
3. Understand the boron deposition mechanism
4. Understand the CRUD Induced Localized Corrosion (CILC) mechanism

This dissertation contributes to the second and third goals of CASL's crud model by providing a more fundamental understanding of the growth of metal oxides present in CRUD.

1.1 Objective & Scope

This dissertation is intended to provide fundamental insights into the process by which CRUD is formed in PWRs by investigating the aqueous thermodynamics of formation of nickel oxide (NiO) and nickel ferrite (NiFe₂O₄) as representative CRUD components in bulk and nanoparticle morphologies. The technique developed in this

¹ The consortium website is located at <http://www.casl.gov>

dissertation is referred to as Density Functional Theory (DFT) referenced semi-empirical thermodynamics; it links 0K first-principles calculations with high temperature thermodynamics by redefining the reference chemical potentials of the constituent elements. This approach allows for the prediction of temperature and pressure dependent free energies of materials that are experimentally inaccessible or have not yet been measured. The technique also permits aqueous chemistry to be incorporated into thermodynamic calculations via the redefined reference chemical potentials. The ability to extend accurate first-principles calculations to high temperatures and aqueous environments allows the stability of crystal surfaces, calculated with DFT techniques, to be predicted at conditions representative of a PWR. With this information, this dissertation will determine under what conditions the particulate matter observed in CRUD could nucleate and be stable. A mechanism for agglomeration for the particles that is consistent with conditions located at the site of observed CRUD deposition will be proposed. The technique will then be applied to extending our understanding of a particular species sometimes present in CRUD for which no model has previously been developed.

1.2 Corrosion Product Build-up in Nuclear Reactors

To minimize CRUD deposition in PWRs, it was initially suggested that the coolant be maintained at a slightly basic pH that corresponds to a minimum solubility of magnetite, which was thought to be the major CRUD component. After it was established that the major component of CRUD is nickel ferrite, a slightly acidic pH was recommended that corresponds to the nickel ferrite minimum solubility. The $\text{pH}_{573\text{K}}$ of the coolant in PWRs is typically maintained at 7.2 ± 0.2 [4], which apparently reduces the concentration of corrosion products that precipitate as CRUD [5]. Corrosion of the tubing can also be reduced by addition of zinc to the coolant, which is incorporated into the protective oxide layer in the tubing.

Further control of CRUD deposition through chemical means requires a detailed knowledge of the thermodynamics and kinetics of metal oxides in solution under high temperature and pressure conditions, which for pressurized water reactors can be as

high as 350K and 155bar, respectively. While reliable thermodynamic data are available for many bulk ternary oxides at reactor temperatures and pressures, corresponding thermodynamic data for spinels with mixed compositions are not as readily available but can be calculated from first-principles [6]. In addition, understanding processes such as CRUD formation requires reliable solution phase data that can be combined with thermodynamic data for solids.

The species that deposit as CRUD originate from the products of the corrosion of heat exchanger tubing, and consist primarily of NiO and NiFe₂O₄ particles [3,4,7–9]. The thermodynamics that drives CRUD precipitation from water is relatively well known from experimental data [10,11]. There are also detailed continuum growth models that couple the thermodynamics, microstructure, flow and chemistry of CRUD [12,13]. However, there are critical details that are not available from experimental data and are not considered in existing models that are needed to make advances in chemically controlling CRUD formation. In particular, it is not known whether CRUD surfaces are denuded or terminated with products from reaction with water under the high temperature and pressure conditions of a PWR. A denuded surface would promote strong adsorption of solvated ions, while a surface terminated with H, OH, or H₂O would require loss or rearrangement of the terminating layer to add chemical species. These would be very different growth mechanisms with different kinetics. Furthermore, being able to predict surface energies and terminations opens possibilities for the rational introduction of chemical species that could protect CRUD surfaces against addition of growth species.

1.2.1 Boron Incorporation in CRUD

Another challenge posed by CRUD deposition is the resulting depression of neutron flux. This phenomena leads to what is called the Axial-Offset Anomaly (AOA) [11,12] (now known as CRUD-induced power shift (CIPS)), which is due to the presence of neutron-adsorbing boron trapped in the CRUD. The deposited boron reduces neutron flux by adsorbing the neutrons followed by transmutation to lithium. The reduction in thermal neutron flux makes it difficult to achieve high fuel burn-up. In a case study of a

plant that experienced severe AOA, the primary CRUD component was Bonaccordite [14], which has been found in other plants that experienced CIPS [8].

Despite the correlation between the presence of Bonaccordite in CRUD and plants experiencing CIPS, consideration of Bonaccordite is missing from CRUD deposition models [3,11–13] as a mechanism by which boric acid present in the coolant may be incorporated into CRUD. Part of the reason for this is the lack of experimental thermochemical data for the formation of this rare mineral. In addition, the hydrothermal synthesis experiments by Sawicki have only shown Bonaccordite formation at temperatures above 350°C, [15] which is significantly higher than the maximum coolant temperature of ~315°C in PWRs.

The amount of boron in Bonaccordite alone is not sufficient to explain CIPS [16]. Boron must be incorporated into CRUD in other forms as well, such as lithium metaborate (γ -LiBO₂) and lithium tetraborate (Li₂B₄O₇). In fact, the formation of lithium borates, is likely to be the dominant mechanism for the incorporation of boron into CRUD [11]. In the past, CRUD formation models assumed the formation of lithium metaborate was the primary means by which boron is incorporated into CRUD [12]. However, this compound has never been directly observed in PWR fuel CRUD [11,14] possibly because its dissolution is thermodynamically favored during reactor shutdown. Current models take lithium tetraborate to be the thermodynamically stable phase in CRUD [3]. Evidence corroborating the models comes from in situ observations of synthetic CRUD growth by Uchida *et al.* [16] who only observed the formation of lithium tetraborate, which readily dissolved upon cooling. Yet another mechanism for boron incorporation is the adsorption of boric acid onto surfaces of the primary components of CRUD. Experiments reveal that amount of boron adsorbed increases according to: NiO < ZrO₂ < NiFe₂O₄ < Fe₃O₄ [17]. Boric acid adsorption is typically modeled by fitting experimental results to adsorption isotherms [11]. A more detailed understanding of the mechanism and energetics of the adsorption process on (001) surfaces of NiO was recently modeled from first-principles [18]. The importance of this mechanism is motivation for carefully examining the structure of lowest energy surfaces of the

principle components of CRUD, which could be used to more accurately model the kinetics of adsorption and extend models to regimes for which no experimental data exists. Better understanding of the mechanism of boric acid adsorption on nickel ferrite is also of interest as it has been suggested to be a formation mechanism of Bonaccordite [17].

1.2.2 Particulate Corrosion Products in Nuclear Reactor Coolant

During regular operation of a PWR, water enters at 548K and exits at 598K where pressure is maintained at approximately 155bar to prevent bulk boiling. However, localized boiling will occur at nucleation sites on the fuel cladding that forms steam bubbles that detach from the surface and collapse in the coolant water, which is too cold to support boiling. Such boiling is referred to as sub-cooled nucleate boiling (SNB) and is a significant contribution to the heat flux from the fuel cladding to the water. CRUD is found to deposit on PWR fuel cladding in the region where SNB occurs. Experiments in controlled environments have demonstrated that colloidal metal particles in solution will preferentially deposit on metal surfaces at SNB sites [16,19,20]. However, these studies are most relevant for the initial stages of deposition where particles agglomerate onto the metal surface at the bubble/surface interface. One mechanism, proposed by Iwahori, *et al.* [21], is related to the observation that many metal oxides present hydrophobic surfaces at high temperatures characteristic of reactor coolant. This model proposes that such particles will stick to the interface between water and steam which will concentrate the particles and lead to agglomeration. Being in the presence of steam could significantly increase the probability of particles agglomerating or attaching to surfaces since it has been determined that the removal of the water layer from the particles is the rate limiting step for the attachment of colloidal metal oxide particles in the absence of SNB [22]. It is therefore possible that the rapid evaporation of water at the bubble/surface interface removes water and makes agglomeration and attachment of particles possible. However, this approach is only appropriate for the initiation of CRUD deposits. The deposition of thicker CRUD is usually modeled using continuum thermal hydraulics as a porous medium undergoing wick boiling [2-4,11-13,23]. The

wick-boiling models have an important feature in common with previously discussed micro-layer evaporation and dry-out models in that they both predict that deposition and agglomeration is driven by the increased concentration of solutes and colloids along with increased temperature.

The models discussed above all presuppose the presence of colloidal metal oxides in the coolant. However, it is agreed in the literature that particles do not nucleate homogeneously in the coolant or are unstable [4,24]. Castelli [4] estimates that particles 100nm in diameter will need to be in a solution with metal ions at a concentration of 125% of the saturation value in order for the particle to be stable. However, at least in the case of Castelli, surface energies were estimated and spherical particles assumed. Regardless of the source of the particles, it is known that up to ~90% of the mass of particulate matter in the coolant is under 200nm in diameter [24–26]. An IAEA study (see Table 4.1 of Ref. [5]) reports particulate matter composition and size during shutdown. Observations showed <5% of corrosion products were nickel ferrite with a diameter of approximately 200nm. Nearly 80% of the particulate matter was in the form of 20nm iron-rich $(\text{Fe}_x\text{Ni}_y\text{Cr}_z)_3\text{O}_4$ spinels. It has been suggested that the majority of these particulates grow on the steam generator tubing [5,24] and are transported to the core where they deposit as a component of CRUD, but this assertion is still heavily debated.

Particles that are only a few tens of nanometers in diameter are potentially single crystals with well-defined surfaces. In this case, understanding the surface structure and stability will lead to a more complete understanding of the mechanisms of agglomeration and provide information such as nucleation barriers that can be used to generate more accurate predictions of formation kinetics.

1.3 Density Functional Theory Applied to Metal Oxides

Standard DFT calculations employing the LSDA (local-spin-density approximation) or GGA (generalized-gradient approximation) exchange-correlation functionals are well known to be unable to accurately calculate the band gap, magnetic moment, and structure of magnetic insulating materials (such as transition metal oxides) due to

the strongly correlated behavior of the d and f electrons [27]. In fact, LSDA calculations predict Magnetite (Fe_3O_4) to be an antiferromagnetic metal at 0K rather than the ferrimagnetic insulator found experimentally [28,29]. The calculation of the band gap of nickel oxide (NiO) is not accurately accounted for by LSDA or GGA alone and it has been shown experimentally that the large Coulomb interaction between electrons in the d orbital of nickel is partially responsible for the observed band gap [30,31].

Many modifications of the basic LSDA and GGA functionals have been proposed that may improve the accuracy of DFT predictions for this problem, including the addition of a Hubbard-U term [32] and the use of hybrid functionals which incorporate exact (Hartree-Fock style) exchange [33]. In this dissertation, the GGA+U exchange-correlation functional is employed to make accurate and inexpensive calculations of metal oxides and their surfaces. The addition of a Hubbard-U terms is known to improve predictions of the structure and mechanical properties of transition metal oxides [34–36]. Employing a U parameter also allows the correct ground-state spin configuration of oxides and spinels to be determined which can cause significant errors in the total energy if not properly accounted for.

1.4 Metal Oxide Thermodynamics from First-Principles Calculations

DFT calculations have become a common tool for predicting and understanding the 0K properties of a wide range of materials. However, there remain challenges to using DFT to estimate finite temperature properties and to examine effects such as solvation on stability. In Car-Parrinello dynamics, for example, a fictitious Lagrangian allows nuclei (treated as classical particles) and electronic states to dynamically explore a coupled phase space, including liquid dynamics [37,38]. However, this approach is subject to the short time scales inherent to molecular dynamics simulation. Other well-established approaches use results from total energy DFT calculations to inform higher level modeling; examples include the “Computer Coupling of Phase Diagrams and Thermochemistry” (i.e. CALPHAD) for predicting equilibrium phases [39] and phase field modeling for studying evolving microstructures [40]. More recently an emphasis has been placed on calculating temperature and pressure-dependent free energies for

complex structures from enthalpies, entropies, and chemical potentials derived from first-principles [41–47].

First-principles thermodynamics is a technique by which first-principles calculations can be extended to finite temperatures using experimental thermodynamic data. This technique was originally developed to study reactions occurring at the surface of metal or metal oxide films [43,48] with gas molecules adsorbed on surfaces. It has been applied to determine the stability of metal oxide surfaces in environments including oxygen and water. In the case of surfaces, first-principles thermodynamics calculates chemical potentials of gasses as a function of pressure and temperature and approximates the chemical potential of metals and oxides as the energy, $E(0\text{K})$, calculated by the computational approach employed. In this manner the free energy of formation (at the reference temperature and pressure of $T_r = 298.15\text{K}$ and $P_0 = 1\text{bar}$) is computed according to

$$\Delta_f G_{\text{M}_x\text{O}_y}^0(T_r) = E_{\text{M}_x\text{O}_y}(0\text{K}) - xE_{\text{M}}(0\text{K}) - \frac{y}{2}\mu_{\text{O}_2}^0(T_r). \quad (1.1)$$

Temperature and pressure dependence of free energy of formation of the system is accounted for by the change in chemical potential of the gas phase, which is written as a reference value plus a temperature and pressure dependent component,

$$\mu_{\text{O}_2}(T, P) = \mu_{\text{O}_2}^0(0\text{K}) + \Delta\mu_{\text{O}_2}(T, P), \quad (1.2)$$

where the reference chemical potential $\mu_{\text{O}_2}^0(0\text{K})$ is often taken to be $E_{\text{O}_2}(0\text{K})$. Assuming an ideal diatomic gas model or an empirical function describing the temperature dependence of the specific heat, $C_p(T)$, the effect temperature and pressure on the chemical potential of oxygen is calculated as

$$\Delta\mu_{\text{O}_2}(T, P) = \int_{T_r}^{T'} C_p(T') dT' - T \int_{T_r}^{T'} \frac{C_p(T')}{T'} dT' - (T - T_r)S^0(T_r) + RT \ln\left(\frac{P}{P_0}\right). \quad (1.3)$$

This technique is limited in accuracy and is subject to systematic errors such as neglecting the temperature and pressure dependence of the solid phases and the well-known deficiency in the LSDA and GGA functionals, which calculate an overly strong bond in the oxygen molecule. Wang, *et al.* [49] suggests that a correction to the oxygen

bond energy may be employed resulting in a shift of the energy of formation of metal oxide compounds. The suggested correction involves adding $1.36\text{eV}/\text{O}_2$ to the formation energy which was determined by fitting the calculated energy of formation to experimental values of enthalpy of formation of various transition metal oxides. This approach effectively shifts the reference oxygen chemical potential away from the 0K DFT energy value used in Eq. (1.2).

In traditional first-principles thermodynamics treatments of metal oxides using Eq. (1.1), GGA and GGA+U calculations are mixed and the chemical potential of oxygen is used as a parameter to make the reference states match. However, if a consistent framework to investigate the formation many compounds is required, the need to use different U parameters for each compound makes it impossible to have the same ground state as it adds energy to the system which results in a different value of the oxygen chemical potential. Enthalpies of formation cannot be calculated in such systems since the oxygen chemical potential is not transferrable to compounds with other values of the U parameter, or those requiring U values to vary between elements. Various approaches have been taken to work around this limitation including redefining chemical potentials [48,50] and shifting the enthalpy of formation to match experimental results [51]. However, these approaches do not allow for the incorporation of additional metals or materials species that do not use the same U value. Because the reference state energy is different for each compound with a unique U value, a self-consistent reference state must be established between all of the components. One approach to establish a consistent reference state is that of Jain *et al.* [51] who added an additional term to shift the reference state to match experimental enthalpies of formation. This approach also incorporated the oxygen binding energy correction by Wang, *et al.* [49]. The energy shift is specific to each species of metal and U_{eff} parameter.

To overcome these limitations, the semi-empirical DFT-referenced thermodynamics technique was developed for this dissertation [52]. This approach establishes a self-consistent reference state by defining a set of effective chemical potentials (ECPs) at the reference state. The chemical potentials are derived by solving a set of linear

equations that relate DFT energies for the bulk structures to experimental heats of formation. A set of ECPs are derived that connect energies of (Co, Fe, Ni, Zn)Fe₂O₄ spinels and oxides calculated at 0K from DFT to free energies in high temperature environments relevant to the study of corrosion in PWRs.

1.5 Roadmap

This dissertation is intended to provide fundamental insights into the process by which CRUD is formed in PWRs by investigating the aqueous thermodynamics of formation of nickel oxide (NiO) and nickel ferrite (NiFe₂O₄) as representative CRUD components. The technique developed in this dissertation is referred to as Density Functional Theory (DFT) referenced semi-empirical thermodynamics; it links 0K first-principles calculations with high temperature thermodynamics by redefining the reference chemical potentials of the constituent elements. This technique permits aqueous chemistry to be incorporated into thermodynamic calculations and allows for the prediction of temperature and pressure dependent free energies of materials that are experimentally inaccessible or have not yet been measured. The ability to extend accurate first-principles calculations to high temperatures and aqueous environments allows the stability of crystal surfaces, calculated with DFT techniques, to be predicted at conditions representative of a PWR. Accurate values of surface energies are used in fulfilling the the principle goal of this dissertation which is to investigate the aqueous thermodynamics of formation of nickel oxide (NiO) and nickel ferrite (NiFe₂O₄) crystallites as representative CRUD components. Specifically, this dissertation investigates the thermodynamics of homogeneous nucleation of crystallites and proposes a mechanism for their agglomeration.

Chapter two of this dissertation proposes the semi-empirical DFT-referenced thermodynamics framework for predicting the thermodynamic stability of metal oxide and spinel phases that form CRUD. The procedure for conducting these calculations is described in detail followed by the derivation of the thermodynamic technique itself. The environment-dependent surface energy is derived for binary oxides and spinel ferrite oxides within the semi-empirical DFT-referenced thermodynamics framework.

Chapter three will first report the calculations of the bulk oxide and ferrite spinels structures that are needed for the accurate parameterization of the semi-empirical DFT-referenced thermodynamics technique. Next, the results of the investigation of surface structure will be provided which includes the equilibrium surface geometry for denuded, and with water associatively absorbed or dissociated on {100}, {110}, and {111} surfaces of nickel oxide and nickel ferrite. Finally, the temperature and environmental dependence of surface energy will be determined using DFT referenced semi-empirical thermodynamics and reported at representative PWR operating conditions.

Chapter four will investigate the possibility of formation of NiO and NiFe₂O₄ particles originating from detailed DFT calculations of surfaces and prediction of their stability in liquid water at the high temperatures and pressures typical of PWRs. Specifically, the nucleation barrier and critical size of the particles from aqueous precursors will be predicted at realistic PWR conditions. Finally, a mechanism will be proposed for the generation and agglomeration for the particles observed in the coolant that is consistent with conditions located at the site of observed CRUD deposition.

2 Methodology

In a series of papers reporting studies similar to the approach developed in this dissertation, Guo and Barnard calculated morphologies and relative thermodynamic stabilities of hematite and goethite iron oxide nanoparticles from a set of effective chemical potentials and surface energies [50,53,54]. The chemical potentials were derived by solving a set of linear equations that relate DFT energies for the bulk structures to experimental heats of formation. The surface energies were calculated from DFT with slab structures, and were assumed to be temperature independent. However, the presence of surface termination resulting from reaction with water introduces effective relative temperature and pressure dependencies to the surface energies. From these data they were able to construct quasi-phase diagrams for surface structures [54] and nanometer-scale cluster morphologies that depend on temperature, pressure and humidity [50]. The formation of crystallites may result in an equilibrium shape that is bound by more than the than lowest energy surface. Cluster morphology may have a role in agglomeration by resulting in higher energy surface being displayed. There is precedent for the study of nanometer-scale cluster morphology in literature including studies of spinels (Co_3O_4 [55], ZnCr_2O_4 [56], MgAl_2O_4 [57]), iron oxides (Hematite [50], Goethite [50]), and perovskites (TiO_2 [58–60]).

This dissertation uses a similar scheme, referred to as DFT-referenced semi-empirical thermodynamics [52], to calculate energies of nickel oxide and nickel ferrite in water as a function of temperature and pressure up to those typical of PWRs (pressure of 155bar and temperatures up to about 610K). As described in this chapter, the scheme involves deriving a consistent set of Effective Chemical Potentials (ECPs) by solving a set of coupled linear equations that combine DFT and experimental free energies for NiO, ZnO, Fe_2O_3 , Fe_3O_4 , $\text{FeO}(\text{OH})$, CoFe_2O_4 , ZnFe_2O_4 , NiFe_2O_4 and H_2O . CRUD also contains relatively smaller concentrations of Co and Zn, while the primary coolant contains solvated Ni^{+2} , Zn^{+2} , Fe^{+2} and Fe^{+3} ions. For the sake of future CRUD studies, and to help validate this approach, these Co and Zn are incorporated into the thermodynamic scheme, but not used in the surface energy calculations. Incorporation of these

species into the scheme also demonstrates the relative ease with which other elements can be added within this scheme (see also Ref. [42]).

The DFT-referenced semi-empirical thermodynamics technique introduced in this dissertation requires detailed calculations of both bulk and surface structures of oxides and spinels. The procedure for conducting these calculations is described in detail followed by the derivation of the thermodynamic technique itself. The environment-dependent surface energy is derived for binary oxides and spinel ferrite oxides within the DFT-referenced semi-empirical thermodynamics framework. A detailed derivation of the surface energy for non-stoichiometric spinel ferrites is performed so that the surface energy may be expressed in terms of the concentrations of ions, dissolved gasses, and pH present in the reactor environment. The surface energies calculated in this dissertation should be considered quasi-surface energies since they do not meet the standard thermodynamic definition which only applies to single component systems. The term ‘surface energy’ is commonly employed in the literature and will serve as a shorthand notation for ‘quasi-surface energy’ herein.

2.1 Bulk Structure Calculations

All DFT calculations were carried out using the generalized gradient approximation with the exchange-correlation functional of Perdew, Burke, and Ernzerhof [61,62] as implemented in VASP (Vienna Ab-initio Simulation Package) [38,63–65]. The Generalized Gradient Approximation including on-site Coulomb interactions (GGA+U) is employed where the on-site Coulomb interactions are implemented using the simplified rotationally-invariant formulation of Dudarev *et al.* [30]. The simplified implementation uses only the single parameter $U_{\text{eff}} = U - J$ to describe the Coulombic repulsion. Values for U_{eff} of 4.5eV on Fe [66], 6.0eV on Ni [51], 3.3eV on Co [49], and 4.7eV on all Zn atoms [35] in an oxide were used.

The accuracy of the GGA+U approach can be enhanced by assigning a unique U_{eff} parameter for each oxidation state of a given element. This was done for magnetite by Zhu, *et al.* [67] who used 4.0eV and 4.5eV for iron atoms with octahedral and tetrahedral coordination, respectively, and by Chen, *et al.* [68] for the $\text{Co}^{+2}/\text{Co}^{+3}$ oxidation

states of Co_3O_4 . In the present study this added degree of complexity is neglected in favor of a more transferable approach where mixed oxides could be investigated by assigning a single U_{eff} to a given element. Reproducing all aspects of the electronic structure of the oxides is not of critical interest in the present study, rather it is most important to reproduce the properties that have the most significant influence on the thermodynamic stabilities of the bulk oxides and ferrites.

Electrons within the ionic core were modeled with the projector augmented wave (PAW) pseudopotentials [69,70] included in VASP. The plane-wave kinetic energy cutoff was fixed at 520eV, which is 130% of the maximum value used to create the elements' pseudopotential. For all calculations the Monkhorst-Pack [71] scheme was used to sample the Brillouin zone (BZ) and the density of the k-space mesh was increased until the energy varied by less than 1.0×10^{-4} eV per formula unit.

Bulk properties were determined by fitting the energy versus volume data to the Birch-Murnaghan [72] equation of state. When calculating the bulk properties, the tetrahedron method with Blöchl corrections [70], was used during BZ integration. The difference in electronic energy between consecutive self-consistent cycles required for convergence was set to 5.0×10^{-7} eV $\times n$, where n is the number of ions in the system. Geometry optimization via a conjugate gradient algorithm continued until all forces were less than 1.5×10^{-2} eV/Å. The bulk energies reported are determined by performing an ionic relaxation at the equilibrium lattice parameter determined by the Birch-Murnaghan fit.

2.2 Surface Structure Calculations

Surface energy calculations were carried out using slab geometries, where periodicity was maintained in directions parallel to the surface and 15Å of vacuum separated surface planes. All slab calculations were performed with the outer four atomic layers allowed to relax (three atomic layers in the case of the (100) surfaces), while the remaining internal layers were fixed. Partial occupancies of orbitals were set using 0.1eV wide Gaussian smearing for all surface geometry optimizations. The use of symmetry was disabled for all surface calculations. The k-point mesh was reduced to a

single k-point in the direction normal to the surface with the number of k-points in the remaining directions scaled from that used for the bulk calculations. The electronic and force convergence criteria for surface calculations remained the same as the bulk.

2.3 DFT Referenced Semi-empirical Thermodynamics

The ECPs are defined such that their values reproduce the standard Gibbs free energy of formation, $\Delta_f G^0$, of the relevant oxides to satisfy the equations:

$$\Delta_f G_{\text{Fe}_2\text{O}_3}^0(T) = E_{\text{Fe}_2\text{O}_3}(0\text{K}) - 2\mu_{\text{Fe}}^0(T) - \frac{3}{2}\mu_{\text{O}_2}^0(T); \quad (2.1)$$

$$\Delta_f G_{\text{FeO(OH)}}^0(T) = E_{\text{FeO(OH)}}(0\text{K}) - \mu_{\text{Fe}}^0(T) - \mu_{\text{O}_2}^0(T) - \frac{1}{2}\mu_{\text{H}_2}^0(T); \quad (2.2)$$

$$\Delta_f G_{\text{Fe}_3\text{O}_4}^0(T) = E_{\text{Fe}_3\text{O}_4}(0\text{K}) - 3\mu_{\text{Fe}}^0(T) - 2\mu_{\text{O}_2}^0(T); \quad (2.3)$$

$$\Delta_f G_{\text{NiO}}^0(T) = E_{\text{NiO}}(0\text{K}) - \mu_{\text{Ni}}^0(T) - \frac{1}{2}\mu_{\text{O}_2}^0(T); \quad (2.4)$$

$$\Delta_f G_{\text{ZnO}}^0(T) = E_{\text{ZnO}}(0\text{K}) - \mu_{\text{Zn}}^0(T) - \frac{1}{2}\mu_{\text{O}_2}^0(T); \quad (2.5)$$

$$\Delta_f G_{\text{Co}_3\text{O}_4}^0(T) = E_{\text{Co}_3\text{O}_4}(0\text{K}) - 3\mu_{\text{Co}}^0(T) - 2\mu_{\text{O}_2}^0(T); \quad (2.6)$$

$$\Delta_f G_{\text{NiFe}_2\text{O}_4}^0(T) = E_{\text{NiFe}_2\text{O}_4}(0\text{K}) - \mu_{\text{Ni}}^0(T) - 2\mu_{\text{Fe}}^0(T) - 2\mu_{\text{O}_2}^0(T); \quad (2.7)$$

$$\Delta_f G_{\text{CoFe}_2\text{O}_4}^0(T) = E_{\text{CoFe}_2\text{O}_4}(0\text{K}) - \mu_{\text{Co}}^0(T) - 2\mu_{\text{Fe}}^0(T) - 2\mu_{\text{O}_2}^0(T); \quad (2.8)$$

$$\Delta_f G_{\text{ZnFe}_2\text{O}_4}^0(T) = E_{\text{ZnFe}_2\text{O}_4}(0\text{K}) - \mu_{\text{Zn}}^0(T) - 2\mu_{\text{Fe}}^0(T) - 2\mu_{\text{O}_2}^0(T). \quad (2.9)$$

In Eqns. (2.1)–(2.9) the E_A 's denote DFT energies of species A at 0K, the μ 's represent the ECPs, $\Delta_f G_A^0(T)$ are experimental free energies of formation, and the superscript naught denotes that the element is referenced to thermodynamic standard state pressure of 1bar (gas for O_2 and H_2 , solid for oxides and metals).

Eqns. (2.1)–(2.9) are used in two ways. First, Eqns. (2.1)–(2.6) contain six unknown quantities (the ECPs), and therefore they are used to determine a complete set of ECPs. These values are then substituted into Eqns. (2.7)–(2.9) to predict the free energies of formation of the spinel compounds. These predictions are used to validate the method by comparing to experimental free energy values. Once the method is validated, a new set of ECP values are determined that minimize errors (in a least squares sense) for all nine equations.

This approach does not explicitly account for various entropy effects that are important at high temperature. However, these effects are implicitly included by fitting ECP values to experimental free energies of formation. Furthermore, the magnetic order of these materials is often different at very low temperatures, where most are antiferromagnetic. This consideration is important in materials such as cobalt oxide (with a Néel temperature of 40K), zinc oxide (with a possible ordering transition at 10.5K), and magnetite (with the opening of a band gap and change in structure resulting from the Verwey transition at 125K) [73]. The complications resulting from these low energy states are mitigated by always conducting the DFT calculations for the crystal symmetry present at the thermodynamic standard state ($T = 298.15^\circ\text{C}$) and by fitting to temperature dependent experimental free energies.

Because of the importance of solvation chemistry with respect to reactor conditions, and for completeness, reactions (2.10)–(2.13) are considered in addition to the set of Eqns. (2.1)–(2.9), to determine a consistent set of ECPs for liquid (l) and gaseous (g) water along with the aqueous metal hydroxides and aqueous cations (aq):

$$\left(\Delta_f G_{\text{H}_2\text{O}}(T, P)\right)_g = \left(\mu_{\text{H}_2\text{O}}(T, P)\right)_g - \frac{1}{2}\mu_{\text{O}_2}^0(T) - \mu_{\text{H}_2}^0(T); \quad (2.10)$$

$$\left(\Delta_f G_{\text{H}_2\text{O}}(T, P)\right)_l = \left(\mu_{\text{H}_2\text{O}}(T, P)\right)_l - \frac{1}{2}\mu_{\text{O}_2}^0(T) - \mu_{\text{H}_2}^0(T); \quad (2.11)$$

$$\left(\Delta_f G_{M(\text{OH})_2}(T, P)\right)_{aq} = \left(\mu_{M(\text{OH})_2}(T, P)\right)_{aq} - \mu_M^0(T) - \mu_{\text{H}_2}^0(T) + \mu_{\text{O}_2}^0(T); \quad (2.12)$$

$$\begin{aligned} \left(\Delta_f G_{M^{+z}}(T, P)\right)_{aq} \\ = \left(\mu_{M^{+z}}(T, P)\right)_{aq} + \frac{z}{2}\mu_{\text{H}_2}^0(T) - \mu_M^0(T) - z\left(\mu_{\text{H}^+}^0(T, P)\right)_{aq}. \end{aligned} \quad (2.13)$$

The free energy of formation values for the aqueous ions (Ni^{+2} , Fe^{+2} , Fe^{+3} , Li^+ , Co^{+2} , and Zn^{+2}) were obtained from the SUPCRT 2007 database [74,75] that reports the values for solutions of unit activity on a molal basis. The SUPCRT database uses the revised Helgeson-Kirkham-Flowers equation of state [76] as implemented by Shock, *et al.* [77–79]. The standard free energy of formation Ni and Fe hydroxides are calculated using the definition of the second solubility coefficient K_{s2} tabulated in Ref. [80]. The reaction

between metal oxides and water defining the coefficient is then used to relate the formation of the complex to known free energies of formation of the reactants.

In keeping with standard practice for aqueous geochemistry and the SUPCRT database, the chemical potential of the proton, $(\mu_{\text{H}^+}^0(T, P))_{aq}$, is assumed to be zero at the reference pH of zero [81]. Reactions can be modeled at non-reference conditions by relating pH to H^+ activity, where $\text{pH} = -\log(a_{\text{H}^+})$ [82]. Activity is related to the chemical potential of a species x through the definition

$$\mu_x(T) = \mu_x^0(T_r) + RT \ln(a_x). \quad (2.14)$$

Similarly, the activity of the aqueous hydrogen ion may be expressed in terms of the solution pH as

$$\mu_{\text{H}^+}(T) = \mu_{\text{H}^+}^0(T_r) + RT \ln(10^{-\text{pH}}). \quad (2.15)$$

Because the ECPs determined here are expressed in molal form, the pH will be independent of pressure. The way in which pH is defined in this study means that the neutral pH is temperature dependent. Therefore, the pH reported in this study should be considered to be with reference to neutral water at standard temperature (298.15K).

2.4 Calculation of Surface Energies of Metal Oxides

Metal oxides can be challenging systems for which to calculate surface energies, as the surface terminations may be non-stoichiometric. Such surfaces have a complicated relationship to the environment in which they exist. The general form of the surface energy for a nickel iron oxide in the presence of hydrogen is given by

$$\begin{aligned} \gamma(T, P) = \frac{1}{2A} & \left(G_{\text{slab}} - n_{\text{Ni}}\mu_{\text{Ni}}(T, P) - n_{\text{Fe}}\mu_{\text{Fe}}(T, P) - n_{\text{H}_2}\mu_{\text{H}_2}(T, P) \right. \\ & \left. - n_{\text{O}_2}\mu_{\text{O}_2}(T, P) \right). \end{aligned} \quad (2.16)$$

2.4.1 Nickel Oxide Surface Energies with Solid Chemical Potentials

As discussed in the explanation of the thermodynamic model of this system, it is assumed that the free energy of the slab is approximated by the DFT+U calculated energy of the slab at 0K. There are n formula units of each element in the slab. These chemical potentials are not the ECPs (μ^0) defined in Sec. 2.3, rather they are floating

chemical potentials defined by the environment. For clarity, the notation indicating that the chemical potentials are functions of temperature and pressure will not be included in the derivation to follow, even though they remain so. The nickel oxide surface will be assumed to be in equilibrium with chemical reservoirs of bulk nickel oxide, nickel, and water. In equilibrium, the chemical potentials of bulk nickel oxide and water are defined as

$$\mu_{\text{NiO}} = \mu_{\text{Ni}} + \frac{1}{2}\mu_{\text{O}_2}, \quad (2.17)$$

$$\mu_{(\text{H}_2\text{O})_\ell} = \mu_{\text{H}_2} + \frac{1}{2}\mu_{\text{O}_2}. \quad (2.18)$$

In this case, the chemical potential of nickel oxide is fixed to the free energy of the bulk such that

$$\mu_{\text{NiO}} = E_{\text{NiO}} = \mu_{\text{Ni}} + \frac{1}{2}\mu_{\text{O}_2}. \quad (2.19)$$

We can eliminate the hydrogen chemical potential by substituting Eq. (2.18), solved for μ_{H_2} , into Eq. (2.16) such that

$$\gamma(T, P) = \frac{1}{2A} \left(E_{\text{slab}} - n_{\text{Ni}}\mu_{\text{Ni}} - n_{\text{H}_2} \left(\mu_{(\text{H}_2\text{O})_\ell} - \frac{1}{2}\mu_{\text{O}_2} \right) - n_{\text{O}_2}\mu_{\text{O}_2} \right). \quad (2.20)$$

Now, since our system does not have access to a reservoir of molecular oxygen, we can eliminate its chemical potential by substituting Eq. (2.19), solved for μ_{O_2} , into Eq. (2.20) so that

$$\gamma(T, P) = \frac{1}{2A} \left(E_{\text{slab}} - n_{\text{Ni}}\mu_{\text{Ni}} - n_{\text{H}_2}\mu_{(\text{H}_2\text{O})_\ell} - 2 \left(n_{\text{O}_2} - \frac{n_{\text{H}_2}}{2} \right) (g_{\text{NiO}} - \mu_{\text{Ni}}) \right). \quad (2.21)$$

After collecting terms, the surface energy can be expressed in terms of the chemical potentials of nickel oxide, nickel, and water:

$$\gamma(T, P) = \frac{1}{2A} [E_{\text{slab}} - (n_{\text{Ni}} + n_{\text{H}_2} - 2n_{\text{O}_2})\mu_{\text{Ni}} - (2n_{\text{O}_2} - n_{\text{H}_2})g_{\text{NiO}} - n_{\text{H}_2}\mu_{\text{H}_2\text{O}}]. \quad (2.22)$$

2.4.2 Nickel Ferrite Surface Energies with Solid Chemical Potentials

Nickel ferrite is a challenging system for which to calculate surface energies, as the surface terminations may be non-stoichiometric. Such surfaces have a complicated

relationship to the environment in which they exist. The general form of the surface energy for nickel ferrite is given by

$$\gamma(T, P) = \frac{1}{2A} \left(G_{\text{slab}} - n_{\text{Ni}} \mu_{\text{Ni}}(T, P) - n_{\text{Fe}} \mu_{\text{Fe}}(T, P) - n_{\text{H}_2} \mu_{\text{H}_2}(T, P) - n_{\text{O}_2} \mu_{\text{O}_2}(T, P) \right). \quad (2.23)$$

The surface will be modeled to be in equilibrium with chemical reservoirs of bulk nickel ferrite, iron, nickel, and water. In equilibrium, the chemical potentials of bulk nickel ferrite and water are defined as

$$\mu_{\text{NiFe}_2\text{O}_4} = \mu_{\text{Ni}} + 2\mu_{\text{Fe}} + 2\mu_{\text{O}_2}, \quad (2.24)$$

$$\mu_{(\text{H}_2\text{O})_l} = \mu_{\text{H}_2} + \frac{1}{2}\mu_{\text{O}_2}. \quad (2.25)$$

In this case, the chemical potential of n is fixed to the free energy of the bulk such that

$$E_{\text{NiFe}_2\text{O}_4} = \mu_{\text{Ni}} + 2\mu_{\text{Fe}} + 2\mu_{\text{O}_2}. \quad (2.26)$$

We can eliminate the hydrogen chemical potential by substituting Eq. (2.25), solved for μ_{H_2} , into Eq. (2.16) such that

$$\gamma(T, P) = \frac{1}{2A} \left(E_{\text{slab}} - n_{\text{Ni}} \mu_{\text{Ni}} - n_{\text{Fe}} \mu_{\text{Fe}} - n_{\text{H}_2} \left(\mu_{(\text{H}_2\text{O})_l} - \frac{1}{2}\mu_{\text{O}_2} \right) - n_{\text{O}_2} \mu_{\text{O}_2} \right). \quad (2.27)$$

Now, since our system does not have access to a reservoir of molecular oxygen, we can eliminate its chemical potential by substituting Eq. (2.26), solved for μ_{O_2} , into Eq. (2.27) so that

$$\begin{aligned} \gamma(T, P) = \frac{1}{2A} \left(E_{\text{slab}} - n_{\text{Ni}} \mu_{\text{Ni}} - n_{\text{Fe}} \mu_{\text{Fe}} \right. \\ \left. - n_{\text{H}_2} \left(\mu_{(\text{H}_2\text{O})_l} - \frac{1}{4} (E_{\text{NiFe}_2\text{O}_4} - \mu_{\text{Ni}} - 2\mu_{\text{Fe}}) \right) \right. \\ \left. - \frac{n_{\text{O}_2}}{2} (E_{\text{NiFe}_2\text{O}_4} - \mu_{\text{Ni}} - 2\mu_{\text{Fe}}) \right). \quad (2.28) \end{aligned}$$

After collecting terms, the surface energy can be expressed in terms of the chemical potentials of nickel, iron, nickel ferrite, and water:

$$\gamma(T, P) = \frac{1}{2A} [E_{\text{slab}} - \Gamma_{\text{Fe}}\mu_{\text{Fe}} - \Gamma_{\text{Ni}}\mu_{\text{Ni}} - \Gamma_{\text{NiFe}_2\text{O}_4}E_{\text{NiFe}_2\text{O}_4} - n_{\text{H}_2}\mu_{\text{H}_2\text{O}}] \quad (2.29)$$

where,

$$\Gamma_{\text{Fe}} = n_{\text{Fe}} - n_{\text{O}_2} + \frac{n_{\text{H}_2}}{2}, \quad (2.30)$$

$$\Gamma_{\text{Ni}} = n_{\text{Ni}} - \frac{n_{\text{O}_2}}{2} + \frac{n_{\text{H}_2}}{4}, \quad (2.31)$$

$$\Gamma_{\text{NiFe}_2\text{O}_4} = \frac{n_{\text{O}_2}}{2} - \frac{n_{\text{H}_2}}{4}. \quad (2.32)$$

The chemical potentials of Fe, Ni, and O₂ must remain within limits determined by the formation of undesired phases such as pure metals while ensuring that nickel ferrite is formed according to the inequalities:

$$\mu_{\text{Ni}} \leq g_{\text{Ni}}, \quad (2.33)$$

$$\mu_{\text{Fe}} \leq g_{\text{Fe}}, \quad (2.34)$$

$$\mu_{\text{Ni}} + 2\mu_{\text{Fe}} + 2\mu_{\text{O}_2} \geq g_{\text{NiFe}_2\text{O}_4}. \quad (2.35)$$

We can translate these conditions into known quantities by subtracting the chemical potentials of the elements in their reference states (the ECP) from both sides of the equations and defining the difference between the chemical potential and the ECP as $\Delta\mu$. Since the difference between the free energy of a material and the sum of its constituent elements in the reference state is the free energy of formation, the limits on the metal chemical potentials become

$$\Delta\mu_{\text{Ni}} \leq 0, \quad (2.36)$$

$$\Delta\mu_{\text{Fe}} \leq 0, \quad (2.37)$$

$$\Delta\mu_{\text{Ni}} + 2\Delta\mu_{\text{Fe}} + 2\Delta\mu_{\text{O}_2} \geq \Delta_f G_{\text{NiFe}_2\text{O}_4}. \quad (2.38)$$

2.4.3 Nickel Ferrite Surface Energies with Aqueous Chemical Potentials

In the coolant of a PWR, the source of iron and nickel will not be pure metals, but rather their aqueous cations. Consequently, the change in chemical potential of the metals should be expressed in terms of the change in chemical potential of their cations in solution. By definition, the free energy of formation of a cation with charge z is calculated using the reaction [83]:

$$M + z(\text{H}^+)_{aq} = (M^{+z})_{aq} + \frac{z}{2}(\text{H}_2)_g. \quad (2.39)$$

The free energy is calculated via the corresponding equilibrium equation,

$$(\mu_{M^{+z}})_{aq} = \mu_M - \frac{z}{2}\mu_{\text{H}_2} + z\mu_{\text{H}^+}, \quad (2.40)$$

which must also hold in the reference state where

$$(\Delta_f G_{M^{+z}})_{aq} = (\mu_{M^{+z}}^0)_{aq} + \frac{z}{2}\mu_{\text{H}_2}^0 - \mu_M^0 - z\mu_{\text{H}^+}^0. \quad (2.41)$$

Solving Eq. (2.41) for the ERCP of the divalent cation and subtracting it from both sides of Eq. (2.40) yields:

$$\Delta\mu_{M^{+z}} = \Delta\mu_M + z\Delta\mu_{\text{H}^+} - \frac{z}{2}\Delta\mu_{\text{H}_2} - (\Delta_f G_{M^{+z}})_{aq}. \quad (2.42)$$

We can also write the free energy change of the metal in terms of the free energy of the divalent cation as

$$\Delta\mu_M = \Delta\mu_{M^{+z}} - z\Delta\mu_{\text{H}^+} + \frac{z}{2}\Delta\mu_{\text{H}_2} + (\Delta_f G_{M^{+z}})_{aq}. \quad (2.43)$$

Since our system will not have access to gaseous H_2 , only the solvated molecule, we relate the energy between the two in the reference state, using

$$(\mu_{\text{H}_2})_{aq} = \mu_{\text{H}_2} + \Delta G_{\text{hyd}}. \quad (2.44)$$

In the reference state,

$$(\Delta_f G_{\text{H}_2})_{aq} = (\mu_{\text{H}_2}^0)_{aq} - \mu_{\text{H}_2}^0. \quad (2.45)$$

Solving Eq. (2.45) for $\mu_{\text{H}_2}^0$ and subtracting it from Eq. (2.44) yields the desired relationship

$$(\Delta\mu_{\text{H}_2})_{aq} = \Delta\mu_{\text{H}_2}, \quad (2.46)$$

because the free energy of hydration is identical to the free energy of formation for a hydrated species.

Since concentrations will be known, it will be more convenient to express Eq. (2.29) in terms of the chemical potential of ions and aqueous species. This will be accomplished by substituting Eq. (2.44) into (2.40) and solving for the chemical potential of the metal in the solid phase so that

$$\mu_M = (\mu_{M^{+z}})_{aq} + z\mu_{\text{H}^+} - \frac{z}{2}\left((\mu_{\text{H}_2})_{aq} - (\Delta_f G_{\text{H}_2})_{aq}\right). \quad (2.47)$$

Substituting Eq. (2.47) into (2.29), assuming divalent cations ($z = 2$) and simplifying, we can express the surface energy in terms of the chemical potential of aqueous species as

$$\begin{aligned} \gamma(T, P) = \frac{1}{2A} \{ & E_{\text{slab}} - \Gamma_{\text{Fe}} \mu_{\text{Fe}^{+2}} - \Gamma_{\text{Ni}} \mu_{\text{Ni}^{+2}} - \Gamma_{\text{NiFe}_2\text{O}_4} E_{\text{NiFe}_2\text{O}_4} - n_{\text{H}_2} \mu_{\text{H}_2\text{O}} \\ & - [\Gamma_{\text{Fe}} + \Gamma_{\text{Ni}}] \cdot ((\Delta_f G_{\text{H}_2})_{\text{aq}} - (\mu_{\text{H}_2})_{\text{aq}} + 2\mu_{\text{H}^+}) \}. \end{aligned} \quad (2.48)$$

Finally, the limits on the change in the free energy of the pure metals and nickel ferrite (Eqns. (2.36) and (2.37)) are expressed in terms of the free energy of the divalent cation using Eq. (2.43) such that:

$$\Delta\mu_{\text{Ni}^{+2}} - 2\Delta\mu_{\text{H}^+} + (\Delta\mu_{\text{H}_2})_{\text{aq}} + (\Delta_f G_{\text{Ni}^{+2}})_{\text{aq}} \leq 0, \quad (2.49)$$

$$\Delta\mu_{\text{Fe}^{+2}} - 2\Delta\mu_{\text{H}^+} + (\Delta\mu_{\text{H}_2})_{\text{aq}} + (\Delta_f G_{\text{Fe}^{+2}})_{\text{aq}} \leq 0. \quad (2.50)$$

However, the oxygen chemical potential in the condition for nickel ferrite formation is not easily observed but can be eliminated using Eq. (2.25) which allows Eq. (2.38) by substituting

$$\begin{aligned} 2\Delta\mu_{\text{Fe}^{+2}} + \Delta\mu_{\text{Ni}^{+2}} - 6\Delta\mu_{\text{H}^+} - (\Delta\mu_{\text{H}_2})_{\text{aq}} + 4(\Delta_f G_{\text{H}_2\text{O}})_l + 2(\Delta_f G_{\text{Fe}^{+2}})_{\text{aq}} \\ + (\Delta_f G_{\text{Ni}^{+2}})_{\text{aq}} \geq \Delta_f G_{\text{NiFe}_2\text{O}_4}. \end{aligned} \quad (2.51)$$

The chemical potential differences can be related to readily observed quantities such as concentration and pH. Reactions can be modeled at non-neutral conditions by adjusting the chemical potential of hydrogen ions relative to the reference value at neutral pH. Activity is related to the chemical potential of a species through the definition

$$(\mu_{\text{H}^+})_{\text{aq}} = (\mu_{\text{H}^+}^0)_{\text{aq}} + RT \ln(a_{\text{H}^+}). \quad (2.52)$$

In keeping with standard practice for aqueous chemistry, the standard chemical potential of the proton, $(\mu_{\text{H}^+}^0)_{\text{aq}}$, is taken to be zero [83]. The activity of the aqueous hydronium may be written in terms of pH such that $\text{pH} = -\log(a_{\text{H}^+})$ [82]. The chemical potential change of H^+ is therefore written as

$$(\Delta\mu_{\text{H}^+})_{aq} = RT \ln(10^{-\text{pH}}). \quad (2.53)$$

Because the ERCs determined here are expressed in molal form, the pH will be independent of pressure. The way in which pH is defined in this study means that the neutral pH is temperature dependent. Therefore, the pH reported in this study should be considered to be with reference to neutral water at standard temperature (298.15K). Assuming an ideal solution, the activity in Eq. (2.52) may be approximated as the molal concentration. The chemical potential change of a metal ion can then be expressed in terms of its molal concentration (x_M) as

$$\Delta\mu_M = RT \ln(x_M). \quad (2.54)$$

2.5 Summary

In this chapter, the semi-empirical DFT-referenced thermodynamics technique is developed to provide a means to connect 0K first-principles calculations to high temperature conditions relevant for studying corrosion in PWRs. The technique was extended to incorporate aqueous species and water which enables the calculation of surface energies in aqueous environments. Since DFT calculations of surfaces are derived from the energies of slabs, the calculation of surface energy for both stoichiometric and non-stoichiometric slabs was derived for the case of NiO and NiFe₂O₄. The surface energy was also derived for the special case of surface energies defined with aqueous species serving as chemical reservoirs.

3 Calculation of the Structure of Oxides and their Surfaces

Accurate determination of the ECPs are needed to study the thermodynamics of binary oxides and spinels. This is accomplished through detailed calculations of the ground state energy of the materials used to derive the ECPs. This chapter reports and discusses the DFT+U calculations for the relevant solid-phase of binary oxides (NiO, Co₃O₄, ZnO, FeO(OH), α -Fe₂O₃, Fe₃O₄), and spinels (NiFe₂O₄, ZnFe₂O₄, CoFe₂O₄). For the spinels, both the normal and inverse structures are investigated. A discussion of the effect of changing the iron U_{eff} parameter from 3.5eV to 4.5eV is included for each solid system containing iron. This is followed by validation of the DFT referenced semi-empirical thermodynamics approach using ECPs to predict free energies of formation for the ferrites. An optimized set of ECPs is then determined via best fit to the free energies for all 9 oxides and spinels. The method is further validated for the solution-phase chemistry by comparing the first solubility constant for binary metal oxides to experimental values. Of fundamental importance to the goals of this dissertation, the results of the investigation of the surface structure of NiO and NiFe₂O₄ are reported. The DFT calculated energies of the model surfaces are used with the DFT referenced semi-empirical thermodynamics scheme to calculate environmentally dependent surface energies.

3.1 Bulk Structure of Binary Oxides & Spinel

The arrangement of spin magnetic moments in spinels and oxides varies widely, but those investigated in this study are nonmagnetic, antiferromagnetic, or ferrimagnetic. In a spinel structure, metal ions are stacked in layers normal to the [111] direction. Fig. 3.1 labels the layers that contain B (octahedral) sites as O₁ and O₂, and A (tetrahedral) sites as T₁ and T₂. The notation for this scheme will show spin orientation of a layer as an arrow indicating the relative orientation of the spin up (\uparrow), down (\downarrow) or null (\emptyset) in the construct O₁[T₁O₂T₂]O₁. The square brackets denote the trilayer containing the T₁, O₂, and T₂ planes.

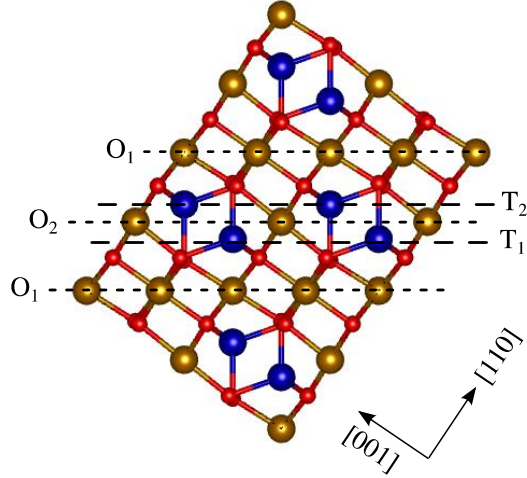


Figure 3.1 Depiction of the spinel structure showing the stacking sequence of sites along the $[111]$ direction. A (tetrahedral) sites lie in T_1 and T_2 layers where the sites contain blue colored atoms. B (octahedral) sites lie in O_1 and O_2 layers where the sites contain brown colored atoms.

3.1.1 Binary Oxides

Nickel oxide (NiO) is an antiferromagnetic oxide with the $Fm\bar{3}m$ space group and is isostructural with Rocksalt (NaCl). The minimum energy magnetic configuration results in Ni atoms in (111) planes having antiferromagnetic alignment of spins as illustrated in Fig. 3.2a. A comparison of some bulk thermodynamic properties calculated in this study and literature values are given in Table 3.1.

Table 3.1 Comparison of properties determined in this study and reported values of key structural, magnetic, and electrical properties of NiO obtained from DFT calculations.

nickel oxide NiO	GGA+U This work $U_{\text{eff}} = 6.0\text{eV}$	GGA+U [84] $U_{\text{eff}} = 5.3\text{eV}$	GGA+U [85] $U_{\text{eff}} = 6.3\text{eV}$	LSDA+U [30] $U_{\text{eff}} = 6.2\text{eV}$	Experiment
a (Å)	4.194	4.19	4.20	4.19	4.17 [86]
E_g (eV)	3.282	3.10	3.10	3.00	4.3 [31]
B (GPa)	181.730	-	203.00	182.00	145, 189, 205 [30]
$M_{\text{net}}(\mu_B)$	0.000	0.00	0.00	0.00	0.00
$\text{Ni}^{+2}(\mu_B)$	± 1.721	± 1.69	± 1.69	-	± 1.90 [86]

Cobalt oxide (Co_3O_4) is an antiferromagnetic normal spinel with $F\bar{4}3m$ having a very low Néel temperature ($T_N = 40\text{K}$). It is experimentally observed that only the doubly charged A site cations have a net moment [87] described as a $|\downarrow | \uparrow|$ state as illustrated in Fig. 3.2b. A comparison between bulk properties calculated during the course of this study and available literature data is shown in Table 3.2.

Table 3.2 Comparison of properties determined in this study and reported values of key structural, magnetic, and electrical properties of cobalt oxide (Co_3O_4) obtained from DFT calculations.

Cobalt oxide Co_3O_4 $ \downarrow \uparrow $	GGA+U This work $U_{\text{eff}}(\text{Co}^{+2}, \text{Co}^{+3})$ = 3.3eV	GGA+U [68] $U_{\text{eff}}(\text{Co}^{+2}) = 4.4\text{eV}$ $U_{\text{eff}}(\text{Co}^{+3}) = 6.7\text{eV}$	GGA+U [49] $U_{\text{eff}}(\text{Co}^{+2}, \text{Co}^{+3})$ = 3.3eV	Experiment [87]
a (Å)	8.153	8.27	–	8.065
E_g (eV)	1.541	1.96	1.60	1.6 [88]
B (GPa)	196.766	192	–	–
M_{net} ($\mu_B/\text{f.u.}$)	0.000	0.00	0.00	0.000
$\text{Co}^{+2}(\text{A})$ (μ_B)	± 2.632	± 2.84	± 2.67	± 3.02
$\text{Co}^{+3}(\text{B})$ (μ_B)	0.000	0.00	0.07	0.0

Zinc oxide (ZnO) has the Wurtzite (ZnS) structure, shown in Fig. 3.2c, with the $P6_3mc$ space group and is non-magnetic. The U_{eff} value of 4.7eV was determined by fitting the energy of the Zn-3d electrons to experimentally derived values [35]. There is some debate in the literature as to the magnitude or need for the application of the Hubbard U parameter to the p -orbitals [89]. Comparing the results from this and other studies with and without U_{eff} shows that none are able to accurately predict the band gap of ZnO. However, the use of the GGA+U functional does substantially increase the band-gap from that determined with the GGA functional alone (see comparison in Table 3.3). Addition of a $U_{\text{eff}} = 9.7\text{eV}$ on the p -orbital only adds a minor correction to the band-gap to which increases to 2.22eV. From the collected values of previous literature, and testing conducted but not reported during the course of this study, it is observed that as the magnitude of U_{eff} increases it has a proportionately smaller effect on the band gap and lattice parameter.

Table 3.3 Comparison of values determined in this study and reported values obtained from DFT calculations of some properties of ZnO.

zinc oxide ZnO	GGA+U	GGA	GGA	GGA+U	Experiment [91]
	This work $U_{\text{eff}} = 4.7\text{eV}$	This work $U_{\text{eff}} = 0\text{eV}$	[90] $U_{\text{eff}} = 0\text{eV}$	[89] $U_{\text{eff}} = 11.97\text{eV}$	
a (Å)	3.237	3.291	3.250	3.281	3.258
c (Å)	5.217	5.306	5.207	5.256	5.220
E_g (eV)	1.339	0.362	0.804	1.610	3.441 [92]
B (GPa)	130.640	127.821		135.050	133.700
B' (GN/m ³)	4.280	4.436		4.900	4 (fixed)

The lowest energy magnetic structures of the iron oxides are shown schematically in Fig. 3.3: (a) Goethite and (b) Hematite are antiferromagnetic, while (c) Magnetite is ferrimagnetic in agreement with the spin configurations found in prior LSDA+U [28,30], and GGA+U [66,93] studies.

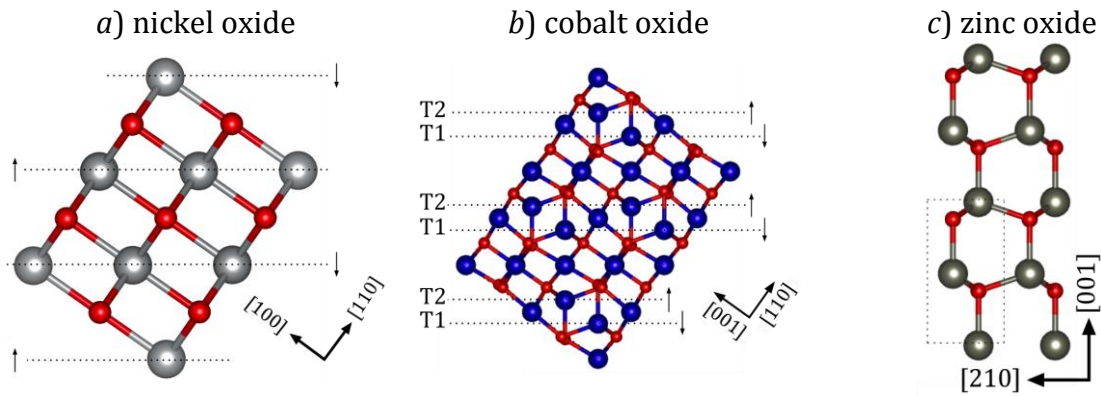


Figure 3.2 The figures show the orientation of spin magnetic moments of Co (blue), or Ni (silver) layers separated by layers of O (red) in (a) nickel oxide (NiO), (b) cobalt oxide (Co₃O₄). The non-magnetic bulk structure of (c) zinc oxide (ZnO) is shown for completeness. Note that the arrows indicate only the relative orientation of the spins (parallel or antiparallel) between the layers not their crystallographic alignment.

Hematite ($\alpha\text{Fe}_2\text{O}_3$) is an antiferromagnetic oxide ($T_N = 955\text{K}$) with the $R\bar{3}c$ space group and is isostructural with Corundum ($\alpha\text{Al}_2\text{O}_3$). A comparison between

reported and presently calculated values is given in Table 3.4. The primary effect of the U_{eff} value in the range of 3.5–4.5eV is to increase the band gap.

Table 3.4 Comparison of properties determined in this study and reported values of key structural, magnetic, and electrical properties of Hematite ($\alpha\text{Fe}_2\text{O}_3$) obtained from DFT calculations.

Hematite Fe₂O₃	GGA+U This work $U_{\text{eff}}(\text{Fe}^{+3}) = 3.5\text{eV}$	GGA+U This work $U_{\text{eff}}(\text{Fe}^{+3}) = 4.5\text{eV}$	GGA+U [66] $U_{\text{eff}}(\text{Fe}^{+3}) = 4.5\text{eV}$	Experiment [94]
a (Å)	5.482	5.477	5.474	5.428
α	55.105°	55.175°	55.217°	55.256°
E_g (eV)	1.914	2.322	2.200	2.2 [95]
B (GPa)	191.068	189.953	190.300	
M_{net} ($\mu_B/\text{f. u.}$)	0.000	0.000	0.000	0.000
Fe^{+3} (μ_B)	± 4.105	± 4.197		

Magnetite (Fe_3O_4) is a ferrimagnetic inverse spinel ($T_N = 858\text{K}$) with the $Fd\bar{3}m$ space group. The study of the magnetic properties of magnetite are complicated by the Verwey transition at 125K [73], whereupon symmetry is lowered and a band gap of 0.15eV opens [96]. By constraining the minimization to a cubic lattice, the room-temperature behavior was modeled and the half-metallic state obtained. This eliminates the concern of having a first-order phase transition between the DFT reference state and the room temperature reference state. Half-metallic behavior was obtained when applying U_{eff} values of 3.5eV or 4.5eV to iron, where the primary effect of the change was to increase the magnetic moment of iron. However, in the case of $U_{\text{eff}} = 3.5\text{eV}$, it was not possible to determine the elastic properties and bulk lattice constant by changing the volume of the 8 formula unit supercell as it did not produce a smooth volume versus energy curve. This phenomenon was also encountered by Guo and Barnard [66] and occurred despite starting from previously converged results, increasing k-point mesh density, and decreasing convergence criteria. Instead, a primitive 14-atom unit cell was used for determining the lattice constant and bulk modulus. Values of the bulk properties calculated in this study and others are given in Table 3.5. The lowest energy ferrimagnetic configuration of spins occurs when the Fe ions in the

T₁ and T₂ sites are aligned ferromagnetically, while the Fe ions in the O₁ and O₂ layers are coupled antiferromagnetically to the tetrahedral sites. This arrangement of spins is in agreement with Refs. [28,29,93]. In the case of Magnetite, the minimum energy spin state will be written as $\uparrow [\downarrow\uparrow\downarrow] \uparrow$.

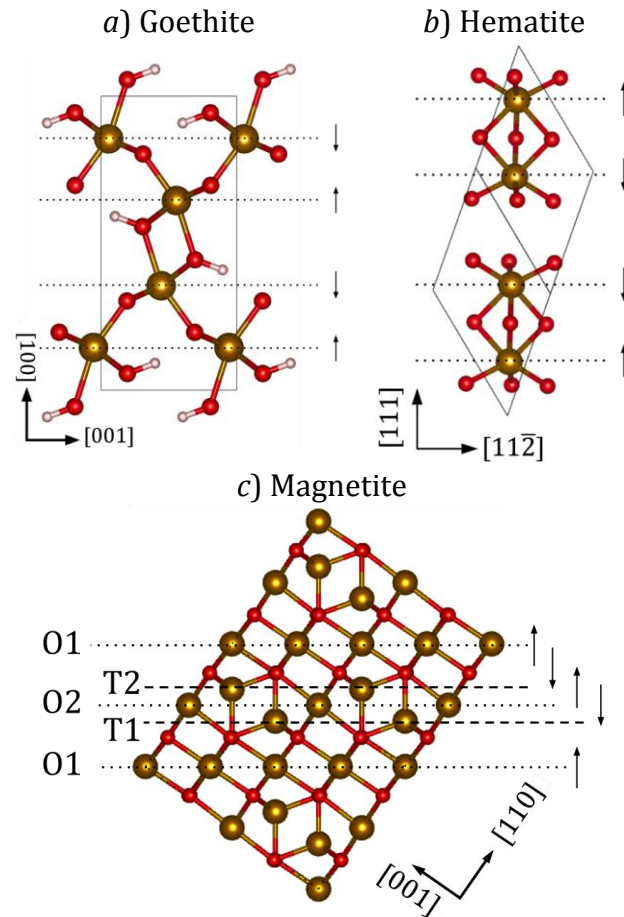


Figure 3.3 The figures show the orientation of spin magnetic moments of Fe (brown) layers separated by layers of O (red) in (a) Goethite (FeO(OH)), (b) Hematite (Fe₂O₃), and (c) Magnetite (Fe₃O₄). Note that the arrows indicate only the relative orientation of the spins (parallel or antiparallel) between the layers not their crystallographic alignment.

Table 3.5 Comparison of properties determined in this study and reported values of key structural, magnetic, and electrical properties of the Magnetite (Fe_3O_4) obtained from DFT calculations.

Magnetite Fe_3O_4 $\uparrow [\downarrow\uparrow\downarrow] \uparrow$	GGA+U This work $U_{\text{eff}} = 3.5\text{eV}$	GGA+U This work $U_{\text{eff}} = 4.5\text{eV}$	GGA+U [66] $U_{\text{eff}} = 4.5\text{eV}$	GGA+U [93] $U_{\text{eff}} = 3.8\text{eV}$	Experiment (See [93])
a (Å)	8.4883	8.4954	8.481	8.470	8.3956
B (GPa)	172.826	169.726	173.3	177.0	181
M_{net} ($\mu_B/\text{f. u.}$)	7.961	8.000	1.33	8.000	8.10
Fe(B) (μ_B)	3.933	3.980	-	-	-
Fe(A) (μ_B)	-4.042	-4.128	-	-4.017	3.82

Goethite (FeO(OH)) is an antiferromagnetic iron hydroxide ($T_N = 373\text{K}$) with the $Pbnm$ space group [97]. A comparison of calculated and reported properties of this mineral is given in Table 3.6. As with magnetite, the primary effect of increasing the value of U_{eff} is to increase the band gap and slightly increase the magnetic moment of iron. However, to match the band gap to experiment requires a substantially large U_{eff} value which causes further deviation from the experimental lattice constants.

Table 3.6 Comparison of properties determined in this study and reported values of key structural, magnetic, and electrical properties of Goethite (FeO(OH)) obtained from DFT calculations.

Goethite FeO(OH)	GGA+U This work $U_{\text{eff}}(\text{Fe}^{+3})$ $= 3.5\text{eV}$	GGA+U This work $U_{\text{eff}}(\text{Fe}^{+3})$ $= 4.5\text{eV}$	GGA+U [66] $U_{\text{eff}}(\text{Fe}^{+3}) =$ 4.5eV	GGA+U [98] $U_{\text{eff}}(\text{Fe}^{+3})$ $= 5.2\text{eV}$	Experiment [97]
a (Å)	10.094	10.042	10.040	10.150	9.951
b (Å)	3.059	3.043	3.045	3.084	3.018
c (Å)	4.653	4.629	4.628	4.646	4.598
E_g (eV)	1.731	2.072	-	2.5	2.5 [95]
B (GPa)	111.814	107.773	114.1	109	111
M_{net} (μ_B)	0.000	0.000	0.00	0.00	0.000
Fe^{+3} (μ_B)	± 4.174	± 4.255	-	± 4.16	-

3.1.2 Ferrite Spinels

Spinels are metals oxides with formula $(A_{1-x}, B_x)^{+2}(A_x, B_{2-x})^{+3}\text{O}_4$ that crystallize such that the oxygen ions form a face-centered cubic lattice, with partial filling of the interstices by metal ions. There are two types of partially occupied cation sites

including (A) tetrahedral sites of which only one eighth are occupied and (B) octahedral sites with only half of the total occupied. The x parameter can vary from 0 to 1, specifying the degree of inversion. Normal spinels ($x = 0$) have only divalent cations at the tetrahedral (A) sites and only trivalent cations at the octahedral (B) sites. Inverse spinels ($x = 1$) have all of their divalent cations on B sites and trivalent cations evenly distributed between A and B sites.

Nickel ferrite (NiFe_2O_4) has an inverse spinel structure, similar to magnetite, but with the Ni^{+2} ions occupying half of the otherwise Fe^{+2} octahedral sites. While experimental results indicate a random distribution of Ni^{+2} in the octahedral (B) sites, our structure distributes Ni^{+2} ions on the octahedral sites that maintain cubic symmetry within the $Im\bar{3}m$ space group. Fig. 3.4 shows the occupancy of octahedral sites on (001) planes labeled according to their distance along the c axis. In the case of nickel ferrite, silver spheres represent Ni^{+2} ions, brown spheres represent Fe^{+3} ions, and red spheres represent O^{2-} ions. Employing the notation defined in Fig. 3.1, nickel ferrite is ferrimagnetic ($T_N = 863\text{K}$) [99] with the spins of the O_1 and O_2 layer Fe^{+3} and Ni^{+2} ions aligned ferromagnetically, while the T_1 and T_2 layer Fe^{+3} ions are aligned antiferromagnetically, resulting in the $\uparrow [\downarrow\downarrow] \uparrow$ configuration.

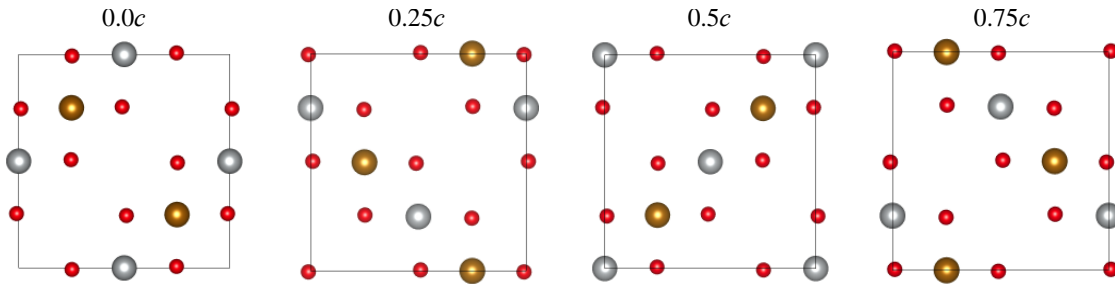


Figure 3.4 This figure shows the distribution of divalent metal cations (M^{+2}) in grey, trivalent iron (Fe^{+3}) in brown, and oxygen in red on (001) planes in an inverse spinel. The location of the plane along the c axis is indicated above each layer. Only planes that contain metal ions with octahedral coordination (B-sites) are shown.

This result is consistent with literature values, given in Table 3.7. It should be noted that the calculated band gap of nickel ferrite is much larger than the experimental value of 0.33eV [96]. However, Fritsch and Ederer [100] report other GGA+U studies calculating a value of approximately 1eV, including their own value of 0.97eV using $U_{\text{eff}} = 3\text{eV}$ for all metal ions.

Table 3.7 Comparison of properties determined in this study and reported values of key structural, magnetic, and electrical properties of the inverse spinel nickel ferrite obtained from DFT calculations.

nickel ferrite	GGA+U	GGA+U	GGA+U	Experiment
NiFe₂O₄	This work	This work	[100]	[101]
$\uparrow [\downarrow\uparrow] \uparrow$	$U_{\text{eff}}(\text{Ni}^{+2}) = 6.0\text{eV}$ $U_{\text{eff}}(\text{Fe}^{+3}) = 3.5\text{eV}$	$U_{\text{eff}}(\text{Ni}^{+2}) = 6.0\text{eV}$ $U_{\text{eff}}(\text{Fe}^{+3}) = 4.5\text{eV}$	$U_{\text{eff}}(\text{Ni}^{+2}) = 3.0\text{eV}$ $U_{\text{eff}}(\text{Fe}^{+3}) = 3.0\text{eV}$	
a (Å)	8.405	8.407	8.426	8.339
E_g (eV)	1.311	1.675	0.97	0.33 [96]
B (GPa)	173.156	174.547	177.1	198.2
M_{net} ($\mu_B/\text{f.u.}$)	2.005	1.797	1.72	2.09 [102]
Ni ⁺² (B) (μ_B)	1.705	1.708	1.58	2.22
Fe ⁺³ (B) (μ_B)	4.142	4.222	4.11	4.86
Fe ⁺³ (A) (μ_B)	-4.041	-4.133	-3.97	-4.73

Zinc ferrite (ZnFe₂O₄) is a normal spinel; all of the doubly charged cations are in tetrahedral (A) sites indicated by T₁ and T₂ layers in Fig. 3.1. Calculated magnetic properties of zinc ferrite are extremely sensitive to the oxygen position parameter (u) [27,103]. GGA+U simulations of Cheng [104] which use $U = 4.5\text{ eV}$ and $J = 0.97\text{ eV}$ applied only to the 3d orbital of iron, predict a different antiferromagnetic configuration which differs by 0.0225eV/f.u. from their reported ($\uparrow [\downarrow] \uparrow$) antiferromagnetic state. Zinc ferrite is typically reported to be antiferromagnetic with a Néel temperature of 10 to 13K. However, the existence of a long-range magnetic order has been questioned by Kamazawa, *et al.* [105], who found that in a high quality single crystal, no indication of antiferromagnetic order is found for temperatures as low as 1.5K (they argue that the often observed antiferromagnetic order is a result of sample inhomogeneity or defects). Usa *et al.* [106] find that third nearest-neighbor interactions are dominant. This could

be the source of the difficulty in capturing the behavior with DFT+U calculations, especially with an effective U value. A sample of studies with parameters similar to those used herein is shown in Table 3.8. In order to assure transferability, the U_{eff} parameter on iron and zinc is taken to be the same as used elsewhere in this study. The U_{eff} value applied to Zn^{+2} in the A-sites has very little effect on the structure and band gap due to the presence of a fully occupied $3d$ -orbital evidenced by the absence of a magnetic moment.

Table 3.8 Comparison of properties determined in this study and reported values of key structural, magnetic, and electrical properties of the normal spinel zinc ferrite (ZnFe_2O_4) obtained from DFT calculations.

zinc ferrite ZnFe_2O_4 $\uparrow [\downarrow\downarrow] \uparrow$	GGA+U This work $U_{\text{eff}}(\text{Zn}^{+2})$ = 4.7eV $U_{\text{eff}}(\text{Fe}^{+3})$ = 3.5eV	GGA+U This work $U_{\text{eff}}(\text{Zn}^{+2})$ = 4.7eV $U_{\text{eff}}(\text{Fe}^{+3})$ = 4.5eV	GGA+U This work $U_{\text{eff}}(\text{Zn}^{+2})$ = 0.0eV $U_{\text{eff}}(\text{Fe}^{+3})$ = 4.5eV	GGA+U [104] $U(\text{Zn}^{+2})$ = 0.0eV $U(\text{Fe}^{+3})$ = 4.5eV $J(\text{Fe}^{+3})$ = 0.97eV	Experiment
a (Å)	8.4887	8.4843	8.4933	8.52	8.52 [105]
E_g (eV)	1.539	1.821	1.797	-	0.2 [107]
B (GPa)	161.309	161.244	162.461	-	-
M_{net} (μ_B /f.u.)	0.0	0.0	0.0	0.0	0.0
Zn^{+2} (A) (μ_B)	0.0	0.0	0.0	0.0	0.0
Fe^{+3} (B) (μ_B)	± 4.212	± 4.284	± 4.281	$\pm 4.1\sim 4.2$	± 4.2 [108]

Cobalt ferrite (CoFe_2O_4) is a ferrimagnetic inverse spinel. The divalent Co cations In this ferrite, the inverse (Table 3.9) and normal configurations (Table 3.20) are very close in energy and the choice of U_{eff} for both iron and cobalt effects which structure is more stable; the near degeneracy in energy is found despite the substantial differences in the structural, electrical, and magnetic properties. The site preference energy for the inverse spinel is variously reported as 0.2 eV/f.u. [109], and 0.339 eV/f.u. [110] in DFT+U studies. The current calculation scheme with $U_{\text{eff}}(\text{Fe}^{+3}) = 3.5\text{eV}$ results in the inverse spinel being more stable than the normal spinel by 0.1eV/f.u., but with

$U_{\text{eff}}(\text{Fe}^{+3}) = 4.5\text{eV}$ the normal spinel is more stable than the inverse spinel by 0.015eV/f.u. Testing has shown that varying the U_{eff} value of Fe has a larger effect on the electronic and structural properties than comparable variation in the Co value. With $U_{\text{eff}}(\text{Fe}^{+3}) = 4.5\text{eV}$, varying the U_{eff} of cobalt from 2.5 to 5.5eV will predict the structures are equally stable at $\sim 4.7\text{eV}$, but the inverse configuration is never more stable. In contrast, with $U_{\text{eff}}(\text{Co}^{+2}) = 3.3\text{eV}$, the inverse configuration is more stable over the range of iron U_{eff} from 3.3–4.0eV.

Table 3.9 Comparison of properties determined in this study and reported values of key structural, magnetic, and electrical properties of the *inverse* spinel cobalt ferrite (CoFe_2O_4) obtained from DFT calculations are placed according to Fig. 3.4.

cobalt ferrite CoFe₂O₄ ↑ [↓↑↓] ↑ Inverse Spinel	GGA+U This work $U_{\text{eff}}(\text{Co}^{+2}) =$ 3.3eV $U_{\text{eff}}(\text{Fe}^{+3}) =$ 3.5eV	GGA+U This work $U_{\text{eff}}(\text{Co}^{+2}) =$ 3.3eV $U_{\text{eff}}(\text{Fe}^{+3}) =$ 4.5eV	GGA+U [100] $U_{\text{eff}}(\text{Co}^{+2}) =$ 3.0eV $U_{\text{eff}}(\text{Fe}^{+3}) =$ 3.0eV	GGA+U [110] $U_{\text{eff}}(\text{Co}^{+2}) =$ 3.29eV $U_{\text{eff}}(\text{Fe}^{+3}) =$ 3.42eV	Experiment [101]
a (Å)	8.449	8.4514	8.463	8.384	8.392
E_g (eV)	0.986	1.171	0.9	0.72	0.11 [96] 0.55 [111]
B (GPa)	171.141	171.402	172.3	-	185.7
M_{net} (μ_B /f.u.)	2.972	2.965	3	3	3
$\text{Fe}^{+3}(\text{A})$ (μ_B)	-4.022	-4.115	-3.98	-3.97	-
$\text{Fe}^{+3}(\text{B})$ (μ_B)	4.135	4.216	4.10	4.10	-
$\text{Co}^{+2}(\text{B})$ (μ_B)	2.627	2.630	2.62	2.61	-

Table 3.10 Comparison of properties determined in this study and reported values of key structural, magnetic, and electrical properties of cobalt ferrite (CoFe_2O_4) in the *normal* spinel configuration obtained from DFT calculations.

cobalt ferrite CoFe₂O₄ ↑ [↓↑↓] ↑ Normal Spinel	GGA+U This work $U_{\text{eff}}(\text{Co}^{+2}) =$ 3.3eV $U_{\text{eff}}(\text{Fe}^{+3}) =$ 3.5eV	GGA+U This work $U_{\text{eff}}(\text{Co}^{+2}) =$ 3.3eV $U_{\text{eff}}(\text{Fe}^{+3}) =$ 4.5eV	GGA+U [109] $U_{\text{eff}}(\text{Co}^{+2}) =$ 3.0eV $U_{\text{eff}}(\text{Fe}^{+3}) =$ 3.0eV	GGA+U [110] $U_{\text{eff}}(\text{Co}^{+2}) =$ 3.29eV $U_{\text{eff}}(\text{Fe}^{+3}) =$ 3.42eV
a (Å)	8.504	8.497	8.52	8.308
E_g (eV)	0.493	0.472	0.45 (direct)	0.09
M_{net} (μ_B /f.u.)	6.838	6.88	5.67	7.0
$\text{Fe}^{+3}(\text{B})$ (μ_B)	4.202	4.265	4.06	4.12
$\text{Co}^{+2}(\text{A})$ (μ_B)	-2.558	-2.573	-2.45	-2.42

3.2 Calculating Effective Chemical Potentials

This approach starts with the assumption that the ECPs determined by solving the linear equations for the reactions denoted by Eqns. (2.1)–(2.9) can be used to extrapolate DFT energies at 0K for related structures to free energies at higher temperatures. Implicit in this assumption is that the U_{eff} values depend only on the element and not on its charge/spin state or its environment. As stated earlier, this assumption is tested by determining a unique set of ECP values from Eqns. (2.1)–(2.6) (the binary metal oxides) only, and then using these values (which we term the ‘partial fit’) to predict free energies for the three mixed oxides (Eqns. (2.7)–(2.9)). The first-principles values needed are the energies of the oxides, calculated with the GGA+U functional at absolute zero, $E_{M_xO_y}(0\text{K})$, are given in Table 3.11.

Table 3.11 The minimum energies of the structures calculated with the GGA+U approach at 0K, along with the k-space mesh density used.

Material	Formula	k-point mesh	$E_{M_xO_y}(0\text{K})$ (kJ/mol)	
			$U_{\text{eff}}(\text{Fe})=3.5\text{eV}$	$U_{\text{eff}}(\text{Fe})=4.5\text{eV}$
Hematite	$\alpha\text{Fe}_2\text{O}_3$	5×5×5	-3356.8447	-3291.3355
Magnetite	Fe_3O_4	5×5×5	-4697.8421	-4593.7907
Goethite	$\alpha\text{FeO}(\text{OH})$	4×6×4	-2393.7212	-2362.9603
Nickel oxide	NiO	9×9×9	-979.8389	-979.8389
Nickel ferrite	NiFe_2O_4	7×7×7	-4358.9149	-4290.5529
Zinc oxide	ZnO	11×11×11	-864.7077	-864.7077
Zinc ferrite	ZnFe_2O_4	5×5×5	-4218.2004	-4160.9124
Cobalt oxide	Co_3O_4	5×5×5	-4110.2767	-4110.2767
Cobalt ferrite	CoFe_2O_4	5×5×5	-4551.1972	-4481.6866

The resulting fit is plotted as dotted lines in Fig. 3.5, which contains the calculated free energies of formation of zinc, cobalt and nickel ferrite for two different values of $U_{\text{eff}}(\text{Fe})$. This can be compared to the experimental values, which are indicated by the solid lines. The agreement between the calculated and experimental values for NiFe_2O_4 and CoFe_2O_4 is excellent for both values of $U_{\text{eff}}(\text{Fe})$. For ZnFe_2O_4 the largest deviation for the smaller value of $U_{\text{eff}}(\text{Fe})$ is 2.9% (see Table 3.12), which is reduced to 1.9% for the

higher $U_{\text{eff}}(\text{Fe})$ value. Overall this is a very encouraging result, and suggests that these assumptions are valid for the purpose of predicting free energies at high temperatures.

A 'global fit' for the ECP values is determined by finding the ECP values that produce the best fit to Eqns. (2.1)–(2.9), in a least-squares sense. The result is given by the dashed lines in Fig. 3.5 and by the values in Table 3.12. This improves the fit between the calculated and experimental free energies for the ZnFe_2O_4 structure, but at the expense of a slightly worse fit between the experimental and calculated free energies for CoFe_2O_4 and ZnFe_2O_4 . Overall, however, the agreement is excellent.

Comparison of the errors in Table 3.12 between systems fit with the two iron U_{eff} values indicates that there is a trade-off present between the accuracy of the fit to the free energies of formation and matching the experimentally observed properties of specific materials. For example, using $U_{\text{eff}}(\text{Fe}) = 3.5 \text{ eV}$ predicts the correct (inverse) structure for CoFe_2O_4 , at the expense of the accuracy of the fits to all of the materials in the system. However, a judicious choice of U_{eff} must be made to satisfy the greatest number of properties of most relevance to the application. To predict free energies of formation and surface energies of oxides and mixed metal spinels, the global fit with $U_{\text{eff}}(\text{Fe}) = 4.5 \text{ eV}$ is used for the results discussed below. The value of the chemical potentials are reported in Appendix A. The ECPs are fit to Eq. (A.1) using coefficients provided in Table A.1.

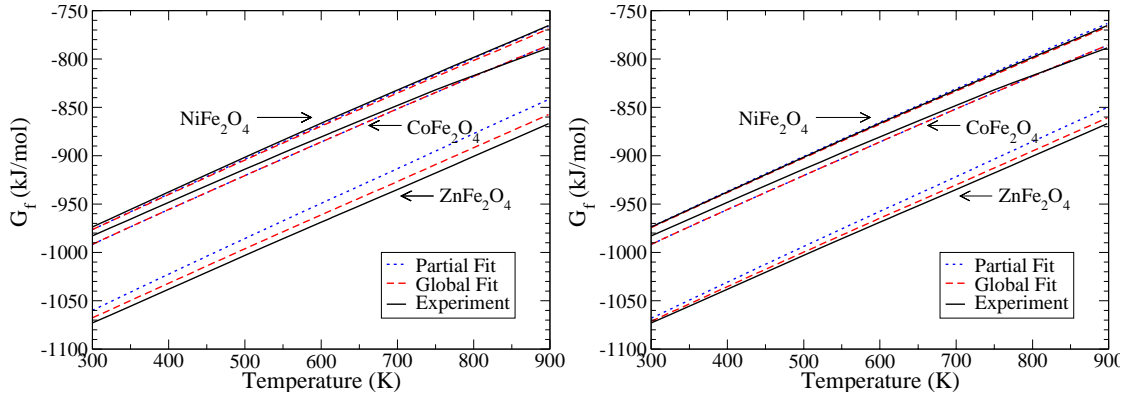


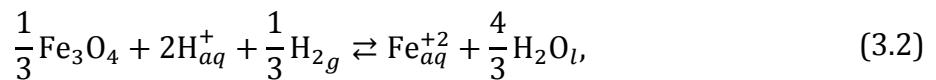
Figure 3.5 Prediction of the free energies of formation for zinc, cobalt, and nickel ferrite are plotted as determined from the partial and global fit with experimental values as a reference (see Table 3.12). The resulting fits for both $U_{\text{eff}}(\text{Fe}) = 3.5\text{eV}$ (left) and $U_{\text{eff}}(\text{Fe}) = 4.5\text{eV}$ (right) are plotted.

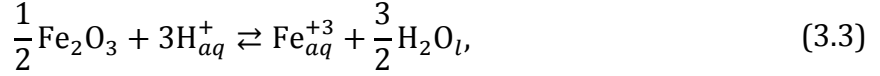
Table 3.12 Comparison of the error incurred using the two fitting approaches to test the transferability of the first-principles results from single species metal oxides to mixed metal oxides. MAE is the maximum absolute error of the fit. The source of experimental data for the Gibbs free energy of formation is indicated by superscript number after the material name: (1) JANAF [112]; (2) Pankratz [113]; (3) Barin [114]; (4) Knacke [115].

Material	Formula	$U_{\text{eff}}(\text{Fe}) = 3.5\text{eV}$				$U_{\text{eff}}(\text{Fe}) = 4.5\text{eV}$			
		Global Fit R ²	Partial Fit MAE (%)	Global Fit R ²	Partial Fit MAE (%)	Global Fit R ²	Partial Fit MAE (%)	Global Fit R ²	Partial Fit MAE (%)
Hematite ¹	$\alpha\text{Fe}_2\text{O}_3$	0.99	1.04	-	-	0.99	0.81	-	-
Magnetite ¹	Fe_3O_4	0.99	0.007	-	-	0.99	0.00	-	-
Goethite ¹	$\alpha\text{FeO}(\text{OH})$	1.00	0.00	-	-	1.00	0.00	-	-
Nickel oxide ²	NiO	0.96	2.15	-	-	0.99	0.82	-	-
Nickel ferrite ³	NiFe_2O_4	0.99	0.44	0.99	2.70	0.99	0.17	0.99	0.28
Zinc oxide ⁴	ZnO	0.80	3.65	-	-	0.93	2.33	-	-
Zinc ferrite ³	ZnFe_2O_4	0.98	1.09	0.90	2.89	0.99	0.70	0.96	1.94
Cobalt oxide ¹	Co_3O_4	0.99	0.005	-	-	0.99	0.00	-	-
Cobalt ferrite ³	CoFe_2O_4	0.99	0.90	0.99	0.91	0.99	0.90	0.99	0.89

3.2.1 Validation

To validate the aqueous chemistry, theoretically derived values for the first solubility constants (K_{s0}) of the binary oxides are compared to experimental data. The solubility of the metal oxides is defined by the reactions:





The subscripts on the species indicate whether it is aqueous (*aq*), liquid-phase (*l*), gas-phase (*g*) or solid (none). The solubility coefficient is defined by $K_{s0} = \exp\left(-\frac{\Delta G_R}{RT}\right)$ where the reaction free energy ΔG_R is determined by Eqs. (3.1)–(3.4) using the ECP values obtained from Eqs. (2.11)–(2.13). The experimental values of the solubility are taken from Ref. [80] and are compared in Fig. 3.6 with those derived using the global ECP values. The overall agreement between calculated and measured values is excellent; this illustrates the ease with which the scheme above can incorporate solution phase chemistry provided that experimental data is available.

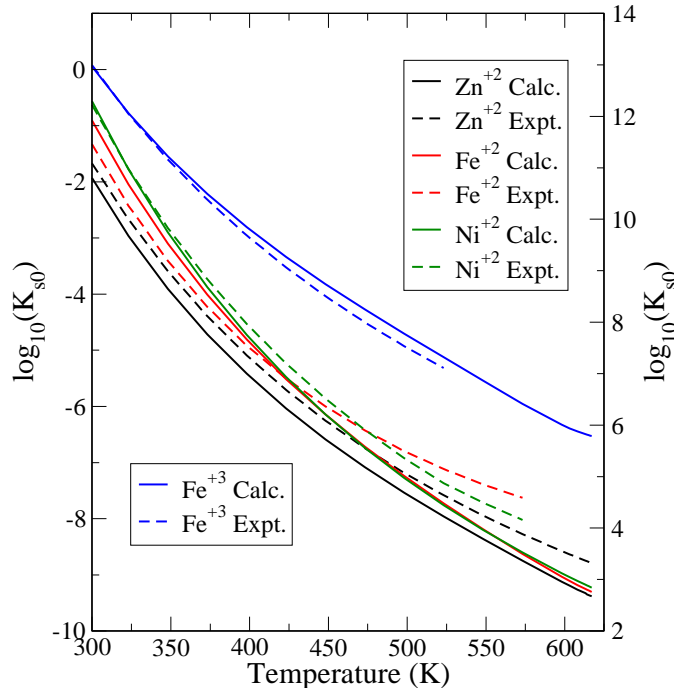


Figure 3.6 Comparison of the predicted (solid lines) and measured (dashed lines) first solubility constants of various metal oxides according to Eqs.(3.1)–(3.4).

3.3 Survey of Prior Work Investigating the Surface Structure of Spinel and Oxides

First-principles determination of surface structure and energy in aqueous environments has been previously explored. A number of studies regarding metal oxide surface stability in gas and liquid water are found in the literature, including Anatase/Rutile (TiO_2) [58,60,116,117], Co_3O_4 [55,118], Goethite [98,119,120], Magnetite [120–123], and Hematite [53,54,119]. Related studies on NiO considered only the (111) surface [84,124].

3.3.1 Survey of Nickel Oxide Surface Investigations

For NiO, the present investigation considers (100), (110), and (111) surfaces that are denuded as well as terminated with associatively adsorbed and dissociated water molecules. NiO (100) is a stoichiometric Tasker type I surface [125]. Simulations [126] and experiments [127] indicate that water does not dissociate on the planar surface, but apparently occurs on roughened or defected surfaces [128]. Films grown at high temperatures in vacuum show (100) surfaces, while (111) surfaces are found at lower growth temperatures ($T < 300\text{K}$). Owing to the relative thermodynamic stability, it is found that heating to remove hydroxyl groups from (111) surfaces will cause a transition to the (100) surface [129,130]. Consistent with the relative stability of the (100) surface at high temperature, annealing at 500K found that the denuded (100) surface occupied 93% of the surface with the remainder being hydroxylated (111) with a $p(1 \times 1)$ unit cell [127].

NiO (111) is a Tasker type III charged polar surface [125] that is inherently unstable due to the divergence of the electrostatic energy at the surface. Consequently, it will undergo reconstruction or adopt a terminating layer to eliminate the dipole. Observations have demonstrated that the dipole is eliminated through faceting or reconstruction; however there is disagreement over the exact structure. NiO (111) surfaces grown from gaseous oxygen exhibit the $p(2 \times 2)$ octopolar reconstruction proposed by Wolf [131]. Both O and Ni-terminated octopoles have been observed on thin films [127,132–134], while only Ni-terminated octopoles have been observed on air-annealed NiO

single crystals [135]. A faceted reconstruction is found in NiO films grown electrochemically in acid [136,137] and is observed to form 2–3 nm wide steps tilted at approximately 8° from the Ni (111) substrate. The faceted reconstruction also has been observed on films annealed in or exposed to humid air where it is suggested that the octopole reconstruction is unstable [124]. The tilted facets can cancel the surface dipole as explained in the model of Maurice, *et al.* [136] Further conflicting evidence comes from a study that reported that a (111) surface, exposed to liquid water, forms a single layer of β -Ni(OH)₂ [127]. Other studies indicate that the oxygen terminated octopolar surface is stable in extremely low-pressure gas-phase water [132] while computational studies using the MSINDO approach have suggested that water may dissociate on the octopolar NiO (111) surface [126,130]. There is agreement between the experimental work of Warren and Thiel [138] and the results of Ciston, *et al.* [124], which predicts that the OH planar ($p(1 \times 1)$ hydrogen terminated surface) is the thermodynamically stable surface in the presence of water.

3.3.2 Survey of Spinel Surface Investigations

Existing computational investigations on mixed metal oxide spinels are limited to only a few compounds with the spinel structure: Fe₃O₄ [67,93,122,139–148], Co₃O₄ [55,118], BaZr₂O₄ [149], and ZnCr₂O₄ [56]. The surface of the spinel MgAl₂O₄ [57] is limited by the presence of Tasker type III (polar) surfaces [125] present for all cuts along the {111}, {110}, and {100} surfaces. The authors note that another mechanism of dipole elimination may be present in spinels containing metals with multiple oxidation states. In the case of spinels (such as nickel ferrite) containing metals with multiple oxidation states (Fe⁺², Fe⁺³) it is also possible to have an electronic reconstruction of the surface to eliminate the dipole [56]. This mechanism is not present in all spinels, such as MgAl₂O₄, as Al and Mg do not have other formal oxidation states that could be formed to eliminate the surface dipole.

The only study available considering nickel ferrite surfaces was conducted by Kumar, *et al.* [150], who used DFT calculations to predict the surface energy of three of the possible non-stoichiometric (111) surfaces in the presence of oxygen gas. The study

also reports the structure and adsorption energy of water on the surfaces and determines that the dissociation of water on the surfaces is thermodynamically favorable.

Due to the structural similarity to nickel ferrite, Magnetite will be used as an analogue for the study of surfaces. Herein, all nickel ferrite and Magnetite (111) surfaces will refer to the planes indicated in Fig. 3.11e. There is a large body of literature regarding the surface structure and stability of iron oxides but very little involving nickel ferrite. For Magnetite crystals, the (111) surface is the most stable, but there exist many possible terminations which undergo substantial relaxation because any surface with bulk ion positions is polar. The two most stable surfaces discussed in literature are where either the O₂ (D) T₁ (E) Fe layers are exposed forming ½ and ¼ monolayer Fe terminated surfaces, respectively. A first-principles thermodynamics study utilizing GGA+U by Grillo, *et al.* [93], found that the ¼ monolayer (E) termination is favorable in the presence of oxygen with partial pressures of up to 10¹³ Bar from 298-1200 K, when compared to A and D terminations. This surface has also been reported in experimental studies to be stable in vacuum [146–148]. Extrapolating the results of Grillo, *et al.*, to vacuum results in agreement with Martin, *et al.* [145], of the most stable surface having the D termination. A study using LSDA+U with first-principles thermodynamics [67] predicted the ½ monolayer (D) of Fe to be stable in vacuum but found that in an oxygen rich environment, the oxygen terminated A' surface becomes stable. The ½ monolayer surface was also found to be most favorable in vacuum by a study employing exact exchange with a PW91 correlation term [144].

Molecular Dynamics simulations by Kundu, *et al.* [143], determined that the lowest energy cut on the (110) and (011) surface occurs when only octahedral sites are on the surface, while the minimum surface energy of the (101) face occurs when the tetrahedral and octahedral iron atoms are on the surface. The (100) plane of Magnetite with a surface equivalent to the C cut of nickel ferrite as shown in Fig. 3.11a, where Fe ions in tetrahedral sites make up the topmost partial layer, was modeled and a recon-

struction was found when using MD simulations [141]. The reconstructed surface incorporates the Fe ion in the tetrahedral sites lying the C and C' planes into the B plane.

For extremely small oxygen partial pressures above ~ 220 K Grillo, *et al.*, reports that the $p(1 \times 1)$ E surface of the (111) plane with a single water molecule dissociatively absorbed is the more stable than the $p(2 \times 2)$ surface with two water molecules where one is associatively absorbed and another is dissociatively absorbed. Experiments on (111) surfaces prepared and tested in a humid environment showed a surface consisting of 75% A' and 25% A termination [140]. However, the A type surface is missing all of the Fe ions in the C (T_2) layer. No evidence for an ordered water layer on the Magnetite (100) or (111), but hydroxyl termination is likely [139,140]. Hydroxyl groups may be present at depths of up to 8\AA from the surface, but XPS measurements indicate the formation of Goethite at the surface.

Molecular Dynamics simulations [143] of the (110) surface of Magnetite show that half of the tetrahedral Fe ions near the surface are removed from the bulk and appear to be attached to the surface via an OH bridge. MD simulations [143] of the (110) surface of Magnetite show that half of the tetrahedral Fe ions near the surface are removed from the bulk and appear to be attached to the surface via an OH bridge.

3.4 Present Investigation into the Surface Structure of Nickel Oxide and Nickel Ferrite

The surface energies of oxides investigated in this work rely on accurate calculation of the surface energy and determination of possible reconstructions. The most commonly observed crystal planes in experimental work (which include the (100), (110), and (111) planes) are surveyed for low energy surfaces. In order to limit the already high computational cost, this study is limited to consideration of surface reconstructions of up to a $p(2 \times 2)$ surface cell. However, as discussed in the literature review of the previous section, experimental observations indicate that reconstructions of these surfaces rarely have surface unit cells exceeding the limit assumed in this work.

3.4.1 Nickel Oxide

The surface structure and terminations of the NiO (100) and (110) surfaces considered in this study are illustrated in Figs. 3.7–3.9. A full monolayer of water can be either adsorbed associatively or be dissociated on the (100) surface, but simulations revealed that water is only stable when it dissociates on the (110) surface.

Illustrated in Fig. 3.10 are the various reconstructions of the NiO (111) surfaces examined in the present study. The Ni-octopole (*a*) and O-octopole (*b*) is the same $p(2 \times 2)$ reconstruction proposed by Wolf [131] for Tasker type III surfaces and observed to form during oxidation of Ni (111) in ultrahigh vacuum conditions. In the presence of water, multiple terminations are possible. One possibility, which has a $p(1 \times 1)$ surface structure, suggested by experimental results [138], is illustrated in (*c*) which can be envisioned as a (111) plane consisting of Ni atoms forming a surface terminated with hydroxyl groups where the oxygen atoms are placed at the sites of oxygen ions in the bulk. Various surfaces with partial hydroxyl-group coverage leading to a $p(2 \times 2)$ symmetry (*d–f*) were proposed by Ciston, *et al.* [124], and considered in this study. In agreement with Ciston, *et al.*, it is found that surfaces with partial hydroxyl coverage have higher surface energies than fully hydroxylated surfaces.

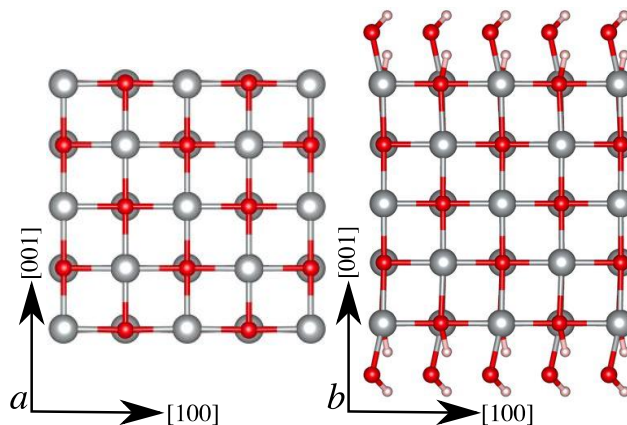


Figure 3.7 Structures of the (100) surfaces of NiO are illustrated in the (*a*) denuded case and (*b*) with a full monolayer of water that has dissociated. Nickel atoms are colored silver, oxygen is red, and hydrogen is white.

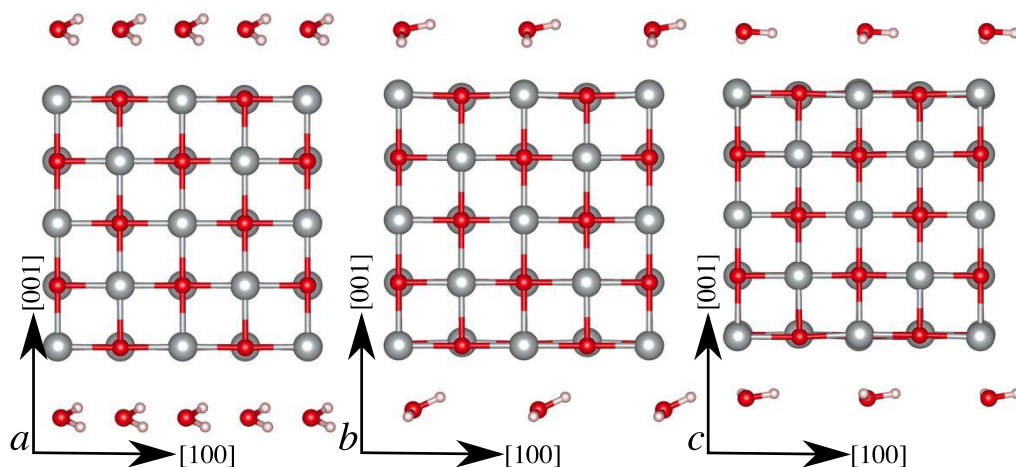


Figure 3.8 Surface structures of the (100) surfaces of NiO are illustrated with (a) 1, (b) 0.5, and (c) 0.25 monolayers of molecular water associatively adsorbed on the surface. Nickel atoms are colored silver, oxygen is red, and hydrogen is white.

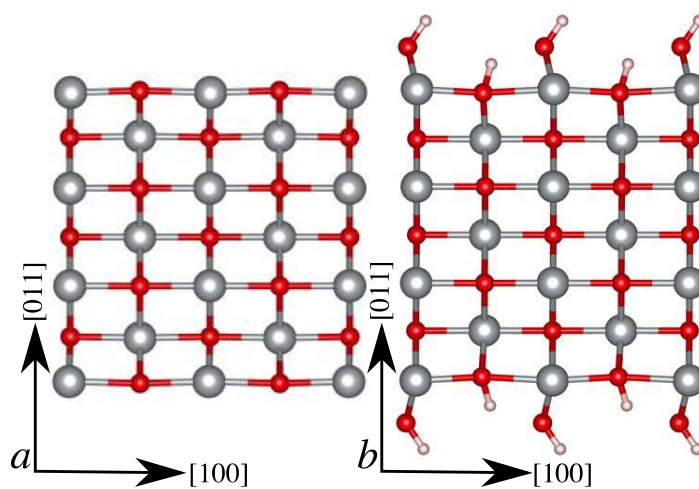


Figure 3.9 Structures of the (110) surfaces of NiO are illustrated in the (a) denuded case and (b) with a full monolayer of water that has dissociated. Nickel atoms are colored silver, oxygen is red, and hydrogen is white.

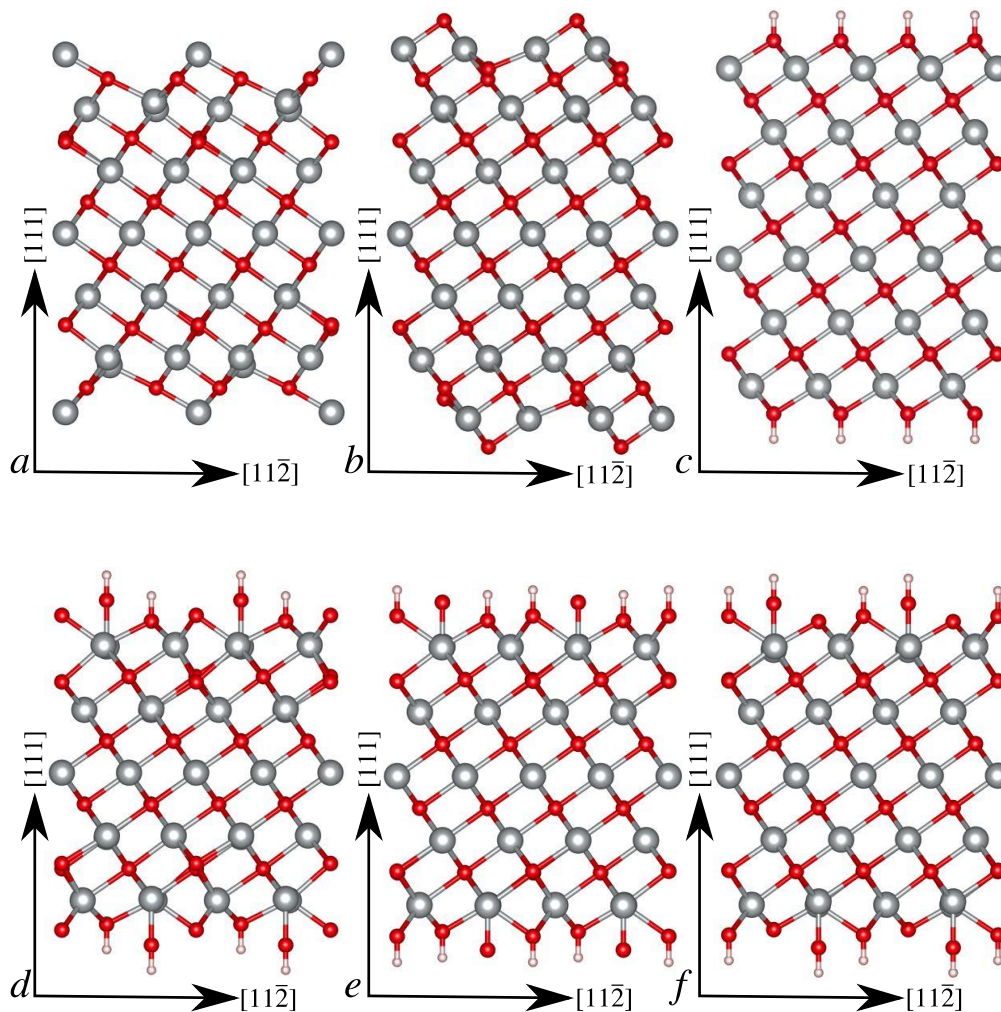


Figure 3.10 Reconstructed NiO (111) surfaces are illustrated with various reconstructions as described in the text. Nickel atoms are colored silver, oxygen is red, and hydrogen is white. Surfaces (a, b, d-f) exhibit the $p(2 \times 2)$ -type reconstruction, while (c) has $p(1 \times 1)$ surface symmetry.

3.4.2 Nickel Ferrite

Lacking experimental data regarding the structure or stability of nickel ferrite surfaces as a guide to those that might be ruled out as unstable or high energy, all possible surfaces were examined. The surfaces examined in this work are defined by the cuts labeled with a letter along the low index planes including (001), (110), (011), (101), and (111) as illustrated in Figs. 3.11a–3.11e, respectively.

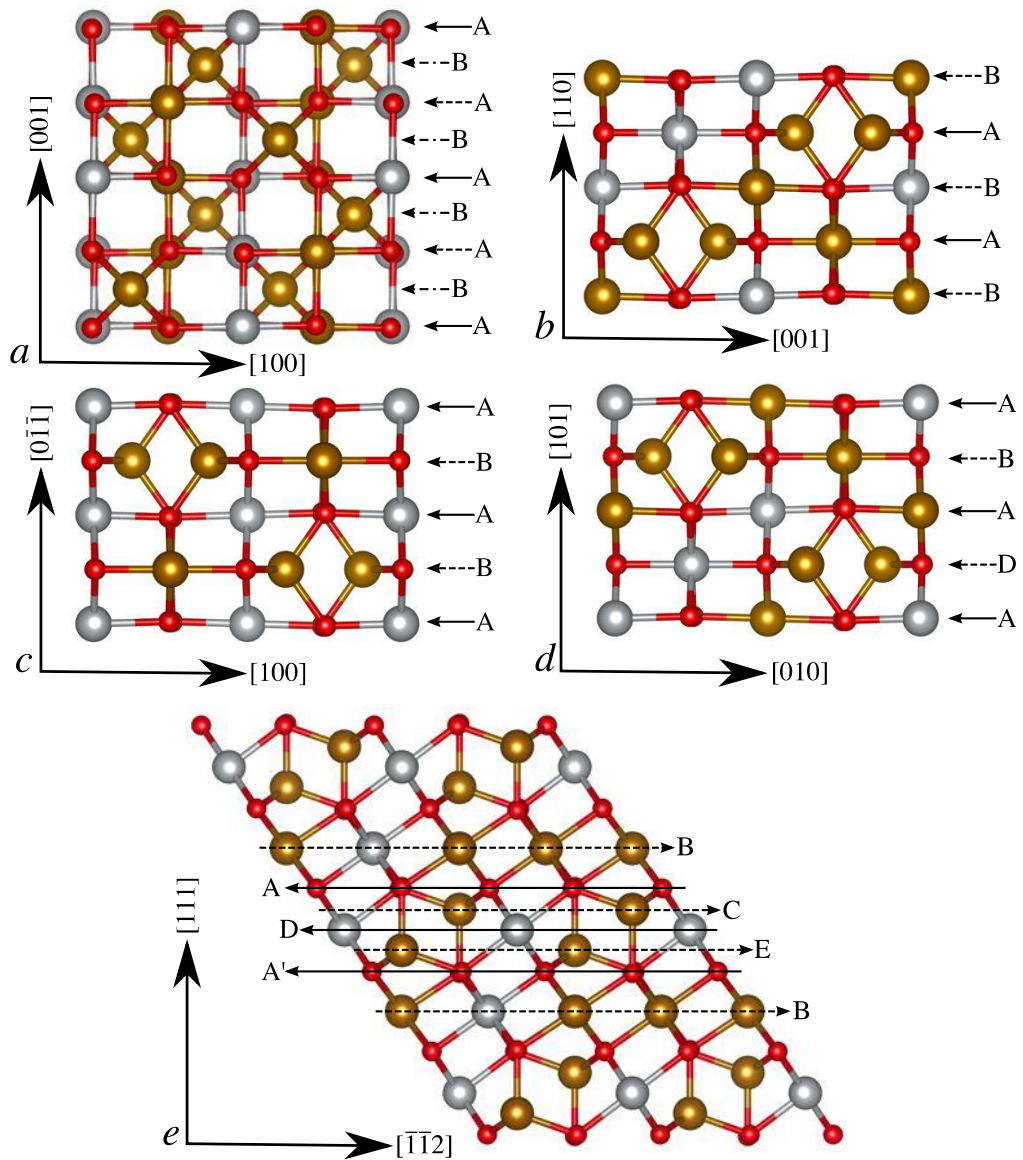


Figure 3.11 Views parallel to the NiFe₂O₄ surfaces investigated herein showing the planes where surfaces are generated. The planes investigated are the (a) (001), (b) (110), (c) (011), (d) (101), (e) (111). Surfaces are identified by both a plane index and a letter (A-E), which indicates the surface cut. The Ni²⁺ (grey), Fe²⁺/Fe³⁺ (brown), and O²⁻ (red) spheres represent the position of the ions.

In the case of nickel ferrite with the cation distribution described by Fig. 3.4, the (b) (110), (c) (011), and (d) (101), shown in Fig. 3.11, are unique surfaces. However, in reality, the Ni cations will be randomly distributed on the octahedral sites making these three surfaces identical. Projections of the denuded surfaces investigated in this study

are provided in Figs. 3.12–3.16 where Fe atoms are colored brown, Ni atoms are colored gray, and O is colored red. Note that more than one supercell is shown in each of the projected surfaces.

Only the stoichiometric surfaces on the (001) (Fig. 3.12c), (011) (Fig. 3.13c), and (111) planes (Figs. 3.16a, 3.16b, 3.20a, and 3.20b) contain defects. Due to the presence of defects, these surfaces are not unique and calculations were performed on the smallest possible surface cell.

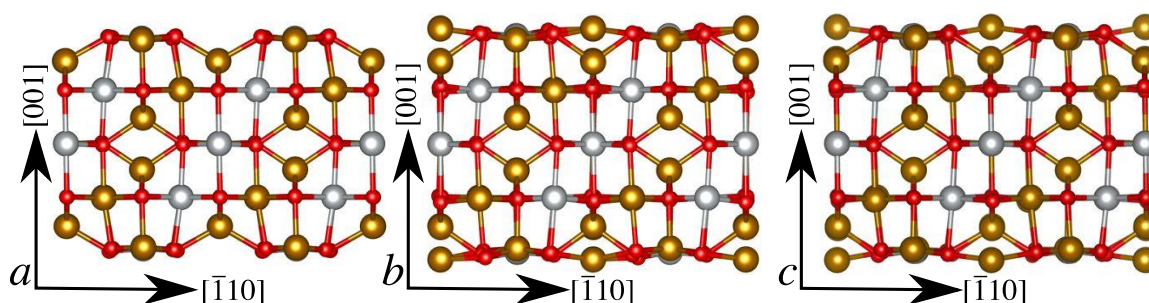


Figure 3.12 Denuded (001) surfaces of NiFe_2O_4 with terminations defined by Fig. 3.11a: (a) A, (b) B, and (c) is the stoichiometric surface.

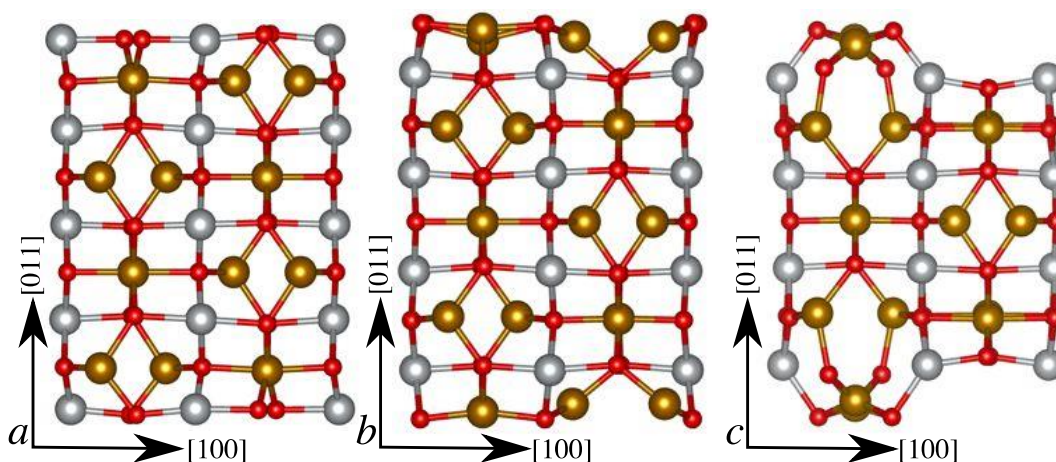


Figure 3.13 Denuded (011) surfaces (a) A, (b) B, as defined in Fig. 3.11c, and (c) is the stoichiometric surface.

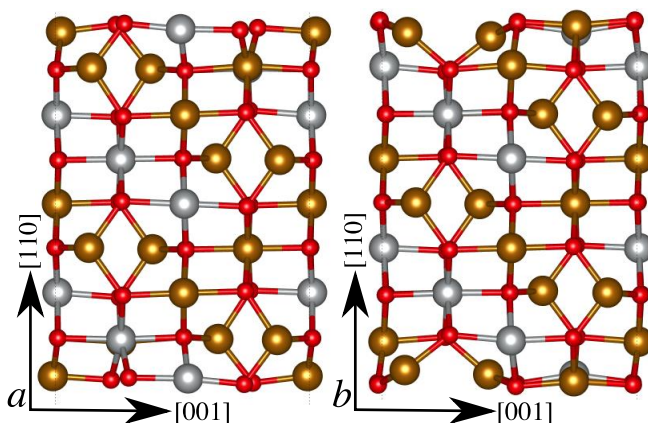


Figure 3.14 Denuded (110) of NiFe_2O_4 with terminations defined by Fig. 3.11b: (a) A, and (b) is B.

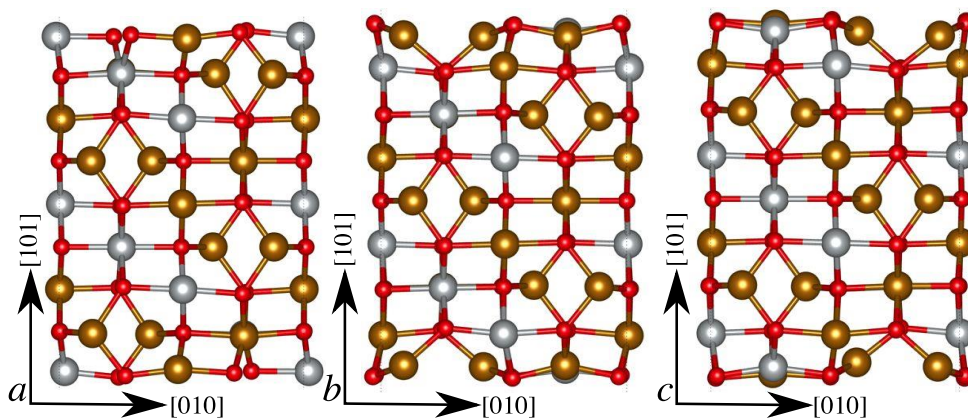


Figure 3.15 Denuded (101) surfaces of NiFe_2O_4 with terminations defined by Fig. 3.11d: (a) A, (b) B, and (c) D.

Surfaces represented in Figs. 3.15b and 3.15c are structurally very similar and have the same number of cations and oxygen ions but differ in how they are arranged. These surfaces differ by 0.0991eV (9.5609kJ/mol) per formula unit. In fact, treating nickel ferrite as a disordered inverse spinel would erase the differences between these surfaces altogether.

In the case of the denuded (111) planes, surface A and A' (Figs. 3.16a and 3.16b, respectively) differ as to the next layer such that in A surfaces, the next layer is the T_2 layer, while A' surfaces have an O_1 site as the next layer.

Few surfaces investigated were found to have stable hydroxyl terminated surfaces. Only projections of the surfaces with stable terminated surfaces are illustrated in Figs. 3.17 and 3.20, where Fe atoms are colored brown, Ni atoms are colored gray, H atoms are colored pink, and O is colored red. Note that no (100) planes could be found with a stable terminated surface. In each case, multiple configurations were attempted including attaching OH groups onto all surface metal atoms and H to all surface oxygen atoms, attaching hydrogen onto surface oxygen atoms, and attaching OH groups to surface metals alone. In the figures and tables, surfaces with an integer number of water molecules are denoted by appending 1ML to the surface identifier indicating the dissociative adsorption of a full monolayer of water. Surfaces denoted as having 'partial' terminations have a mix of water and H₂ dissociatively adsorbed on the surface.

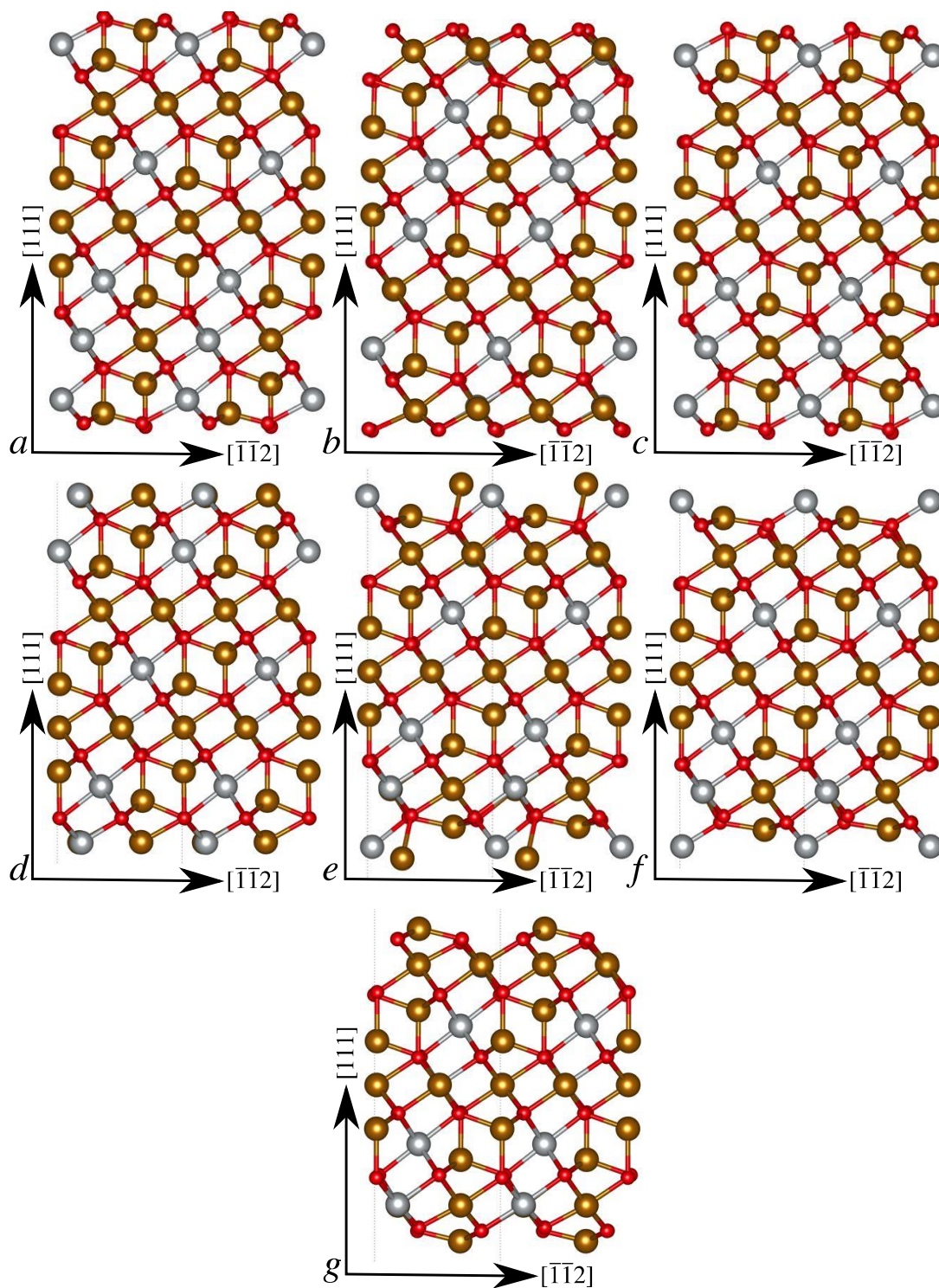


Figure 3.16 Denuded (111) surfaces of NiFe_2O_4 where Fe (brown), or Ni (gray) layers are separated by layers of O (red), as described in the text. Terminations are defined by Fig. 3.11e: (a) A, (b) A', (c) Stoichiometric, (d) B, (e) C, (f) D, and (g) E.

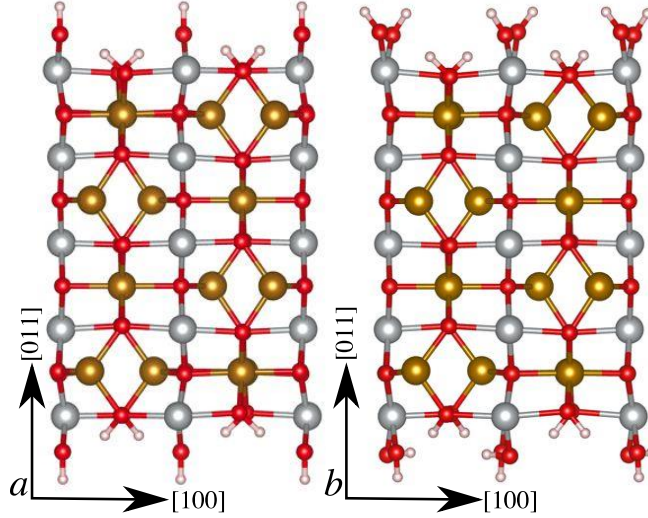


Figure 3.17 This figure shows all of the terminated (011) (a) A with 4 H₂O and 2 H₂ molecules, (b) A with one monolayer of water.

The adsorption energy of water is defined as

$$E_{\text{ads}} = E_{\text{slab}+n\text{H}_2\text{O}} - E_{\text{slab}} - n\mu_{\text{H}_2\text{O}}, \quad (3.5)$$

where n is the number of water molecules dissociated on the surface and $\mu_{\text{H}_2\text{O}}$ is the chemical potential of water. The quantity defined by Eq. (3.5) can be calculated for those surfaces which are covered by an integer number of water molecules of which only a few surfaces are available.

Table 3.13 The energy of adsorption (Eq. (3.5)) for water on various nickel ferrite surfaces with respect to the energy of an isolated water molecule at 0K, where $E_{\text{H}_2\text{O}}(0\text{K}) = -14.2188\text{eV}$, or a water molecule in liquid at 298.15K ($\mu_{\text{H}_2\text{O}}(298\text{K})$).

	E_{ads} from $E_{\text{H}_2\text{O}}(0\text{K})$ [kJ/mol]	E_{ads} from $\mu_{\text{H}_2\text{O}}(298\text{K})$ [kJ/mol]
(111)As	-168.755	-108.549
(111)D	-97.411	-37.205
(111)E	-118.435	-58.229
(011)A	-69.252	-9.046
(110)A	-108.175	-47.969
(110)B	-85.407	-25.202
(101)B	-104.122	-43.907

This quantity can be compared with the work of Kumar, *et al.* [150], for the 0.5ML (analogous to this work's (111)D surface) and 0.25ML (analogous to this work's (111)E surface). A direct comparison is not possible as the bulk structure of the nickel ferrite differs between studies but the relative stability of the 0.25ML to 0.5ML surfaces provide insight into the effect of the cation arrangement. In Kumar's study, the adsorption energy of a water molecule on the 0.5ML surface is 1.19eV more favorable than adsorption on the 0.25ML surface. This result conflicts with this study which find that adsorption of water on the 0.25ML surface is more favorable by 0.218eV. This difference is likely due to the differing arrangement of iron and nickel cations at the surface between these studies.

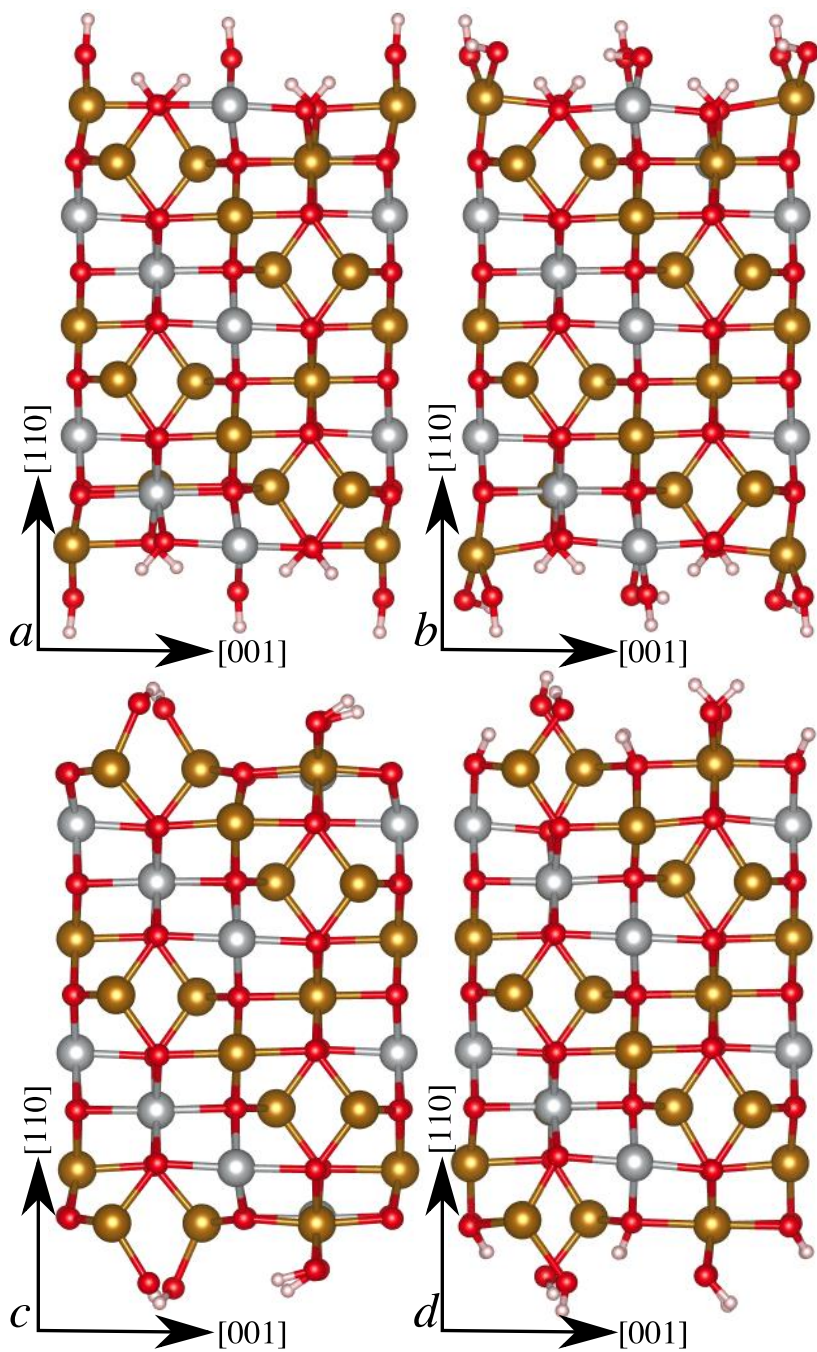


Figure 3.18 This figure shows all of the terminated (110) (a) A with one monolayer, (b) B with 4 H₂O and 2 excess O₂ molecules, and (c) B with one monolayer of water.

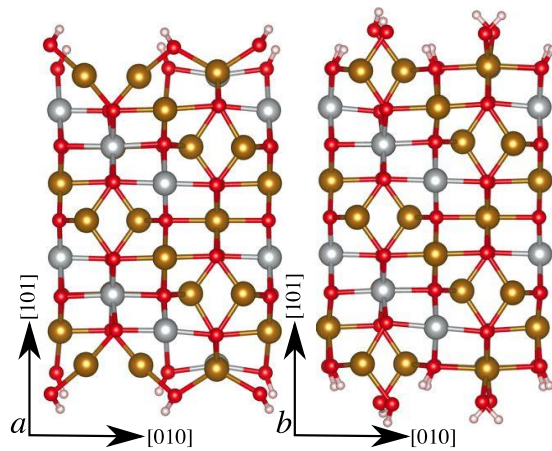


Figure 3.19 This figure shows all of the terminated (101) (a) B with 4 excess H₂, and (b) B with one monolayer.

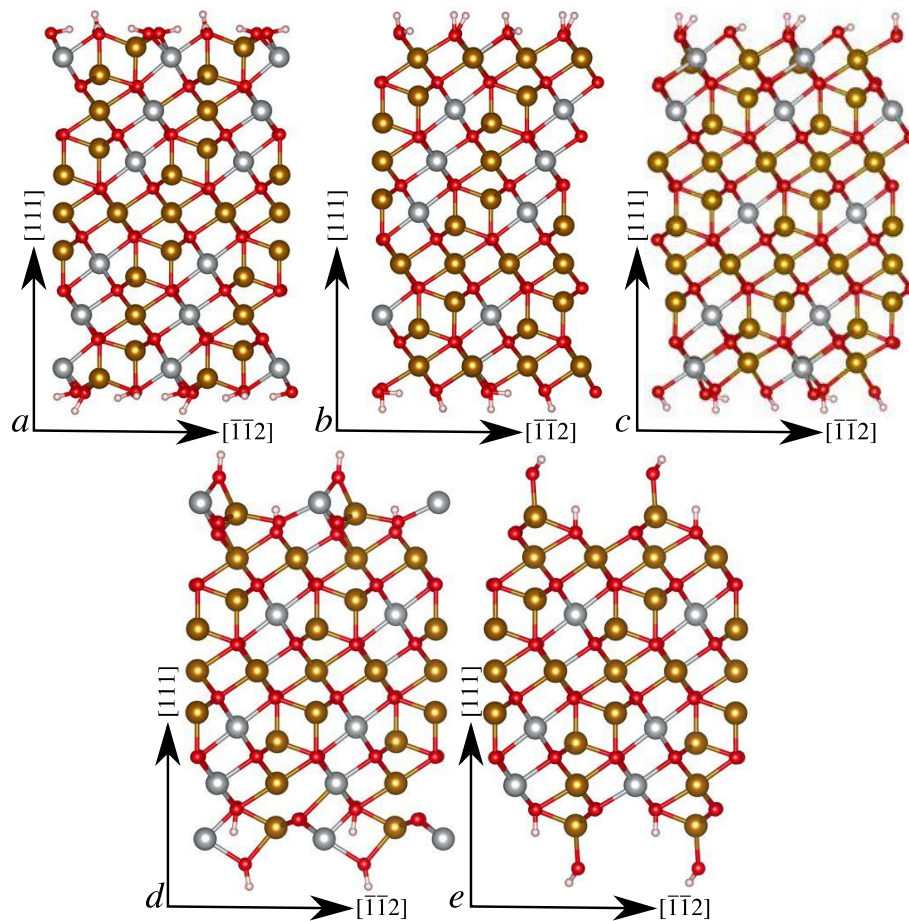


Figure 3.20 This figure shows all stable terminated (111) surfaces of NiFe₂O₄ where Fe (brown), or Ni (gray) layers are separated by layers of O (red) terminated with H (pink), as described in the text. Surface terminations are defined by Fig. 3.11e: (a) A, (b) A', (c) B, (d) D, (e) E.

3.5 Environment Dependent Surface Energies

Within this section, environment dependent surface energies are reported for nickel oxide and nickel ferrite at conditions representative of reactor conditions. There is a relatively large body of existing computational and experimental literature on the stability of NiO surface structures in vacuum and in humid air, and so it is useful to compare our results to the literature before discussing the implications of our results on CRUD formation in water.

3.5.1 Nickel Oxide

The calculated environment-dependent surface energies γ for the twelve low index surfaces of NiO are given in Table 3.16. The energy of the surface is first determined at 0K using a supercell calculation, $E_{\text{slab}}(0\text{K})$. The slab contains n_{NiO} formula units of bulk nickel oxide and $n_{\text{H}_2\text{O}}$ molecules of H₂O adsorbed onto the surface. The DFT+U energy and number of formula units is provided for each surface in Table 3.15. All of the nickel oxide surfaces calculated in Sec. 3.4.1 are stoichiometric meaning that $n_{\text{NiO}} = n_{\text{Ni}} = 2n_{\text{O}_2} - n_{\text{H}_2}$ and $n_{\text{H}_2} = n_{\text{H}_2\text{O}}$. This allows the expression for surface energy from Eq. (2.22) to be simplified and written in terms of the chemical potentials of only nickel oxide and water as

$$\gamma(T, P) = \frac{E_{\text{slab}}(0\text{K}) - n_{\text{NiO}}E_{\text{NiO}}(0\text{K}) - n_{\text{H}_2\text{O}}\mu_{\text{H}_2\text{O}}(T, P)}{2A}. \quad (3.6)$$

In the calculation of the surface energy, the free energy is approximated by the DFT+U calculated energy at 0K. This assumption means that, in Eq. (3.6), the chemical potential of water ($\mu_{\text{H}_2\text{O}}$) and the bulk energy at 0K are both ECPs. The temperature and pressure dependence of the surface energy is determined by the chemical potential of water alone. The surface area is multiplied by a factor of two due to the slab having two identical surfaces where the dimension of the surface cells are provided in Table 3.14.

Table 3.14 Data for calculations of NiO surface energies including k-point mesh densities, type (MP=Monkhorst-Pack, Γ =Gamma-centered), in-plane surface super-cell dimensions, and internal angle between super-cell vectors.

Surface Plane	Mesh Type	Mesh Density	$x(\text{\AA})$	$y(\text{\AA})$	$\alpha(^{\circ})$
(111) $p(1 \times 1)$	Γ	$7 \times 7 \times 1$	2.9658	2.9658	60
(111) $p(2 \times 2)$	Γ	$4 \times 4 \times 1$	5.9316	5.9316	60
(100)	MP	$5 \times 5 \times 1$	8.3885	8.3885	90
(110)	MP	$5 \times 4 \times 1$	5.9316	8.3885	90

Table 3.15 Critical data needed for evaluating various denuded nickel oxide surfaces including total DFT+U energy and the number of formula units of NiO and water. Note that the surface unit cell for the (111)OH-planar termination has $p(1 \times 1)$ symmetry, meaning that the unit cell has edges half the length of all other surface unit cells.

Surface Plane	Surface Termination	E(OK) [eV]	NiO	H ₂ O
(111)	O-octopole	-257.2132	26	0
	Ni-octopole	-216.3808	22	0
(111)	OH-planar (type 1)	-85.4371	7	1
	Diss. (type 2)	-225.1390	20	2
	H ₂ O (type 2)	-224.1597	20	2
	(type 3)	-224.8876	20	2
(100)	Denuded	-561.1530	56	0
	Assoc. H ₂ O (1.0ML)	-634.2212	40	16
	Assoc. H ₂ O (0.5ML)	-516.1816	40	8
	Assoc. H ₂ O (0.25ML)	-457.3144	40	4
	Diss. H ₂ O	-	-	-
(110)	Denuded	-272.2194	28	0
	Assoc. H ₂ O	Unstable	-	-
	Diss. H ₂ O	-392.8191	28	8

Table 3.16 Surface energies of all NiO surfaces studied in liquid water at 155bar. The surface energies are calculated with Eq. (3.6). Only those surfaces that are terminated have environment dependent surface energies.

Surface Plane	Surface Termination	γ (298.15K) (J/m ²)	γ (498.15 K) (J/m ²)	γ (598.15 K) (J/m ²)
(111)	O-octopole	1.799	1.799	1.799
	Ni-octopole	1.854	1.854	1.854
(111)	OH-planar	0.524	0.791	0.931
Diss.	(type 1)	2.016	2.149	2.220
H ₂ O	(type 2)	2.273	2.407	2.477
	(type 3)	2.082	2.215	2.286
(100)	Denuded	0.863	0.863	0.863
	Assoc. H ₂ O (1.0ML)	1.083	1.544	1.788
	Assoc. H ₂ O (0.5ML)	1.003	1.233	1.355
	Assoc. H ₂ O (0.25ML)	0.945	1.060	1.121
	Diss. H ₂ O	2.555	3.016	3.260
(110)	Denuded	1.956	1.956	1.956
	Assoc. H ₂ O	unstable	—	—
	Diss. H ₂ O	1.657	1.984	2.156

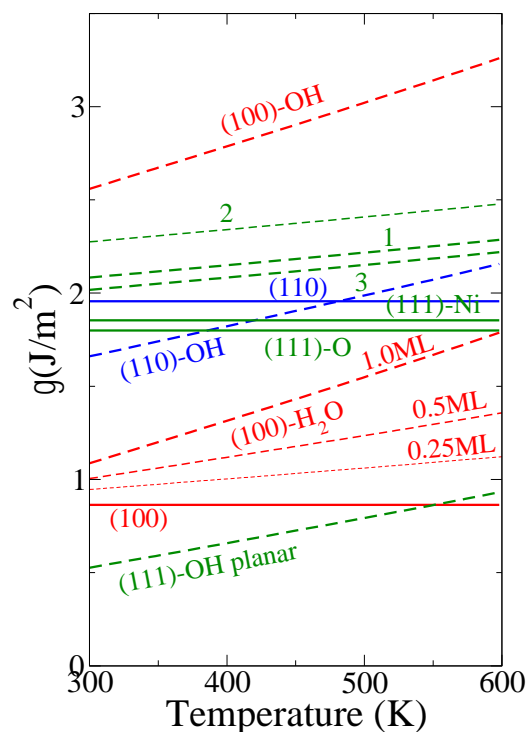


Figure 3.21 The environment dependent surface energies for the investigated surfaces of NiO in liquid water at 155bar. Terminated surfaces are plotted as dashed lines, and denuded surfaces are plotted as solid lines. The (111) surfaces are plotted in green, (110) in blue, and (100) in red. The numbered labels correspond to the three variants of the (111)-OH surfaces illustrated in Fig. 3.10(d-f).

Given in Table 3.17 is a comparison between the surface energies calculated here and reported literature values at 0K. The surface energy at 0K is calculated using Eq. (3.6) by replacing $\mu_{\text{H}_2\text{O}}$ with $E_{\text{H}_2\text{O}}(0\text{K}) = -1371.9296 \text{ kJ/mol}$, which is the DFT calculated energy of a water molecule. Although the literature calculations used a wide variety of computational methods, and therefore quantitative agreement is not expected, comparison to surface energy trends is meaningful. The overall lowest energy structure at 0K of those studied is the (111)OH-planar structure, which is consistent with the prior all-electron B3LYP calculations by Wander *et al.* [151] and the DFT calculations by Ciston *et al.* [124]. For the latter, the values in the parenthesis used a PBE0 functional, while the other values given used a TPSS meta-GGA functional.

Table 3.17 Energies of various NiO surfaces with multiple terminations in vacuum at 0K. ^aTPSSh and (PBE0) functionals with 12.5% exact exchange [124]; ^bSimulation [130]; ^cGGA+U ($U_{\text{eff}}=6.3\text{eV}$) [85]; ^dHybrid-Meta-GGA B3LYP exchange-correlation functional [151]; ^eEstimated from reported binding energies [85].

Surface Plane	Surface termination	γ calculated in this work (J/m ²)	γ Reference (J/m ²)
(111)	O-octopole	1.799	2.153 (2.153) ^a
	Ni-octopole	1.854	2.257 (2.257) ^a
	Octopole (Ni-O ave.)	1.827	3.52 ^b 2.33 ^d
(111) Diss. H ₂ O	OH-planar	-0.132	0.000 (0.207) ^a 0.495 ^d
	type 1	1.688	2.153 (2.070) ^a
	type 2	1.945	2.381 (2.257) ^a
	type 3	1.754	2.526 (2.319) ^a
(100)	Denuded	0.864	1.54 ^d 2.67 ^c
	Assoc. H ₂ O (1.0ML)	-0.054	0.0323 ^e
	Assoc. H ₂ O (0.5ML)	0.434	0.395 ^e
	Assoc. H ₂ O (0.25ML)	0.661	0.573 ^e
	Diss. H ₂ O	1.418	
(110)	Denuded	1.956	
	Diss. H ₂ O	0.853	

The next lowest energy structures examined consist of water chemisorbed onto the (100) surface at three different surface coverages. While there have not been prior reports of surface energies, Yu *et al.* [85] have reported adsorption energies per water molecule of -61.9 , -49.8 and -44.1 kJ/mole for coverages of 0.25, 0.5 and 1 monolayer, respectively, from GGA+U DFT calculations, and Schulze and Reissner [152] have reported an experimental value of -52 kJ/mole based on analysis of thermally programmed desorption (TPD) data. The literature energies for these surfaces listed in the table are estimated from the Yu *et al.* data; these agree well with our results. This bonding configuration in both our calculations and in calculations by Yu *et al.* consists of the oxygen atoms in the overlayer sitting almost on top of the surface nickel atoms at an inter-atomic distance of about 2.4\AA , with the chemisorbed molecules almost flat against the surface with a distance of about 2.3\AA between the hydrogen atoms and oxygen atoms in the NiO surface.

The next lowest energy structures from our calculations are the (110) with chemisorbed hydroxyl groups and the denuded (100) surface, the OH terminated (100) surface, and the various (111) surfaces (except for the OH-planar structure). This ordering agrees with the prior calculations of Ciston *et al.* and by Wander *et al.*

The experimental TPD data of Schulze and Reissner [152] can be used to further validate the calculated relative surface energies for the three water terminated and the denuded (100) surfaces. The TPD experiments, which were carried out at water vapor overpressure of 10^{-9} – 4×10^{-6} mbar, indicate the onset of water desorption at about 200K that is completed by 300K. Plotted in Fig. 3.22 are calculated free energies of the (100) surfaces as a function of temperature T using a chemical potential for water vapor of $\mu(T) = \mu_{\text{H}_2\text{O}}^0(T) + RT \ln p$, where R is the gas constant and p is a water overpressure of 10^{-10} bar. The slopes of the lines with respect to temperature are different due to the different water coverage. The preferred surface stability changes with increasing temperature from a full monolayer to the denuded surface, which for this pressure occurs at ~ 260 K. At the lower reported experimental pressure this calculated crossing occurs at 220K, while at the highest reported pressure the calculated crossing occurs at 300K. These bounds are consistent with the range of reported temperatures for water desorption.

Loss of a terminating layer with increasing temperature at low water vapor pressures is expected and predicted by these calculations. In contrast, for NiO and NiFe₂O₄ surfaces in liquid water at high temperatures it is not intuitively clear that termination will be lost prior to water boiling. As discussed previously, this issue of surface termination is especially important for understanding CRUD deposition in PWRs because the type of surface termination will likely have a profound influence on the deposition kinetics.

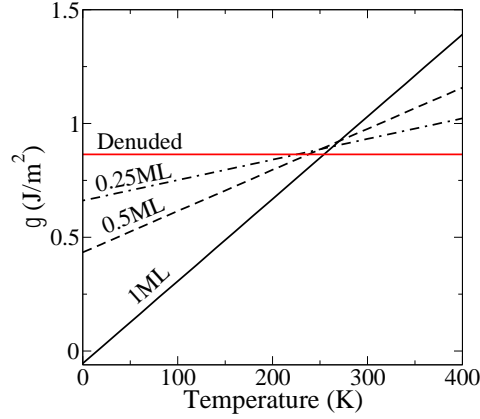


Figure 3.22 Plot of surface energy versus temperature for NiO (100) surfaces at 10^{-10} bar.

3.5.2 Nickel Ferrite

In discussing the surfaces investigated herein, it was noted that the (011), (110), and (101) surfaces would be equivalent if the nickel cations were randomly distributed on the octahedral sites. A direct comparison between these surfaces, using the total slab energies is not possible due to the varying stoichiometry. However, a comparison between surface energies for equivalent terminations can provide a useful estimate of the effect of randomly distributing the nickel cations. The surface energies of A-type (011), (110), and (101) surfaces (illustrated in Figs. 3.13a, 3.14a, and 3.15a) must be compared separately from the B-type (011), (110), and (101) surfaces (illustrated in Figs. 3.13b, 3.14b, and 3.15b). Surface energies for denuded and terminated surfaces are calculated using Eq. (2.48) where the free energy of the bulk is approximated by the DFT+U calculated energy at 0K:

$$\gamma(T, P) = \frac{1}{2A} \left\{ E_{\text{slab}} - \Gamma_{\text{Fe}} \mu_{\text{Fe}^{+2}} - \Gamma_{\text{Ni}} \mu_{\text{Ni}^{+2}} - \Gamma_{\text{NiFe}_2\text{O}_4} E_{\text{NiFe}_2\text{O}_4} - n_{\text{H}_2} \mu_{\text{H}_2\text{O}} - [\Gamma_{\text{Fe}} + \Gamma_{\text{Ni}}] \cdot \left((\Delta_f G_{\text{H}_2})_{\text{aq}} - (\mu_{\text{H}_2})_{\text{aq}} + 2\mu_{\text{H}^+} \right) \right\}. \quad (3.7)$$

The values of Γ are calculated using Eqns. (2.30)–(2.32) where the number of formula units and the 0K slab energies are provided for each denuded and terminated surface in Tables 3.18 and 3.20, respectively. The dimensions of the surface cells are

provided in Table 3.19. The surface energies are evaluated for denuded and terminated surfaces and provided at three temperatures in Tables 3.21 and 3.22, respectively. The mean and standard deviation are provided for the {110} surfaces with a full monolayer to approximate the effect of a random distribution of cations. The composition of partial monolayers includes varying amounts of H₂ and H₂O, so the results cannot be directly compared. The limits on the allowed chemical potentials provided by Eqs. (2.49)–(2.51) are satisfied by the concentrations of metal ions present in the coolant of a PWR at pH = 7.2 ± 0.2. Representative concentrations of ions are provided by Henshaw, *et al.* [12], where [Fe⁺²]_{aq} = 4.17 × 10⁻¹³, [Ni⁺²]_{aq} = 1.66 × 10⁻¹⁴, and [H₂]_{aq} = 1.10 × 10⁻³.

Table 3.18 Critical data needed for evaluating various denuded nickel ferrite surfaces including total DFT+U energy and the number and type of atomic species. Stoichiometric surfaces are also provided and identified as the S surface cut.

Plane	Surface Cut (Fig. 3.11)	E (0K) [eV]	Ni	Fe	O ₂	H ₂
(111)	A	-320.7655	7	14	16	0
	A'	-321.7017	7	14	16	0
	S	-304.7516	7	14	14	0
	B	-273.9620	7	14	12	0
	C	-274.0147	7	14	12	0
	D	-264.7172	7	12	12	0
	E	-256.3921	5	12	12	0
(100)	A	-416.9191	10	18	20	0
	B	-449.3741	10	22	20	0
	S	-433.7861	10	20	20	0
(110)	A	-398.5005	9	17	18	0
	B	-381.7649	9	19	18	0
(011)	A	-377.4462	10	16	18	0
	B	-401.5694	8	20	18	0
	S	-336.6625	8	16	16	0
(101)	A	-381.6632	9	17	18	0
	B	-398.7525	9	19	18	0
	D	-398.3561	9	19	18	0

Table 3.19 Data for calculations of nickel ferrite surface energies including k-point mesh densities, type (MP=Monkhorst-Pack, Γ =Gamma-centered), in-plane surface super-cell dimensions, and internal angle between super-cell vectors.

Surface Plane	Mesh Type	Mesh Density	$x(\text{\AA})$	$y(\text{\AA})$	$\alpha(^{\circ})$
(111)	Γ	$7 \times 7 \times 1$	5.9443	5.9443	60
(100)	MP	$5 \times 5 \times 1$	8.4065	8.4065	90
{110}	MP	$5 \times 7 \times 1$	8.4065	5.9443	90

Table 3.20 Critical data needed for evaluating various terminated nickel ferrite surfaces including total DFT+U energy and the number and type of atomic species.

Plane	Surface Cut (Fig. 3.11)	E(OK) [eV]	Ni	Fe	O ₂	H ₂
(111)-OH	A	-368.6230	7	14	16	4
	A'	-368.0263	7	14	16	4
	B	-346.4456	7	14	15	3
	D	-295.1741	7	12	13	2
	E	-287.2847	5	12	13	2
(110)-OH	A-Partial	-464.2438	9	17	20	6
	A-1ML	-502.5975	9	17	22	8
	B-Partial	-398.5005	9	19	18	0
	B-1ML	-521.2203	9	19	22	8
(011)-OH	A-Partial	-460.3859	10	16	20	6
	A-1ML	-496.9388	10	16	22	8
(101)-OH	B-Partial	-428.9061	9	19	18	4
	B-1ML	-521.1355	9	19	22	8

The stoichiometric surface energies are independent of the concentration of metal ion precursors and the denuded stoichiometric surface energies are independent of temperature. These surfaces are reported as having a S surface cut in Table 3.21. The temperature independence reflects the fact that the surface is composed of only bulk nickel ferrite. The origin of the temperature dependence in terminated stoichiometric surfaces ((111) surfaces of type A and A' reported in Table 3.22) is due to the temperature dependent chemical potential of the adsorbed water.

Many of the nickel ferrite surfaces considered herein are predicted to have a negative surface energy in the coolant of a PWR; the lowest of which are plotted in Fig. 3.23. This work predicts that the denuded, metal terminated, (111)B and C surfaces will be the most stable. Negative surface energies arise because the energy calculated is

actually a quasi-surface energy as discussed in Ch. 2. Negative surface energies have been found previously and arise from chemical effects [153,154]; In a multicomponent system, this is due to having to choose the component(s) that become the surface excess quantities. This study has chosen to express surface excess quantities in terms of water and metal cations. The presence of a full monolayer of water on the surface decreases the energy of the surface in each case examined. The effects of partial termination were the same except in the case of (110)B, where the partial termination, which included excess oxygen atoms, increased the surface energy. This is consistent with the behavior that all of the slabs with metal deficiencies had positive surface energies, with the exception of the (011)A surface with a partial termination of four H₂O and two H₂ molecules.

Table 3.21 Surface energies of denuded nickel ferrite surfaces at conditions representative of PWR coolant. The average and standard deviation of the equivalent {110} surfaces are provided separately from the stoichiometric (011) surface.

Plane	Surface Cut (Fig. 3.11)	γ (J/m ²)		
		298.15K	498.15K	598.15K
(111)	A	15.221	15.079	15.032
	A'	14.976	14.834	14.787
	S	1.708	1.708	1.708
	B	-7.937	-7.796	-7.749
	C	-7.951	-7.810	-7.763
	D	-2.014	-1.962	-1.943
	E	5.288	5.235	5.217
(100)	A	4.663	4.625	4.613
	B	-2.030	-1.979	-1.998
	S	1.235	1.235	1.235
{110}	A	4.100±0.109	4.075±0.202	4.067±0.204
	B	-0.796±0.026	-0.770±0.138	-0.762±0.138
(011)	S	3.059	3.059	3.059

Table 3.22 Surface energies of terminated nickel ferrite surfaces at conditions representative of PWR coolant. The average and standard deviation of the equivalent $\{110\}$ -1ML surfaces are provided separately from those of the partially terminated surfaces which are provided for each plane separately.

Plane	Surface Cut (Fig. 3.11)	γ (J/m ²)		
		298.15K	498.15K	598.15K
(111)	A	0.530	0.795	0.935
	A'	0.686	0.951	1.091
	B	-1.977	-1.742	-1.626
	D	-2.216	-2.031	-1.943
	E	4.972	5.052	5.104
{110}	A-1ML	3.900±0.291	4.201±0.294	4.364±0.296
	B-1ML	-1.429±0.010	-1.077±0.010	-0.897±0.010
(011)	A-Partial	-0.215	0.051	0.187
(101)	B-Partial	-6.997	-6.721	-6.598
	B-1ML	-1.422	-1.070	-0.890
(110)	A-Partial	-0.337	-0.077	0.057
	B-Partial	6.269	6.372	6.438

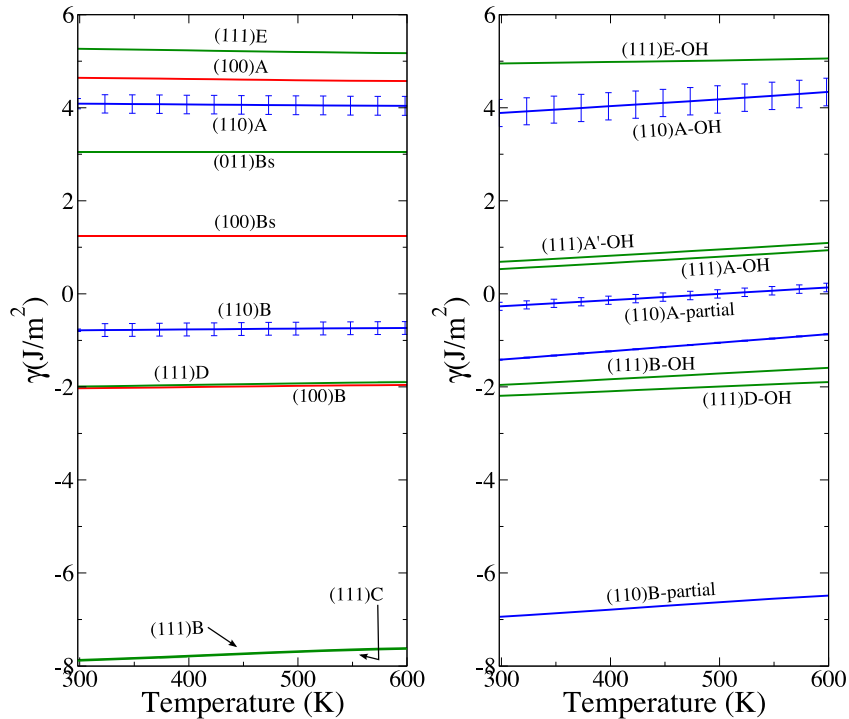


Figure 3.23 The $\{110\}$ (blue), (111) (green), and (100) (red) surfaces of nickel ferrite are shown as a function of temperature in the presence of ions at concentrations typical of PWR coolant. Denuded surfaces are shown in the plot at left, and terminated surfaces are shown on the other plot. The energies of the denuded (111)A and (111)A' surfaces are not shown.

4 Understanding CRUD Deposition

The primary purpose of this dissertation is to develop an understanding of the mechanisms of CRUD deposition beyond what is inferred from continuum thermal-hydraulic and thermodynamic models. Existing continuum models of CRUD formation are lacking a detailed understanding of the origin of particulates observed in CRUD, their stability and mechanism of agglomeration. What is likely the principle reason for the neglect of nano-sized particulates in these models is that data supplied by plants report corrosion products that pass through their filters (diameter $\leq 0.1\mu\text{m}$) as soluble species assumed to be ions or hydroxides. However, nano-sized particles passing through the filter may play an important role in determining the structure and morphology of the CRUD deposits as these particulates could serve as nuclei for the growth of larger particles or adhere to CRUD surfaces directly. Due to the large surface to volume ratio of nanoparticles, the energy of the surface could have a large impact on particle stability and barrier to nucleation. Mechanisms of boron incorporation into CRUD will be considered within the DFT-referenced semi-empirical thermodynamics framework. This technique will enable consideration of boron incorporation into materials, such as Bonaccordite, that are not available in existing thermodynamic databases.

4.1 Origin of Particles in Reactor Coolant and CRUD

The first goal of this section is to develop an understanding of the origin of the observed nano-sized particles by determining if the particles could nucleate at conditions predicted, by continuum models, for the coolant or within the porous structure of the CRUD. In this dissertation, only nickel oxide and nickel ferrite particles will be considered. Beyond the consideration of homogeneous nucleation, the DFT-referenced semi-empirical thermodynamic approach will be employed to predict whether particle growth might occur under conditions dissimilar from those that permit nucleation. The second goal of this section is to propose a mechanism for agglomeration of particles that is consistent with the chemical environment predicted at the sites of observed

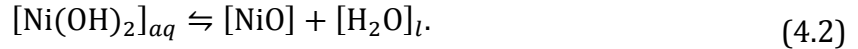
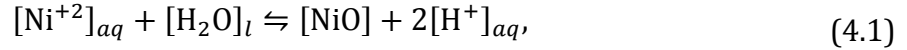
CRUD deposition. The agglomeration of particles is not the only, or even the principle, mechanism of CRUD deposition; Most growth is likely due to the supersaturation of metal precursors [12,13,23,155]. However, the outer layer (coolant-side) of CRUD is principally made of loosely-adherent particulate material where it has been suggested to result from the deposition of particles existing in the coolant [156,157]. This work proposes that the agglomeration of particles can contribute to its formation. It is generally accepted that these particles do not form via homogeneous nucleation in the coolant. However, existing calculations rely on simplified estimate surface energy and assume spherical particles (e.g. Ref. [4]). The improved estimates of surface energy and particle shape derived in this dissertation provide a more refined understanding of the nucleation behavior of these particles.

Table 4.1 Concentrations of species and conditions representative of various environments in operating PWRs are drawn Ref. [11] and reported in molal units at 473K. The conditions representing thick CRUD are obtained from Refs. [11,12]. These conditions are predicted to exist at a depth of 40 μ m from the coolant-side CRUD with a total thickness of 60 μ m.

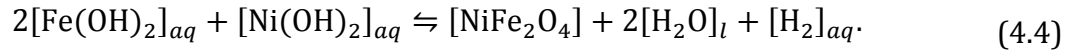
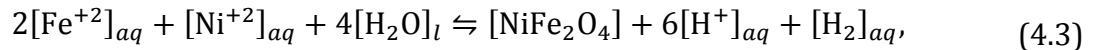
Species concentrations	Coolant	Thick CRUD
Temperature	548K-598K	≤ 643 K
pH	7.2 ± 0.2	7.8
$[\text{Fe}^{+2}]_{aq}$	4.17×10^{-13}	
$[\text{Fe}(\text{OH})_2]_{aq}$	7.90×10^{-9}	
$[\text{Ni}^{+2}]_{aq}$	1.66×10^{-14}	
$[\text{Ni}(\text{OH})_2]_{aq}$	3.01×10^{-10}	
$[\text{H}_2]_{aq}$	1.10×10^{-3}	7.44×10^{-5}
$[\text{B}(\text{OH})_3]_{aq}$	2.91×10^{-2}	2.20
$[\text{Li}^+]_{aq}$	1.67×10^{-7}	1.00×10^{-2}

The MAMBA (MPO Advanced Model for Boron Analysis) continuum code is used to provide estimates of the temperature, pH, along with concentrations of metal ions, aqueous hydroxides, and aqueous hydrogen within CRUD [3,155,156]. Representative results for thin and thick CRUD are reported in Table 4.1. Coolant pressure is assumed to be a constant 155bar.

There are many possible reactions that could result in the homogeneous nucleation of nickel oxide and nickel ferrite particles in the coolant. Herein, it is assumed that the most prevalent species ($[M^{+2}]_{aq}$ and $[M(OH)_2]_{aq}$) serve as the source of metal for the particles. This work considers two possible mechanisms by which nickel oxide may be formed in the coolant:



Nickel ferrite is also assumed to form according to:



The free energies of the reactions given by Eqs. (4.1)–(4.4), at concentrations representative of coolant and deep into CRUD (Table 4.1) are plotted in Fig. 4.1. Investigating the formation of nickel oxide and nickel ferrite from thermodynamics alone indicates that the formation of the bulk from hydroxides is favorable, but the bulk will not be stable due to dissolution into ions in the coolant under standard conditions; Substantial concentration enhancement, increased pH, or high temperatures are required for the bulk phase to be stable. All three of these factors are present for the coolant as it is drawn into the porous structure of CRUD. The effect of these changes in the species concentrations (100-fold), temperature, and pH are indicated by comparing the marked and unmarked lines in Fig. 4.1. This leads us to the conclusion that the presence of CRUD could make the formation of metal oxides thermodynamically favorable. However, even in the absence of concentration enhancement, a rise in pH can affect a substantial change on the thermodynamics as indicated by the increased favorability of metal oxide formation upon a change from 7.2 (unmarked lines) to 7.8 (marked lines) in Fig. 4.2.

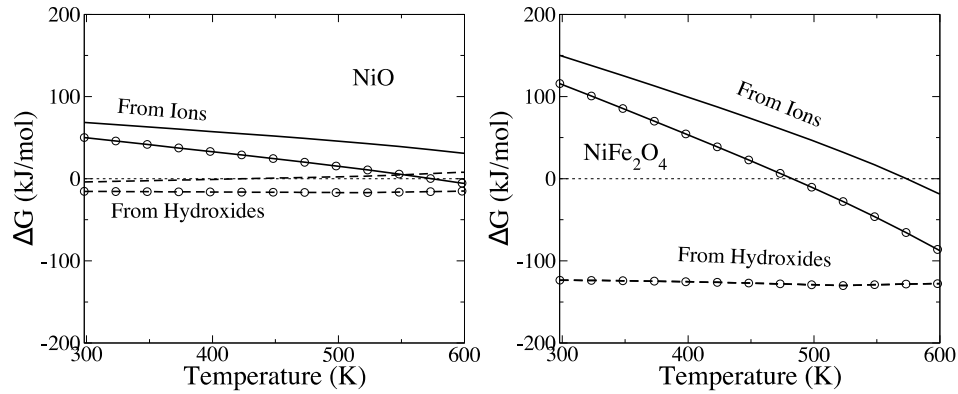


Figure 4.1 The free energy reaction for forming nickel oxide (left) from ions (Eq. (4.1)) and hydroxides (Eq. (4.2)) are plotted as solid and dashed lines, respectively. The free energy of reaction for forming nickel ferrite (right) from ions (Eq. (4.3)) and hydroxides (Eq. (4.4)) are plotted as solid and dashed lines, respectively. Lines marked with circles represent the reactions with concentrations increased a hundred-fold with $\text{pH} = 7.8$, approximating the conditions deep within CRUD.

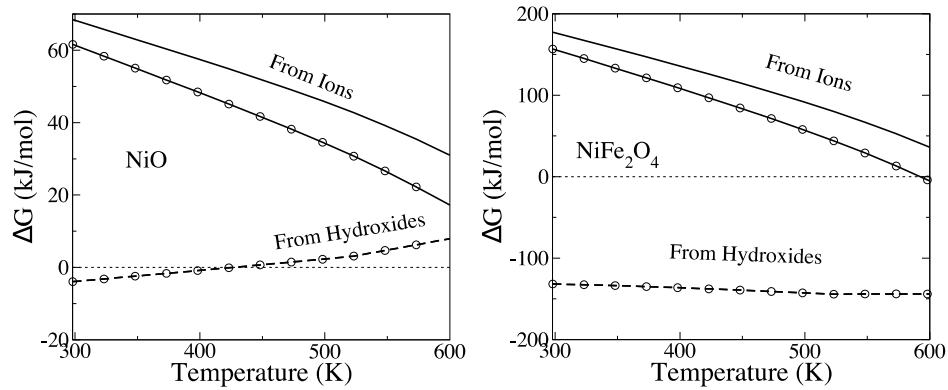


Figure 4.2 The free energy reaction for forming nickel oxide (left) from ions (Eq. (4.1)) and hydroxides (Eq. (4.2)) are plotted as solid and dashed lines, respectively. The free energy of reaction for forming nickel ferrite (right) from ions (Eq. (4.3)) and hydroxides (Eq. (4.4)) are plotted as solid and dashed lines, respectively. Unmarked lines indicate reactions occurring at $\text{pH} = 7.2$, while lines marked with circles are for $\text{pH} = 7.8$, both with concentrations unchanged from the bulk coolant.

4.1.1 Morphology of NiO and NiFe₂O₄ Crystallites

Equilibrium crystal shapes were calculated according to the Wulff Construction using the WULFFMAKER software [158]. For nickel oxide, the Wulff construction predicts that only two surfaces are present at the conditions of interest: the hydroxyl terminated

(111) and denuded (100) surface. The temperature dependence of these surfaces is plotted in Fig. 4.3a. For nickel ferrite, only the denuded (111)C surface will be exposed, with surface energy plotted in Fig. 4.3b. The NiO surfaces are independent of pH while the NFO surface is only weakly dependent on pH.

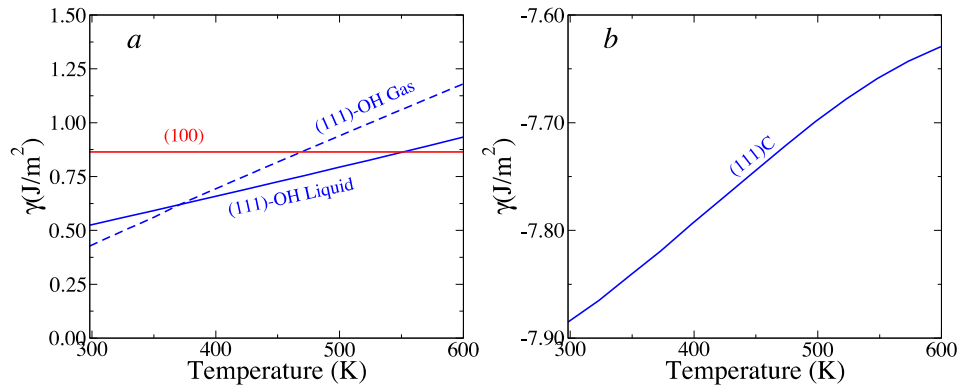


Figure 4.3 The lowest energy surfaces of (a) NiO and (b) NiFe₂O₄ are plotted. The (111) surface terminated with hydroxyl groups is the only surface which is dependent on the phase of the water.

The Wulff construction predicts that the equilibrium crystal shape of nickel oxide is octahedral with (111) surfaces terminated by hydroxyl groups at low temperatures, transitioning to a truncated-octahedron shape at temperatures of approximately 298K in water at 155bar or 348K in steam at 155bar (illustrated in Table 4.2). Due to the exceptional stability of the (111)C surface of nickel ferrite, the equilibrium crystal shape (illustrated in Table 4.3) will be octahedral at all conditions relevant to PWR operation.

Table 4.2 Scaled illustration of the Wulff construction for the equilibrium shapes of NiO crystallites in liquid and steam. The hydroxyl terminated (111) surface is grey and the denuded (100) surface is red.

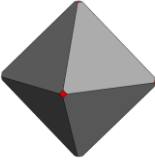
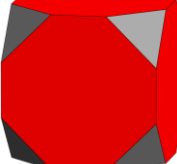
Temperature (K)	298.15	398.15	498.15	598.15
Liquid (155 bar)				
Steam (155 bar)				

Table 4.3 Scaled illustration of the Wulff construction for the equilibrium shapes of NiFe₂O₄ particles in liquid and steam. The denuded (111)_C surface is brown.

Temperature (K)	298.15–598.15
Liquid & Solid (155 bar)	

4.1.2 Homogeneous Nucleation

With detailed knowledge of the equilibrium crystal shape, surface energy, and aqueous thermodynamics provided by this dissertation, the barrier to homogeneous nucleation of particles comprising CRUD can be more accurately calculated. In Sec. 4.1.1, the Wulff construction revealed that there are two types of shapes that the particles may form: regular and truncated octahedra. With this knowledge, the free energy of a particle can be expressed as a sum of the bulk and surface energies:

$$G_{\text{particle}}(T, P) = V\rho_{\text{bulk}}E_{\text{bulk}}(\text{OK}) + (\gamma_{100}(T, P)A_{100}(T, P) + \gamma_{111}(T, P)A_{111}(T, P)). \quad (4.5)$$

The free energy of bulk NiO and NFO (NiFe_2O_4) are calculated from the bulk chemical potential (defined as the DFT energy at 0K, i.e. $E_{\text{bulk}}(0\text{K})$) multiplied by a given volume (in \AA^3) and a molar density of ρ_{bulk} . The constant ρ_{bulk} corresponds to either $\rho_{\text{NiO}} = 8.99047 \times 10^{-26} \text{ mol}_{\text{NiO}}/\text{\AA}^3$, or $\rho_{\text{NFO}} = 22.3610 \times 10^{-27} \text{ mol}_{\text{NFO}}/\text{\AA}^3$, which is the number of moles of bulk crystal per unit volume. The surface area occupied by (111) and (100) surfaces are denoted as A_{111} and A_{100} , respectively. The surface area and volume are defined in terms of the characteristic dimensions illustrated in Fig. 4.4. Regular octahedral particles are characterized by the width of the particle along the edge of the square base (a). The particle is bound by eight (111) planes for a total surface area $A_{111} = 2\sqrt{3}a^2$ and volume $V = \frac{1}{3}\sqrt{2}a^3$. Truncated octahedral particles are characterized by two dimensions: the length of an edge of the square octahedron base (b), and length of the square end-cap base (c). The volume is expressed as $V = \sqrt{2}\left(\frac{b^3}{3} - c^3\right)$. The total surface area of the (100) faces is $A_{100} = 6c^2$, and that of the (111) faces is $A_{111} = 2\sqrt{3}(b^2 - 3c^2)$.

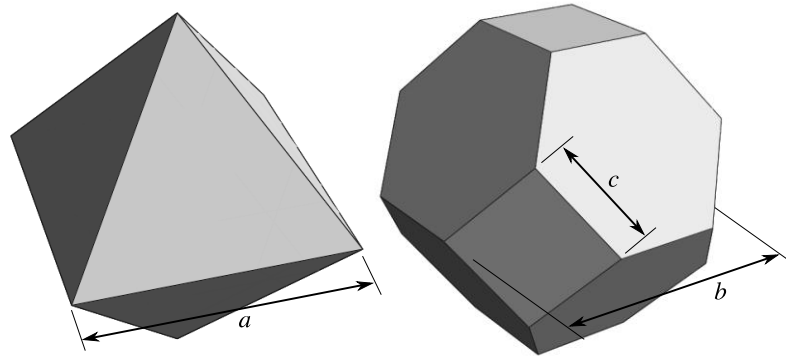


Figure 4.4 Illustration of the definition of the characteristic width, a , of a regular octahedron, and those of a truncated octahedron, b and c .

This study considers the possibility that NiO particles are nucleated from divalent ions according to the reaction:

$$\begin{aligned}
& V\rho_{\text{NiO}}[\text{Ni}^{+2}]_{aq} + (V\rho_{\text{NiO}} + \rho_{100}A_{100} + \rho_{111}A_{111})[\text{H}_2\text{O}]_l \\
& \quad \rightleftharpoons \{V\rho_{\text{NiO}}[\text{NiO}] + (\rho_{100}A_{100} + \rho_{111}A_{111})[\text{H}_2\text{O}]\}_{\text{particle}} \\
& \quad + 2V\rho_{\text{NiO}}[\text{H}^+]_{aq}.
\end{aligned} \tag{4.6}$$

The bracketed quantity with the ‘particle’ sub-script represents the number of formula units which comprise the particle. The constant ρ_{111} and ρ_{100} are defined as the molar density of H_2O on (111) or (100) surfaces where $\rho_{111} = 2.17992 \times 10^{-25} \text{ mol}_{\text{H}_2\text{O}}/\text{\AA}^2$ and $\rho_{100} = 0 \text{ mol}_{\text{H}_2\text{O}}/\text{\AA}^2$. The free energy of the reaction given by Eq. (4.6) is:

$$\begin{aligned}
\Delta G(T, P) = & G_{\text{particle}}(T, P) + 2V\rho_{\text{NiO}}(\mu_{\text{H}^+}(T, P))_{aq} - V\rho_{\text{NiO}}(\mu_{\text{Ni}^{+2}}(T, P))_{aq} \\
& - [V\rho_{\text{NiO}} + \rho_{100}(T, P)A_{100}(T, P) \\
& + \rho_{111}(T, P)A_{111}(T, P)](\mu_{\text{H}_2\text{O}}(T, P))_l.
\end{aligned} \tag{4.7}$$

$G_{\text{particle}}(T, P)$ is the free energy of the particle calculated using Eq. (4.5), which includes the contributions from the bulk and surface energies. Fig. 4.5 contains plots of the free energy for the homogeneous nucleation of NiO particles at PWR operating conditions.

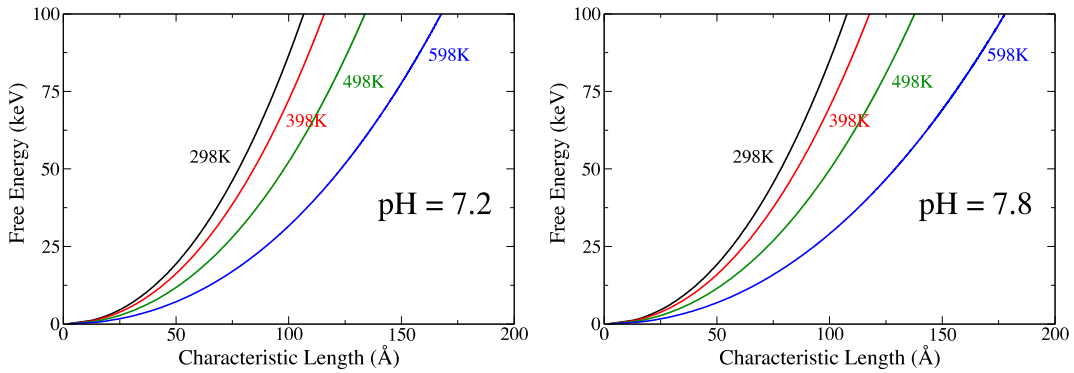
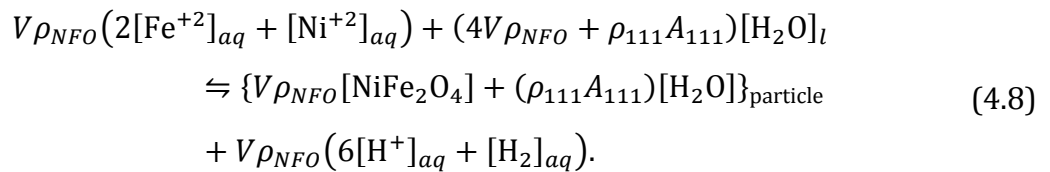


Figure 4.5 The free energy of the reaction, defined by Eq. (4.7), for forming a NiO particle (with characteristic length b) is plotted. The reaction is plotted for a pH of 7.2 (left) and 7.8 (right) with divalent cations at coolant concentrations.

This analysis provides no evidence for the homogeneous nucleation of NiO particles at temperatures and reactant concentrations existing in the coolant, or those

predicted to exist within deep CRUD. This result is expected from the data plotted in Fig. 4.2, which indicates that the formation of bulk NiO is not favorable at coolant concentrations. Although Fig. 4.1 does indicate that a 100-fold increase in concentration will make bulk NiO stable, the concentration does not decrease the nucleation barrier height to make homogeneous nucleation a significant source of particles (results are not plotted). The morphology of nickel oxide particles making up CRUD can be qualitatively compared to actual samples which are found in the form of needles and cubes [7]. This model does not predict the formation of acicular nickel oxide particles. Observations by Yeon, *et al.* [20], have demonstrated that the formation of nickel oxide is the kinetically favored product of the reaction between aqueous nickel ions and preexisting Magnetite films or particles. Kinetics is likely to be the reason for the formation acicular nickel oxide particles. In CRUD from plants which underwent CIPS, at least some of the NiO deposits were observed to be roughly spherical particles approximately 0.1 μm in diameter [14]. According to this work, truncated octahedrons approaching the appearance of a cube would be expected if NiO particles were to be formed in steam or liquid water at very high temperatures (in excess of 598K). However, extremely concentrated solutions would be required to generate these particles from homogeneous nucleation. The present model of ion activity is only applicable to dilute solutions, and would be invalid in this regime. From this work, it is concluded that homogeneous nucleation of NiO particles are not the source of the observed deposits in CRUD and a more likely explanation is the heterogeneous growth of nickel oxide crystallites.

This study also considers the case of NFO particle formation from doubly charged aqueous cations:



The constant ρ_{111} is defined as the number of moles of H_2O on (111) surface where $\rho_{111} = 108.5293 \times 10^{-27} \text{ mol}_{\text{H}_2\text{O}}/\text{\AA}^2$. The free energy of formation of a NFO particle,

$$\begin{aligned}
\Delta G(T, P) = & G_{\text{particle}}(T, P) + V\rho_{\text{NFO}} \left(6(\mu_{\text{H}^+}(T, P))_{\text{aq}} + (\mu_{\text{H}_2}(T, P))_{\text{aq}} \right) \\
& - V\rho_{\text{NFO}} \left(2(\mu_{\text{Fe}^{+2}}(T, P))_{\text{aq}} + (\mu_{\text{Ni}^{+2}}(T, P))_{\text{aq}} \right) \\
& - (4V\rho_{\text{NFO}} + \rho_{111}A_{111}) (\mu_{\text{H}_2\text{O}}(T, P))_l,
\end{aligned} \tag{4.9}$$

in PWR coolant at operating conditions is plotted in Fig. 4.6(*left*). Notice that, because bulk NFO is unstable at coolant conditions used in calculating the free energy, the curves imply not a nucleation barrier, but a stable particle size. Although the surface energy is weakly dependent on pH, the reaction for forming the particles is highly pH dependent; The result of increasing pH is a large increase in the stable particle size and greatly increased stability Fig. 4.6(*right*). With an increase in pH to 7.8, bulk NFO becomes stable at high temperatures (Fig. 4.1(*right*)) allowing for the deposition of bulk NFO. With an increase in precursor concentration predicted to occur within CRUD, the most stable particle would be larger, approaching the micron-sized particles observed in CRUD samples. Even without an increase in the concentration of metal ions, the energetic stability and particle size is further increased at conditions representative of CRUD (Table 4.1) as illustrated by comparing Figs. 4.6(*right*) to 4.7. The stability of NFO particles in coolant is a novel prediction that may greatly improve our understanding of the mechanism by which CRUD forms.

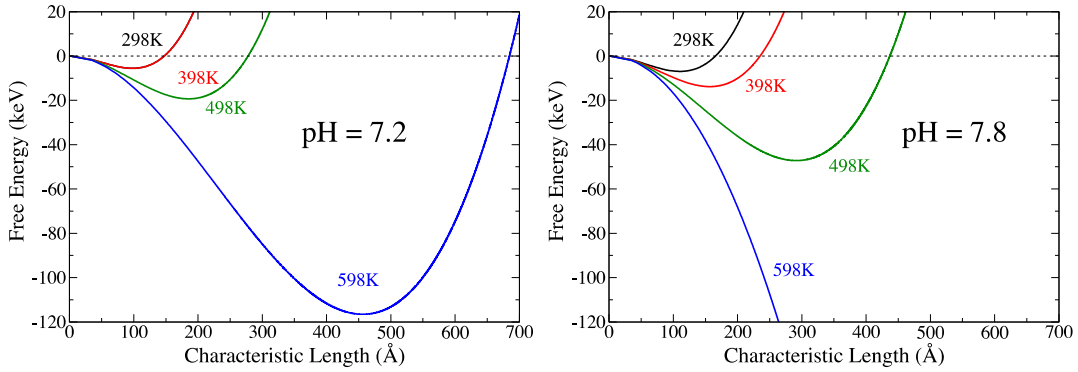


Figure 4.6 Plot of the free energy of the reaction, given by Eq. (4.8), forming an octahedral NFO particle (with characteristic length a) from divalent cations at a pH of 7.2 (left) and 7.8 (right).

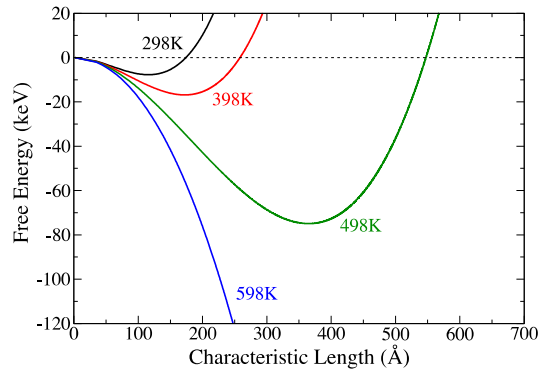


Figure 4.7 Plot of the free energy of the reaction, given by Eq. (4.8), forming an octahedral NFO particle (with characteristic length a) from divalent cations under the conditions specified by the deep CRUD conditions listed in Table 4.1.

4.1.3 Agglomeration and Deposition

A principle goal of this dissertation is to provide new insights into understanding CRUD deposition to inform continuum models. This work can be extended to provide more accurate, physically meaningful, values for parameters that are currently assumed or fit to data that appear in continuum models. An example of where the knowledge of the specific surface structure and termination can contribute to informing empirical models is found in the sticking probability for particles adhering to cladding [22,159] or existing CRUD. The value of the knowledge of the particle surfaces arises from Observa-

tions with hematite particles (more relevant to BWR CRUD) indicate that the hydrophobic nature of the particles cause them to attached to bubbles [21], which is also at the core of the model by Lister and Cussac [157]. First-principles modeling can also provide values for such quantities as the energy required to remove the water adsorbed onto a particle surface present in many models of particle deposition [159]. The results are consistent with observations [7] and existing models [3] that CRUD particles are located at SNB sites in the highest temperature region of the reactor.

Two theories are proposed which contribute to a deeper understanding of CRUD using the knowledge of surfaces and thermodynamics of particle nucleation and growth developed by this dissertation. First, an additional source of particles is proposed based on the stable NFO particles that may be generated at conditions expected to be encountered in CRUD. Second, a mechanism for particle agglomeration is proposed which originates from knowledge of the surface structure of the stable particles.

The commonly accepted source of the particles that deposit as CRUD are eroded from steam generator tubing and transported to the core [3,4,7–9]. This is likely the case due to the observed similarities of the particles found in the steam generators to those that form CRUD. However, the insights brought by this work to the surface chemistry of NiO and NFO leads to the proposal that there is another source of particles originating in the CRUD itself. This hypothesis is primarily based on the fact that the formation of NiO and NFO particles are stable only at the highest temperatures and pH conditions predicted to be encountered in CRUD. This suggests such particles nucleate either deep within the porous structure of the CRUD or grow at the water/steam interface of the steam chimneys as indicated by the schematic illustration in Fig. 4.8. Nucleation of particles in the presence of steam would also drive the formation of particles with denuded surfaces such as the predicted stable NFO particles. It is proposed that the particles nucleated in these environments will be transported through the steam chimney into the coolant where they could be brought back into contact with the outer surface of CRUD. This proposal explains why the outer layer of CRUD is observed to be made of loosely bound particles.

Regardless of the source of the particles, the detailed knowledge of the particle surfaces developed in this dissertation leads to a theory regarding the agglomeration of the particulate component of CRUD. Although limited data exists in the open literature regarding the morphology of CRUD at the sub-micron scale, what is present clearly shows that the outer layer of CRUD is partially made of agglomerations of smaller particles [9,14,26,160]. The prevalence of NFO in CRUD could be explained by the agglomeration of the stable octahedral particles. The particles are predicted to expose denuded surfaces which can strongly adhere with like surfaces on other particles to form agglomerates.

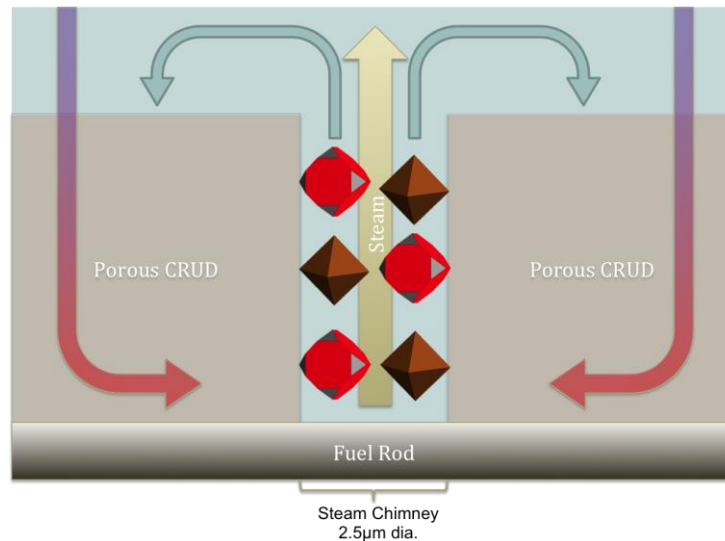


Figure 4.8 Schematic diagram illustrating the proposed mechanism of particle generation in CRUD.

4.2 Thermodynamics of Boron Incorporation in CRUD

The free energy of formation of Bonaccordite is calculated up to about 320°C, and the free energy changes as a function of temperature for several reactions that can lead to Bonaccordite are evaluated. This study suggests that the formation of Bonaccordite from aqueous metal ions and boric acid at concentrations found in PWR coolant

only becomes thermodynamically favorable at temperatures significantly above that of the bulk coolant. However, at the predicted solute concentrations, temperatures and pH of the fluid that exists inside the porous CRUD where Bonaccordite has been observed, the calculations predict that formation of Bonaccordite from dissolved ions is thermodynamically favorable. Hence the results from this study provide key information that is missing from current CRUD deposition models.

4.2.1 Calculations on Bulk Bonaccordite

Bonaccordite (Ni_2FeBO_5) is a member of the ludwigite group of boron containing minerals of the form $M_2^{+2}M^{+3}\text{O}_2\text{BO}_3$. It has only been found in nature at one site in the Bon Accord region of South Africa [161], and it is inadvertently produced in the cores of high-duty pressurized light-water nuclear reactors (PWRs) [14]. Bonaccordite is typically observed as long, slender cylinders or whiskers. It is insoluble in water and has a relatively high hardness equivalent to quartz. Bonaccordite has been synthesized by annealing a mixture of NiO, Fe_2O_3 and boric acid at a temperature of 1050°C followed by slow cooling [162]. It has also been made by hydrothermal synthesis starting at temperatures above 350°C [15].

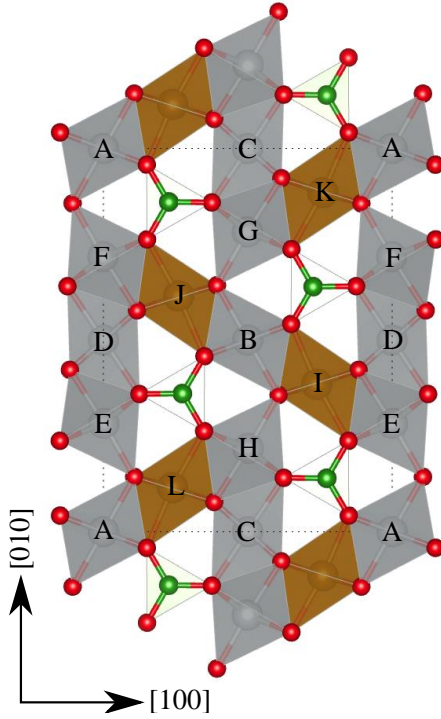


Figure 4.9 Illustration of the structure of the (111) plane of Bonaccordite (Ni_2FeBO_5). Nickel and iron sites are shown as grey (A-H) and brown (I-L) octahedrons, respectively. The unit cell is indicated by a fine dotted line.

Although Ludwigites are known to have disordered cations, for convenience this study assumes that the sites are occupied by the majority cation determined in Ref. [163]. The key structural feature of Bonaccordite is the presence of z-shaped pathways made of edge-sharing octahedral sites that propagate along the $[100]$ direction. The complete path illustrated in Fig. 4.9 consists of the sites, EDFJBIEDF, listed from left to right along the $[100]$ direction. The magnetic structure was examined for a ferrimagnetic configuration and four different antiferromagnetic configurations, summarized in Table 4.4:

- **FIM:** The ferrimagnetic configuration has all Ni and Fe sites coupled ferromagnetically with like sites, and Fe sites coupled antiferromagnetically to Ni sites. Up spins were assigned to sites A–H; down spins were assigned to sites I–L. This configuration results in a net moment of $0.942 \mu_B/\text{f.u.}$.

- **AFM1:** The configuration is described as having Ni sites antiferromagnetically coupled within a path, Fe sites coupled ferromagnetically within a path, but antiferromagnetically between paths. The sites A–D, I, and J are given as initial up spins; sites E–H, K, and L are set to be down spins.
- **AFM2:** The configuration is described as Ni sites coupled ferromagnetically in a path, and antiferromagnetically between paths. The Fe sites are coupled antiferromagnetically to the Ni within a path. Up spins are initially assigned to the A, C, and G–J sites, and down spins are assigned to B, D–F, and K–M sites.
- **AFM3:** The configuration is described as ferromagnetic coupling between all edge-sharing octahedral sites (those within a path), coupled antiferromagnetically to the neighboring paths. Up spins are assigned to A, C, G, H, K, and L sites; down spins are assigned to B, D–F, I, and J sites.
- **AFM4:** The configuration is simply described by antiferromagnetic coupling between all edge-sharing octahedral sites (those within a path). Sites B, C, E, F, K, and L are initialized with up spins; sites A, D, and G–J are initiated with down spins.

Table 4.4 Summary of detailed magnetic information and relative stability of calculated Bonaccordite structures with the five magnetic structures described in the text.

Spin Configuration	M_{net} ($\mu_B/\text{f.u.}$)	M_{Ni} (μ_B)	M_{Fe} (μ_B)	ΔE (meV/f.u.)
FIM	0.942	+ 1.76	- 4.28	0.0
AFM1	0.000	\pm 1.79	\pm 4.31	69.5
AFM2	0.000	\pm 1.77	\pm 4.29	14.0
AFM3	0.000	\pm 1.79	\pm 4.31	69.5
AFM4	0.000	\pm 1.79	\pm 4.31	96.3

The lowest energy magnetic structure observed in our calculations is ferrimagnetic (FIM), but is in disagreement with low temperature measurements that did not observe any remnant magnetization or hysteresis down to temperature of 4K [162]. To be consistent with experiments, the magnetic structure of the Bonaccordite in this study is taken to be of the AFM2 type, which had the lowest energy of the antiferromag-

netic configurations. All tests were carried out with a 4×3×12 k-point mesh and a summary of the bulk properties are reported in Table 4.5.

Table 4.5 Comparison of physical, electrical, and magnetic properties of Bonaccordite between this work and experimental values. Reference values are taken from Fernandes, *et al.* [162].

Property	Bonaccordite	
	AFM2 Configuration	
	(Ni ₂ FeBO ₅)	
	This work	Reference
a (Å)	9.289	9.209
b (Å)	12.315	12.232
c (Å)	3.019	3.002
E_g (eV)	~1.76	-
M_{net} (μ_B /f.u.)	0	0
Ni ²⁺ (μ_B)	±1.77	-
Fe ³⁺ (μ_B)	±4.29	-

Properties for a total of eight metal oxides are used to construct the ECPs as in Sec. 2.3 to create a set of coupled linear equations; these metal oxides are Fe₂O₃, FeO(OH), Fe₃O₄, NiO, ZnO, Co₃O₄, found in Eqns. (2.1)–(2.6) and B₂O₃ and Li₂O via

$$\Delta_f G_{\text{Li}_2\text{O}}^0(T) = E_{\text{Li}_2\text{O}}(0\text{K}) - 2\mu_{\text{Li}}^0(T) - \frac{1}{2}\mu_{\text{O}_2}^0(T), \quad (4.10)$$

$$\Delta_f G_{\text{B}_2\text{O}_3}^0(T) = E_{\text{B}_2\text{O}_3}(0\text{K}) - 2\mu_{\text{B}}^0(T) - \frac{3}{2}\mu_{\text{O}_2}^0(T). \quad (4.11)$$

Details of the calculated crystal structure, along with mechanical and magnetic properties are reported in Sec. 3.1 and Table 4.6.

Table 4.6 Comparison of physical, electrical, and magnetic properties of lithium and boron oxides calculated in this work with experimental values. Superscript letters indicate the reference: ^a[164], ^b[165], ^c[166], ^d[167], ^e[168], ^f[169], ^gcalculated value using GGA with exact exchange (experiment unavailable) [170], ^hcalculated [171]. The data for lithium containing compounds were provided by A. D. Andersson at Los Alamos National Lab.

Property	Lithium Oxide (Li ₂ O)		Boron Trioxide (B ₂ O ₃)		Lithium Metaborate (LiBO ₂)		Lithium Tetraborate (Li ₂ B ₄ O ₇)	
	This work	Ref.	This Work	Ref.	This work	Ref.	This work	Ref.
<i>a</i> (Å)	4.635	4.619 ^d	4.403	4.336 ^c	7.0651	5.746 ^e	9.5582	9.479 ^f
<i>b</i> (Å)	4.635	4.619 ^d	4.403	4.336 ^c	4.3968	4.397 ^e	9.5582	9.479 ^f
<i>c</i> (Å)	4.635	4.619 ^d	8.749	8.340 ^c	12.4734	6.662 ^e	10.9034	10.290 ^f
<i>E_g</i> (eV)	5.172	7.99 ^b	6.773	6.2 ^a	5.397	8.25 ^g	5.807	8.87 ^g
B (GPa)	79.79	—	—	60 ^h	39.36	—	37.61	—

These eight coupled equations can be solved to define ECPs ($\mu^0(T)$) for each element: Fe, O, H, Ni, Zn, Co, B and Li. To validate the method, the effective chemical potentials were used to predict free energies of formation of three ferrites that contain iron and one other metal, NiFe₂O₄, CoFe₂O₄, and ZnFe₂O₄, as well as Li₂B₄O₇ and LiBO₂. The free energies calculated from the effective chemical potentials (found by solving Eqns. (2.1)–(2.6), (4.12), and (4.13)) reproduce experimental values from 298.15 to 598.15K with maximum deviations in kJ/mol (R^2 values) of 1.0913 (0.9995), 0.0348 (1.0000), 4.2154 (0.9914), 1.7194 (0.9965), and 8.1762 (0.9900) for NiFe₂O₄, CoFe₂O₄, ZnFe₂O₄, LiBO₂, and Li₂B₄O₇, respectively. The 0K DFT energy for these materials is reported in Tables 3.11 and 4.7 .

Table 4.7 This table supplements Table 3.11 by adding oxides containing boron and lithium.

Material	Formula	k-point mesh	<i>E</i> (0K) (kJ/mol)
Boron Trioxide	B ₂ O ₃	4×4×2	-3870.4508
Lithium Oxide	Li ₂ O		-1381.2831
Lithium Metaborate	LiBO ₂		-2711.6935
Lithium Tetraborate	Li ₂ B ₄ O ₇		-9352.9381
Bonaccordite	Ni ₂ BFeO ₅	4×3×12	-5582.0082

Water, solvated Fe^{+2} , Ni^{+2} and their hydroxides are incorporated via equations (2.10)–(2.13), while boric and acid aqueous Li^+ ions incorporated into the scheme via:

$$\left(\Delta_f G_{\text{H}_3\text{BO}_3}(T, P)\right)_{aq} = \left(\mu_{\text{H}_3\text{BO}_3}(T, P)\right)_{aq} - \mu_{\text{B}}^0(T) - \frac{3}{2}\mu_{\text{H}_2}^0(T) - \frac{3}{2}\mu_{\text{O}_2}^0(T), \quad (4.12)$$

$$\left(\Delta_f G_{\text{Li}^+}(T, P)\right)_{aq} = \left(\mu_{\text{Li}^+}(T, P)\right)_{aq} - \mu_{\text{Li}}^0(T) - \frac{1}{2}\mu_{\text{H}_2}^0(T) + \left(\mu_{\text{H}^+}(T, P)\right)_{aq}. \quad (4.13)$$

To incorporate Bonaccordite into future PWR metal-oxide deposition models, this study predicts the standard Gibbs free energy of formation $\Delta_f G_{\text{Ni}_2\text{FeBO}_5}^0(T)$ via

$$\Delta_f G_{\text{Ni}_2\text{FeBO}_5}^0(T) = E_{\text{Ni}_2\text{FeBO}_5}(0\text{K}) - 2\mu_{\text{Ni}}^0(T) - \mu_{\text{Fe}}^0(T) - \mu_{\text{B}}^0(T) - \frac{5}{2}\mu_{\text{O}_2}^0(T), \quad (4.14)$$

where $E_{\text{Ni}_2\text{FeBO}_5}(0\text{K})$ is the GGA+U calculated energy of Bonaccordite at 0K, provided in Table 4.7, and the chemical potentials are as previously defined. The ECPs of the elements, used in the present Bonaccordite analysis are fit to the function

$$\mu_A^0(T) = a + bT + cT \ln(T) + dT^2 + \frac{e}{T}. \quad (4.15)$$

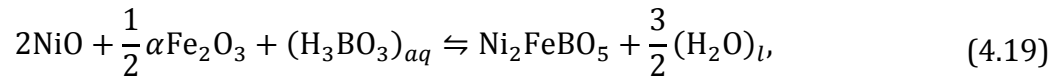
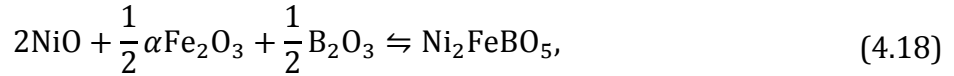
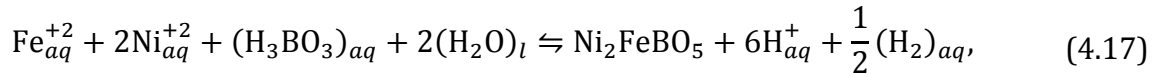
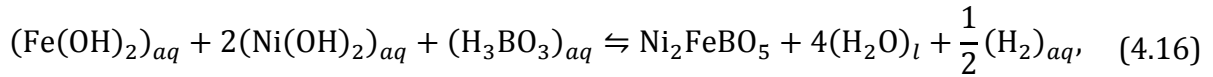
The resulting free energy of formation of Bonaccordite is given by Eq. (4.14) with coefficients in the bottom row of Table 4.8.

Table 4.8 The first seven rows contain coefficients for Eq. (4.15) that have been fit to the elemental effective chemical potentials derived above. The bottom row contains coefficients for Eq. (4.15) that are fit to the calculated free energy of formation of Bonaccordite calculated using Eq. (4.14).

Species	<i>a</i>	<i>b</i>	<i>c</i> (10^{-3})	<i>d</i> (10^{-6})	<i>e</i>
Fe	-834.6859	3.3319	-477.7022	268.2382	25847.5007
Ni	-444.7136	1.7857	-254.1135	136.2051	15029.6734
Co	-747.6997	3.3360	-478.4589	253.8193	26248.6098
Zn	-337.9925	3.6425	-536.2993	346.6793	23042.4735
O ₂	-536.1590	-4.4739	611.5139	-316.8325	-34399.8178
H ₂	-820.7220	1.4724	-229.8178	99.9242	16524.3717
B	-551.2513	-1.9669	327.8514	-344.2570	1059.5673
Li	-316.8768	1.9986	-295.4849	174.8006	12378.8270
Ni ₂ FeBO ₅	-1522.1120	-0.4476	145.1477	-161.8992	-2606.0234

4.2.2 Thermodynamics of Bonaccordite Formation

Because of a lack of information regarding the thermodynamics of Bonaccordite, the thermodynamics of possible formation mechanisms is investigated. Sawicki [15] synthesized Bonaccordite from Hematite ($\alpha\text{Fe}_2\text{O}_3$), nickel oxide (NiO), and either boron oxide (B_2O_3) or boric acid (H_3BO_3) precursors that are present in a nuclear reactor. However, other synthesis routes are possible including the formation from aqueous metal ions (Eqns. (4.16) and (4.17)) and other metal oxides (Eqns. (4.18) and (4.19)):



To be consistent with conditions in typical operating conditions of a PWR are described in Table 4.1. Using these concentrations, the free energy of reactions involving aqueous species given by Eqns. (4.16)–(4.19) are plotted in Fig. 4.10.

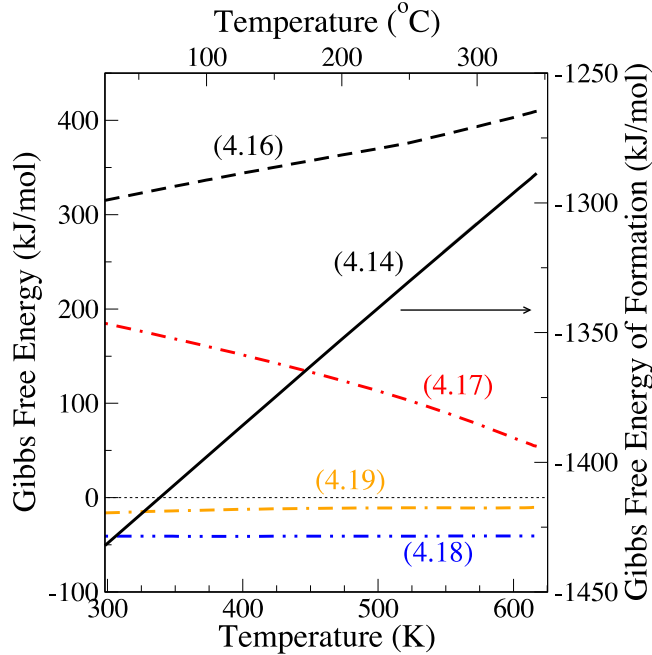


Figure 4.10 The predicted standard Gibbs free energy of formation of Bonaccordite (Eq. (4.14)) is plotted as a solid line that corresponds to the energy scale on the right. Dotted lines denote the new Gibbs Free energy for possible synthesis reactions in PWRs that are denoted by Eqns. (4.16)–(4.19). Numbers labeling lines on the plot correspond to the reactions given in Eqn. (4.14), and (4.16)–(4.19). Concentrations of aqueous species are taken to be the observed values in the coolant at a pressure of 155bar.

The formation of Bonaccordite is thermodynamically favored to proceed through the reaction of binary oxides (Eq. (4.18)) or binary metal oxides and boric acid (Eq. (4.19)) at all temperatures, although apparently with a high activation energy [162]. However, in a PWR environment the source of the metals will be hydrated ions or NiFe_2O_4 already present in the porous CRUD, and the boron will be present as boric acid, which is better represented by Eqs. (4.16) and (4.17). Using the conditions given in Table 4.1, the current thermodynamic model does not predict the formation of Bonaccordite at PWR temperatures as shown by Fig. 4.10. Given the apparent need for near or supercritical conditions not present in coolant, it is useful to examine conditions present where Bonaccordite is observed to form in CRUD.

Bonaccordite is observed to form in an approximately 30–40 μm thick region near the clad side of the CRUD. CRUD deposition models predict that solute concentra-

tions, temperature and pH of the fluid flowing in the porous CRUD are significantly different from the bulk coolant conditions. It is therefore possible that the thermodynamic stability of Bonaccordite may change inside the porous CRUD. A CRUD deposition model reported in Table 4.1 predicts that boric acid concentrations will be increased, $(\text{H}_2)_{aq}$ concentrations will decrease, pH will exceed 7.8, and temperature may reach $\sim 643.15\text{K}$ (370°C). The model assumes $60\mu\text{m}$ thick CRUD and predictions made using 1200ppm boric acid are taken from the model. In addition, the models predict that lithium metaborate, rather than lithium tetraborate, will precipitate at conditions approximately $40\mu\text{m}$ into the CRUD. The effect of using the concentrations and pH predicted inside the CRUD is plotted in Fig. 4.11. Because the concentration of metal ions and hydroxides are already at or near the solubility limit, it is unlikely that they will vary substantially from the coolant values. Assuming the previously predicted conditions are valid inside CRUD, the relative energy of the possible synthesis reactions remains unchanged, but the reaction given by Eq. (4.17) is shifted down, which predicts Bonaccordite to be stable at subcritical temperatures within the range of temperatures predicted by existing CRUD models at the depth where Bonaccordite forms. This result lends credibility to the thermodynamic model developed here and the as yet unmeasured free energy of formation of Bonaccordite.

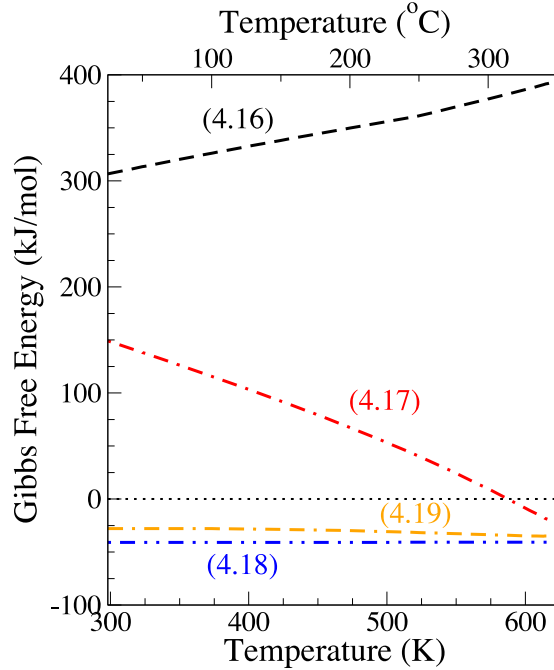
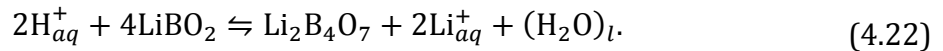
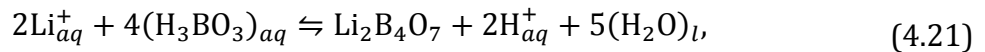
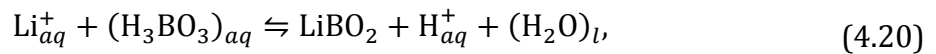


Figure 4.11 Possible synthesis reactions in PWR CRUD (Eqns. (4.16)–(4.19)). Numbers labeling lines on the plot correspond to the reactions given in Eqns. (4.16)–(4.19). Concentrations of aqueous species are taken to be the values predicted by the CRUD models of EPRI and Henshaw, *et al.* at a depth of 40 μm in 60 μm CRUD assuming a bulk coolant pressure of 155bar. The temperature predicted in these models is in excess of that included in the aqueous species database used to parameterize the current work.

4.2.3 Formation of Lithium Borates in CRUD

Bonaccordite is only observed to form in extreme conditions predicted deep within the CRUD. However, CIPS is observed in CRUD as thin as 20–30 μm [12] which corresponds to less extreme conditions which require another mechanism by which boron becomes trapped in the CRUD. In considering other mechanisms for incorporation of Li and B into CRUD, we propose the reactions:



These reactions are designed to test the conventional model of lithium metaborate formation (Eq. (4.20)) and the revised understanding that predicts the formation of lithium tetraborate (Eq. (4.21)). Also considered is the possibility that lithium metabo-

rate is unstable and converts to lithium tetraborate via the reaction of Eq. (4.22). Unfortunately, limited information was available regarding the conditions predicted for 30 μm thick CRUD. As a result, the plot of reactions (4.17), and (4.20)–(4.22) presented in Fig. 4.12 employ the same conditions used to generate Fig. 4.11.

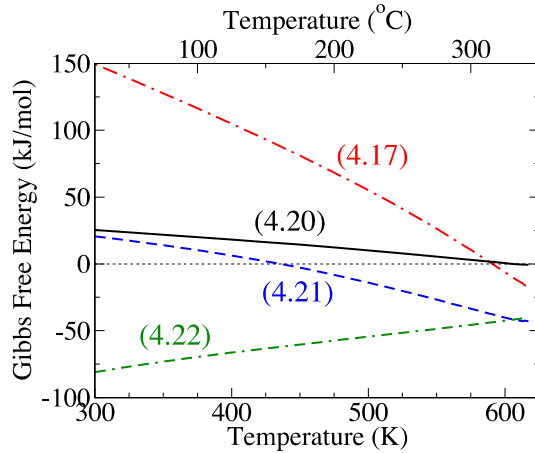


Figure 4.12 A plot of the reactions given by Eqns. (4.17), and (4.20)–(4.22) illustrates the relative free energies of some possible mechanisms for boron incorporation into CRUD. Concentrations of aqueous species are taken to be the values predicted by the CRUD models of EPRI and Henshaw, *et al.* at a depth of 40 μm in 60 μm thick CRUD assuming a bulk coolant pressure of 155bar. The temperature predicted by these models is in excess of that included in the aqueous species database used to parameterize the current work.

This study makes the first prediction of the Gibbs standard free energy of formation of the mineral Bonaccordite and examines the thermodynamics of possible pathways to its formation in PWR operating environments. This study suggests that the formation of Bonaccordite from aqueous metal ions and boric acid is thermodynamically favorable at the conditions predicted to exist inside CRUD where it is observed to form. The results of this study provide critical data that are missing in current PWR CRUD deposition models. As a validation of the model, we demonstrated that the other primary mechanism of boron incorporation (via the formation of lithium tetraborate) is

also thermodynamically favorable under the conditions predicted to exist within the CRUD.

REFERENCES

- [1] Committee on Review of DOE's Nuclear Energy Research and Development Program National Research Council, Review of DOE's Nuclear Energy Research and Development Program, The National Academies Press, Washington, D.C., 2008.
- [2] K. Edsinger, C.R. Stanek, B.D. Wirth, Light water reactor fuel performance: Current status, challenges, and future high fidelity modeling, JOM. 63 (2011) 49–52.
- [3] J. Deshon, D. Hussey, B. Kendrick, J. McGurk, J. Secker, M. Short, Pressurized water reactor fuel crud and corrosion modeling, JOM. 63 (2011) 64–72.
- [4] R. Castelli, Nuclear Corrosion Modeling - The Nature of CRUD, Elsevier Inc., 2010.
- [5] IAEA, Optimization of Water Chemistry to Ensure Reliable Water Reactor Fuel Performance at High Burnup and in Ageing Plant (FUWAC), 1st ed., IAEA, Vienna, 2011.
- [6] D.A. Andersson, C.R. Stanek, Mixing and non-stoichiometry in Fe-Ni-Cr-Zn-O spinel compounds: density functional theory calculations., Phys. Chem. Chem. Phys. 15 (2013) 15550–64.
- [7] EPRI, Modeling PWR Fuel Corrosion Product Deposition and Growth Processes, Palo Alto, CA, 2004.
- [8] J.A. Sawicki, Analyses of crud deposits on fuel rods in PWRs using Mössbauer spectroscopy, J. Nucl. Mater. 402 (2010) 124–129.
- [9] J.-W. Yeon, I.-K. Choi, K.-K. Park, H.-M. Kwon, K. Song, Chemical analysis of fuel crud obtained from Korean nuclear power plants, J. Nucl. Mater. 404 (2010) 160–164.
- [10] R. Riess, K. Lundgren, LCC-2 Special Topic Report: CRUD in PWR/VVER and BWR Primary Circuits, Skultuna, Sweden, 2006.
- [11] EPRI, Modeling PWR Fuel Corrosion Product Deposition and Growth Process: Final Report, Palo Alto, CA, 2005.

- [12] J. Henshaw, J.C. McGurk, H.E. Sims, A. Tuson, S. Dickinson, J. Deshon, A model of chemistry and thermal hydraulics in PWR fuel crud deposits, *J. Nucl. Mater.* 353 (2006) 1–11.
- [13] I.U. Haq, N. Cinosi, M. Bluck, G. Hewitt, S. Walker, Modelling heat transfer and dissolved species concentrations within PWR crud, *Nucl. Eng. Des.* 241 (2011) 155–162.
- [14] J.A. Sawicki, Evidence of Ni_2FeBO_5 and m-ZrO_2 precipitates in fuel rod deposits in AOA-affected high boiling duty PWR core, *J. Nucl. Mater.* 374 (2008) 248–269.
- [15] J.A. Sawicki, Hydrothermal synthesis of Ni_2FeBO_5 in near-supercritical PWR coolant and possible effects of neutron-induced ^{10}B fission in fuel crud, *J. Nucl. Mater.* 415 (2011) 179–188.
- [16] S. Uchida, Y. Asakura, H. Suzuki, Deposition of boron on fuel rod surface under sub-cooled boiling conditions—An approach toward understanding AOA occurrence, *Nucl. Eng. Des.* 241 (2011) 2398–2410.
- [17] EPRI, Adsorption of Boric Acid on Synthetic Fuel Crud Oxides, Palo Alto, CA, 2002.
- [18] P. V Kumar, M.P. Short, S. Yip, B. Yildiz, J.C. Grossman, First-Principles Assessment of the Reactions of Boric Acid on $\text{NiO}(001)$ and $\text{ZrO}_2(\text{T}11)$ Surfaces, *J. Phys. Chem. C.* 116 (2012) 10113–10119.
- [19] H. Bindra, B.G. Jones, Deposition of metallic colloids under sub-cooled nucleate boiling, *Colloids Surfaces A Physicochem. Eng. Asp.* 397 (2012) 85–91.
- [20] J.-W. Yeon, Y. Jung, S.-I. Pyun, Deposition behaviour of corrosion products on the Zircaloy heat transfer surface, *J. Nucl. Mater.* 354 (2006) 163–170.
- [21] T. Iwahori, T. Mizuno, H. Kōyama, Role of Surface Chemistry in Crud Deposition on Heat Transfer Surface, *Corrosion.* 35 (1979) 345–350.
- [22] K.A. Dinov, A model of crud particle/wall interaction and deposition in a pressurized water reactor primary system, *Nucl. Technol.* 94 (1991) 281–284.
- [23] C. Pan, B.G. Jones, A.J. Machiels, Concentration levels of solutes in porous deposits with chimneys under wick boiling conditions, *Nucl. Eng. Des.* 99 (1987) 317–327.
- [24] K.-H. Neeb, *The Radiochemistry of Nuclear Power Plants with Light Water Reactors*, De Gruyter, Berlin, New York, 1997.

- [25] P. Belouschek, K. Hof, M. Maas, S. Nowicki, Modelling of transport and deposition of corrosion products in primary circuits, in: British Nuclear Energy Society (Ed.), Water Chem. Nucl. React. Syst. 7, Thomas Telford Publishing, London, 1996: pp. 280–283.
- [26] EPRI, Simulated Fuel Crud Thermal Conductivity Measurements Under Pressurized Water Reactor Conditions, Palo Alto, CA, 2011.
- [27] K.M. Rabe, First-Principles Calculations of Complex Metal-Oxide Materials, Annu. Rev. Condens. Matter Phys. 1 (2010) 211–235.
- [28] V. Anisimov, I. Elfimov, N. Hamada, K. Terakura, Charge-ordered insulating state of Fe_3O_4 from first-principles electronic structure calculations, Phys. Rev. B. Condens. Matter. 54 (1996) 4387–4390.
- [29] H.-T. Jeng, G.Y. Guo, D.J. Huang, Charge-Orbital Ordering and Verwey Transition in Magnetite, Phys. Rev. Lett. 93 (2004) 156403.
- [30] S.L. Dudarev, G.A. Botton, S.Y. Savrasov, C.J. Humphreys, A.P. Sutton, Electron-energy-loss spectra and the structural stability of nickel oxide: An LSDA+U study, Phys. Rev. B. 57 (1998) 1505–1509.
- [31] G. Sawatzky, J. Allen, Magnitude and Origin of the Band Gap in NiO, Phys. Rev. Lett. 53 (1984) 2339–2342.
- [32] R.O. Jones, O. Gunnarsson, The density functional formalism, its applications and prospects, Rev. Mod. Phys. 61 (1989) 689–746.
- [33] J. Hafner, Ab-initio simulations of materials using VASP: Density-functional theory and beyond, J. Comput. Chem. 29 (2008) 2044–2078.
- [34] P. Liao, E.A. Carter, Ab initio DFT+U predictions of tensile properties of iron oxides, J. Mater. Chem. 20 (2010) 6703.
- [35] A. Janotti, D. Segev, C. Van de Walle, Effects of cation d states on the structural and electronic properties of III-nitride and II-oxide wide-band-gap semiconductors, Phys. Rev. B. 74 (2006) 045202.
- [36] R.C. Albers, N.E. Christensen, A. Svane, Hubbard- U band-structure methods, J. Phys. Condens. Matter. 21 (2009) 343201.
- [37] K. Laasonen, M. Sprik, M. Parrinello, R. Car, “Ab initio” liquid water, J. Chem. Phys. 99 (1993) 9080.

- [38] G. Kresse, J. Hafner, Ab initio molecular dynamics for liquid metals, *Phys. Rev. B.* 47 (1993) 558.
- [39] H. Lukas, S.G. Fries, B. Sundman, *Computational Thermodynamics: The CALPHAD Method*, Cambridge University Press, 2007.
- [40] L.-Q. Chen, Phase-Field Models for Microstructure Evolution, *Annu. Rev. Mater. Res.* 32 (2002) 113–140.
- [41] E. Kaxiras, Y. Bar-Yam, J.D. Joannopoulos, K.C. Pandey, Ab initio theory of polar semiconductor surfaces. I. Methodology and the (2x2) reconstructions of GaAs (111), *Phys. Rev. B.* 35 (1987) 9625–9635.
- [42] K.A. Persson, B. Waldwick, P. Lazic, G. Ceder, Prediction of solid-aqueous equilibria: Scheme to combine first-principles calculations of solids with experimental aqueous states, *Phys. Rev. B.* 85 (2012) 235438.
- [43] K. Reuter, M. Scheffler, First-Principles Atomistic Thermodynamics for Oxidation Catalysis: Surface Phase Diagrams and Catalytically Interesting Regions, *Phys. Rev. Lett.* 90 (2003) 046103.
- [44] K. Reuter, C. Stampfl, M. Scheffler, Ab Initio Atomistic Thermodynamics and Statistical Mechanics of Surface Properties and Functions, in: S. Yip (Ed.), *Handb. Mater. Model.*, Springer, 2005: pp. 149–194.
- [45] M. Scheffler, J. Dabrowski, Parameter-free calculations of total energies, interatomic forces and vibrational entropies of defects in semiconductors, *Philos. Mag. A.* 58 (1988) 107–121.
- [46] K. Reuter, M. Scheffler, Composition, structure, and stability of RuO₂(110) as a function of oxygen pressure, *Phys. Rev. B.* 65 (2001) 035406.
- [47] G. Hautier, S.P. Ong, A. Jain, C.J. Moore, G. Ceder, Accuracy of density functional theory in predicting formation energies of ternary oxides from binary oxides and its implication on phase stability, *Phys. Rev. B.* 85 (2012) 155208.
- [48] W. Zhang, J. Smith, X.-G. Wang, Thermodynamics from ab initio computations, *Phys. Rev. B.* 70 (2004) 024103.
- [49] L. Wang, T. Maxisch, G. Ceder, Oxidation energies of transition metal oxides within the GGA+U framework, *Phys. Rev. B.* 73 (2006) 195107.

- [50] H. Guo, A.S. Barnard, Thermodynamic modelling of nanomorphologies of hematite and goethite, *J. Mater. Chem.* 21 (2011) 11566.
- [51] A. Jain, G. Hautier, S.P. Ong, C.J. Moore, C.C. Fischer, K.A. Persson, et al., Formation enthalpies by mixing GGA and GGA + U calculations, *Phys. Rev. B.* 84 (2011) 045115.
- [52] C.J. O'Brien, Z. Rák, D.W. Brenner, Free energies of (Co, Fe, Ni, Zn)Fe₂O₄ spinels and oxides in water at high temperatures and pressure from density functional theory: results for stoichiometric NiO and NiFe₂O₄ surfaces, *J. Phys. Condens. Matter.* 25 (2013) 445008.
- [53] H. Guo, A.S. Barnard, Surface Structure and Environment-Dependent Hydroxylation of the Nonpolar Hematite (100) from Density Functional Theory Modeling, *J. Phys. Chem. C.* 115 (2011) 23023–23029.
- [54] H. Guo, A.S. Barnard, Surface phase diagram of hematite pseudocubes in hydrous environments, *J. Mater. Chem.* 22 (2012) 161.
- [55] F. Zasada, W. Piskorz, P. Stelmachowski, A. Kotarba, J.-F. Paul, T. Płociński, et al., Periodic DFT and HR-STEM Studies of Surface Structure and Morphology of Cobalt Spinel Nanocrystals. Retrieving 3D Shapes from 2D Images, *J. Phys. Chem. C.* 115 (2011) 6423–6432.
- [56] D.J. Binks, R.W. Grimes, A.L. Rohl, D.H. Gay, Morphology and structure of ZnCr₂O₄ spinel crystallites, *J. Mater. Sci.* 31 (1996) 1151–1156.
- [57] M.J. Davies, S.C. Parker, G.W. Watson, Atomistic simulation of the surface structure of spinel, *J. Mater. Chem.* 4 (1994) 813.
- [58] A. Barnard, Z. Saponjic, D. Tiede, T. Rajh, Multi-scale modeling of titanium dioxide: controlling shape with surface chemistry, *Rev. Adv. Mater. Sci.* 10 (2005) 21–27.
- [59] A.S. Barnard, P. Zapol, Predicting the Energetics, Phase Stability, and Morphology Evolution of Faceted and Spherical Anatase Nanocrystals, *J. Phys. Chem. B.* 108 (2004) 18435–18440.
- [60] A. Barnard, P. Zapol, Effects of particle morphology and surface hydrogenation on the phase stability of TiO₂, *Phys. Rev. B.* 70 (2004) 235403.
- [61] J.P. Perdew, K. Burke, M. Ernzerhof, Generalized Gradient Approximation Made Simple, *Phys. Rev. Lett.* 77 (1996) 3865–3868.

- [62] J.P. Perdew, K. Burke, M. Ernzerhof, Erratum: Generalized Gradient Approximation Made Simple, *Phys. Rev. Lett.* 78 (1997) 1396.
- [63] G. Kresse, J. Furthmüller, Efficiency of ab-initio total energy calculations for metals and semiconductors using a plane-wave basis set, *Comput. Mater. Sci.* 6 (1996) 15.
- [64] G. Kresse, J. Furthmüller, Efficient iterative schemes for ab initio total-energy calculations using a plane-wave basis set, *Phys. Rev. B.* 54 (1996) 11169.
- [65] G. Kresse, J. Hafner, Ab initio molecular-dynamics simulation of the liquid-metal-amorphous-semiconductor transition in germanium, *Phys. Rev. B.* 49 (1994) 14251.
- [66] H. Guo, A. Barnard, Modeling the iron oxides and oxyhydroxides for the prediction of environmentally sensitive phase transformations, *Phys. Rev. B.* 83 (2011) 094112.
- [67] L. Zhu, K. Yao, Z. Liu, First-principles study of the polar (111) surface of Fe₃O₄, *Phys. Rev. B.* 74 (2006) 035409.
- [68] J. Chen, X. Wu, A. Selloni, Electronic structure and bonding properties of cobalt oxide in the spinel structure, *Phys. Rev. B.* 83 (2011) 1–7.
- [69] G. Kresse, D. Joubert, From ultrasoft pseudopotentials to the projector augmented-wave method, *Phys. Rev. B.* 59 (1999) 1758.
- [70] P.E. Blöchl, Projector augmented-wave method, *Phys. Rev. B.* 50 (1994) 17953.
- [71] H.J. Monkhorst, J.D. Pack, Special points for Brillouin-zone integrations, *Phys. Rev. B.* 13 (1976) 5188–5192.
- [72] F. Birch, Finite Elastic Strain of Cubic Crystals, *Phys. Rev.* 71 (1947) 809–824.
- [73] E.J.W. Verwey, Electronic Conduction of Magnetite (Fe₃O₄) and its Transition Point at Low Temperatures, *Nature.* 144 (1939) 327–328.
- [74] T. Windman, E.L. Shock, A web-based interactive version of SUPCRT92, *Geochim. Cosmochim. Acta.* 72 (2008) A1027.
- [75] J.W. Johnson, E.H. Oelkers, H.C. Helgeson, SUPCRT92: A software package for calculating the standard molal thermodynamic properties of minerals, gases,

- aqueous species, and reactions from 1 to 5000 bar and 0 to 1000°C, *Comput. Geosci.* 18 (1992) 899–947.
- [76] J.C. Tanger, H.C. Helgeson, Calculation of the thermodynamic and transport properties of aqueous species at high pressures and temperatures; revised equations of state for the standard partial molal properties of ions and electrolytes, *Am. J. Sci.* 288 (1988) 19–98.
- [77] E.L. Shock, H.C. Helgeson, Errata for Calculation of the thermodynamic and transport properties of aqueous species at high pressures and temperatures: Correlation algorithms for ionic species and equation of state predictions to 5 kb and 1000°C, *Geochim. Cosmochim. Acta.* 53 (1989) 215.
- [78] E.L. Shock, H.C. Helgeson, D.A. Sverjensky, Calculation of the thermodynamic and transport properties of aqueous species at high pressures and temperatures: Standard partial molal properties of inorganic neutral species, *Geochim. Cosmochim. Acta.* 53 (1989) 2157–2183.
- [79] E.L. Shock, H.C. Helgeson, Calculation of the thermodynamic and transport properties of aqueous species at high pressures and temperatures: Correlation algorithms for ionic species and equation of state predictions to 5 kb and 1000°C, *Geochim. Cosmochim. Acta.* 52 (1988) 2009–2036.
- [80] D.J. Wesolowski, S.E. Ziemniak, L.M. Anovitz, M.L. Machesky, P. Bénézech, D.A. Palmer, Solubility and surface adsorption characteristics of metal oxides, in: D.A. Palmer, R. Fernández-Prini, A.H. Harvey (Eds.), *Aqueous Syst. Elev. Temp. Press. Phys. Chem. Water, Steam Hydrothermal Solut.*, 1st ed., Elsevier Ltd., London, 2004: pp. 493–595.
- [81] V. Majer, J. Sedlbauer, R.H. Wood, Calculation of standard thermodynamic properties of aqueous electrolytes and nonelectrolytes, in: D.A. Palmer, R. Fernández-Prini, A.H. Harvey (Eds.), *Aqueous Syst. Elev. Temp. Press. Phys. Chem. Water, Steam Hydrothermal Solut.*, 1st ed., Elsevier Ltd., London, 2004: pp. 99–147.
- [82] R.J. Silbey, R.A. Alberty, M.G. Bawendi, *Physical Chemistry*, 4th ed., John Wiley & Sons, Inc., 2005.
- [83] J. Barrett, Liquid water and the hydration of ions, in: *Inorg. Chem. Aqueous Solut.*, Royal Society of Chemistry, Cambridge, 2003: pp. X001–X004.
- [84] W.-B. Zhang, B.-Y. Tang, Stability of the polar NiO(111) surface., *J. Chem. Phys.* 128 (2008) 124703.

- [85] N. Yu, W.-B. Zhang, N. Wang, Y.-F. Wang, B.-Y. Tang, Water Adsorption on a NiO(100) Surface: A GGA+U Study, *J. Phys. Chem. C.* 112 (2008) 452–457.
- [86] A. Cheetham, D. Hope, Magnetic ordering and exchange effects in the antiferromagnetic solid solutions $Mn_xNi_{1-x}O$, *Phys. Rev. B.* 27 (1983) 6964–6967.
- [87] W.L. Roth, The magnetic structure of Co_3O_4 , *J. Phys. Chem. Solids.* 25 (1964) 1–10.
- [88] J. van Elp, J. Wieland, H. Eskes, P. Kuiper, G. Sawatzky, F. de Groot, et al., Electronic structure of CoO, Li-doped CoO, and LiCoO₂, *Phys. Rev. B.* 44 (1991) 6090–6103.
- [89] A.S. Mohammadi, S.M. Baizae, H. Salehi, Density Functional Approach to Study Electronic Structure of ZnO Single Crystal, *World Appl. Sci. J.* 14 (2011) 1530–1536.
- [90] S.Z. Karazhanov, P. Ravindran, A. Kjekshus, H. Fjellvåg, U. Grossner, B.G. Svensson, Coulomb correlation effects in zinc monochalcogenides, *J. Appl. Phys.* 100 (2006) 043709.
- [91] F. Decremps, F. Datchi, A. Saitta, A. Polian, S. Pascarelli, A. Di Cicco, et al., Local structure of condensed zinc oxide, *Phys. Rev. B.* 68 (2003) 104101.
- [92] A. Mang, K. Reimann, S. Rübenacke, Band gaps, crystal-field splitting, spin-orbit coupling, and exciton binding energies in ZnO under hydrostatic pressure, *Solid State Commun.* 94 (1995) 251–254.
- [93] M.E. Grillo, M.W. Finnis, W. Ranke, Surface structure and water adsorption on $Fe_3O_4(111)$: Spin-density functional theory and on-site Coulomb interactions, *Phys. Rev. B.* 77 (2008) 075407.
- [94] R.M. Cornell, U. Schwertmann, *The Iron Oxides: Structure, Properties, Reactions, Occurrences and Uses*, 2nd ed., Wiley-VCH, Weinheim, Germany, 2003.
- [95] D.M. Sherman, Electronic structures of iron(III) and manganese(IV) (hydr)oxide minerals: Thermodynamics of photochemical reductive dissolution in aquatic environments, *Geochim. Cosmochim. Acta.* 69 (2005) 3249–3255.
- [96] R. Waldron, Infrared Spectra of Ferrites, *Phys. Rev.* 99 (1955) 1727–1735.
- [97] H. Yang, R. Lu, R.T. Downs, G. Costin, Goethite, α -FeO(OH), from single-crystal data, *Acta Crystallogr. Sect. E Struct. Reports Online.* 62 (2006) i250–i252.

- [98] B. Russell, M. Payne, L. Ciacchi, Density functional theory study of Fe(II) adsorption and oxidation on goethite surfaces, *Phys. Rev. B.* 79 (2009).
- [99] A.T. Raghavender, K. Zadro, D. Pajic, Z. Skoko, N. Biliškov, Effect of grain size on the Néel temperature of nanocrystalline nickel ferrite, *Mater. Lett.* 64 (2010) 1144–1146.
- [100] D. Fritsch, C. Ederer, Epitaxial strain effects in the spinel ferrites CoFe_2O_4 and NiFe_2O_4 from first principles, *Phys. Rev. B.* 82 (2010) 104117.
- [101] Z. Li, E.S. Fisher, J.Z. Liu, M. V. Nevitt, Single-crystal elastic constants of Co-Al and Co-Fe spinels, *J. Mater. Sci.* 26 (1991) 2621–2624.
- [102] S.I. Youssef, M.G. Natera, R.J. Begum, B.S. Srinivasan, N.S.S. Murthy, Polarised neutron diffraction study of nickel ferrite, *J. Phys. Chem. Solids.* 30 (1969) 1941–1948.
- [103] S. Soliman, A. Elfalaky, G. Fecher, C. Felser, Electronic structure calculations for ZnFe_2O_4 , *Phys. Rev. B.* 83 (2011) 085205.
- [104] C. Cheng, Long-range antiferromagnetic interactions in ZnFe_2O_4 and CdFe_2O_4 : Density functional theory calculations, *Phys. Rev. B.* 78 (2008) 132403.
- [105] K. Kamazawa, Y. Tsunoda, H. Kadowaki, K. Kohn, Magnetic neutron scattering measurements on a single crystal of frustrated ZnFe_2O_4 , *Phys. Rev. B.* 68 (2003) 024412.
- [106] T. Usa, K. Kamazawa, H. Sekiya, S. Nakamura, Y. Tsunoda, K. Kohn, et al., Magnetic Properties of ZnFe_2O_4 as a 3-D Geometrical Spin Frustration System, *J. Phys. Soc. Japan.* 73 (2004) 2834–2840.
- [107] D. Singh, M. Gupta, R. Gupta, Density-functional description of spinel ZnFe_2O_4 , *Phys. Rev. B.* 63 (2001) 205102.
- [108] J. Takaobushi, M. Ishikawa, S. Ueda, E. Ikenaga, J.-J. Kim, M. Kobata, et al., Electronic structures of $\text{Fe}_{3-x}\text{M}_x\text{O}_4$ (M=Mn,Zn) spinel oxide thin films investigated by x-ray photoemission spectroscopy and x-ray magnetic circular dichroism, *Phys. Rev. B.* 76 (2007).
- [109] A. Walsh, S.-H. Wei, Y. Yan, M. Al-Jassim, J. Turner, M. Woodhouse, et al., Structural, magnetic, and electronic properties of the Co-Fe-Al oxide spinel system: Density-functional theory calculations, *Phys. Rev. B.* 76 (2007) 165119.

- [110] Y.H. Hou, Y.J. Zhao, Z.W. Liu, H.Y. Yu, X.C. Zhong, W.Q. Qiu, et al., Structural, electronic and magnetic properties of partially inverse spinel CoFe_2O_4 : a first-principles study, *J. Phys. D. Appl. Phys.* 43 (2010) 445003.
- [111] G.H. Jonker, Analysis of the semiconducting properties of cobalt ferrite, *J. Phys. Chem. Solids.* 9 (1959) 165–175.
- [112] M.W. Chase, NIST-JANAF Thermochemical Tables, 4th ed., American Chemical Society, Washington, D.C., 1998.
- [113] L.B. Pankratz, Thermodynamic Properties of Elements and Oxides, U.S. Dept. of the Interior, Bureau of Mines, Washington, D.C., 1982.
- [114] I. Barin, O. Knacke, Thermochemical properties of inorganic substances, 2nd ed., Springer-Verlag, Berlin, 1991.
- [115] O. Knacke, K. Hesselmann, O. Kubaschewski, Thermochemical properties of inorganic substances, 2nd ed., Springer-Verlag, Berlin; Düsseldorf, 1991.
- [116] A.S. Barnard, P. Zapol, L.A. Curtiss, Anatase and rutile surfaces with adsorbates representative of acidic and basic conditions, *Surf. Sci.* 582 (2005) 173–188.
- [117] A.S. Barnard, H. Xu, An environmentally sensitive phase map of titania nanocrystals, *ACS Nano.* 2 (2008) 2237–42.
- [118] X.-L. Xu, Z.-H. Chen, Y. Li, W.-K. Chen, J.-Q. Li, Bulk and surface properties of spinel Co_3O_4 by density functional calculations, *Surf. Sci.* 603 (2009) 653–658.
- [119] N.H. de Leeuw, T.G. Cooper, Surface simulation studies of the hydration of white rust $\text{Fe}(\text{OH})_2$, goethite $\alpha\text{-FeO}(\text{OH})$ and hematite $\alpha\text{-Fe}_2\text{O}_3$, *Geochim. Cosmochim. Acta.* 71 (2007) 1655–1673.
- [120] S.K. Ghose, S.C. Petitto, K.S. Tanwar, Surface Structure and Reactivity of Iron Oxide – Water Interfaces, *Dev. Earth Environ. Sci.* 9197 (2008) 1–29.
- [121] N. Mulakaluri, R. Pentcheva, M. Scheffler, Coverage-Dependent Adsorption Mode of Water on Fe_3O_4 (001): Insights from First Principles Calculations, *J. Phys. Chem. C.* 114 (2010) 11148–11156.
- [122] R. Pentcheva, F. Wendler, H.L. Meyerheim, W. Moritz, N. Jedrecy, M. Scheffler, Jahn-Teller Stabilization of a “Polar” Metal Oxide Surface: $\text{Fe}_3\text{O}_4(001)$, *Phys. Rev. Lett.* 94 (2005) 126101.

- [123] R. Pentcheva, W. Moritz, J. Rundgren, S. Frank, D. Schrupp, M. Scheffler, A combined DFT/LEED-approach for complex oxide surface structure determination: Fe₃O₄(001), Surf. Sci. 602 (2008) 1299–1305.
- [124] J. Ciston, A. Subramanian, D.M. Kienzle, L.D. Marks, Why the case for clean surfaces does not hold water: Structure and morphology of hydroxylated nickel oxide (111), Surf. Sci. 604 (2010) 155–164.
- [125] P.W. Tasker, The stability of ionic crystal surfaces, J. Phys. C Solid State Phys. 12 (1979) 4977–4984.
- [126] D.J. Simpson, T. Bredow, A.R. Gerson, MSINDO study of water adsorption on NiO surfaces, Theor. Chem. Acc. 114 (2005) 242–252.
- [127] N. Kitakatsu, V. Maurice, C. Hinnen, P. Marcus, Surface hydroxylation and local structure of NiO thin films formed on Ni(111), Surf. Sci. 407 (1998) 36–58.
- [128] D. Cappus, C. Xu, D. Ehrlich, B. Dillmann, C.A. Ventrice, K. Al Shamery, et al., Hydroxyl groups on oxide surfaces: NiO(100), NiO(111) and Cr₂O₃(111), Chem. Phys. 177 (1993) 533–546.
- [129] M.A. Langell, M.H. Nassir, Stabilization of NiO(111) Thin Films by Surface Hydroxyls, J. Phys. Chem. 99 (1995) 4162–4169.
- [130] N. Pineau, C. Minot, V. Maurice, P. Marcus, Density Functional Theory Study of the Interaction of Cl⁻ with Passivated Nickel Surfaces, Electrochem. Solid-State Lett. 6 (2003) B47.
- [131] D. Wolf, Reconstruction of NaCl Surfaces from a Dipolar Solution to the Madelung Problem, Phys. Rev. Lett. 68 (1992) 3315–3319.
- [132] A. Barbier, C. Mocuta, H. Kuhlenbeck, K.F. Peters, B. Richter, G. Renaud, Atomic structure of the polar NiO(111)-p(2x2) surface, Phys. Rev. Lett. 84 (2000) 2897–900.
- [133] C.A. Ventrice Jr., T.H. Bertrams, H. Hannemann, A. Brodde, H. Neddermeyer, Stable reconstruction of the polar (111) surface of NiO on Au (111), Phys. Rev. B. 49 (1994) 5773–5781.
- [134] N. Erdman, O. Warschkow, D.E. Ellis, L.D. Marks, Solution of the p(2x2) NiO (111) surface structure using direct methods, Surf. Sci. 470 (2000) 1–14.

- [135] A. Barbier, C. Mocuta, G. Renaud, Structure, transformation, and reduction of the polar NiO(111) surface, *Phys. Rev. B.* 62 (2000) 16056–16062.
- [136] V. Maurice, H. Talah, P. Marcus, A scanning tunneling microscopy study of the structure of thin oxide films grown on Ni(111) single crystal surfaces by anodic polarization in acid electrolyte, *Surf. Sci.* 304 (1994) 98–108.
- [137] O.M. Magnussen, J. Scherer, B.M. Ocko, R.J. Behm, In Situ X-ray Scattering Study of the Passive Film on Ni(111) in Sulfuric Acid Solution, *J. Phys. Chem. B.* 104 (2000) 1222–1226.
- [138] O.L. Warren, P.A. Thiel, Structural determination of a NiO(111) film on Ni(100) by dynamical low-energy electron-diffraction analysis, *J. Chem. Phys.* 100 (1994) 659–663.
- [139] T. Kendelewicz, P. Liu, C.S. Doyle, G.E. Brown, E.J. Nelson, S.A. Chambers, Reaction of water with the (100) and (111) surfaces of Fe₃O₄, *Surf. Sci.* 453 (2000) 32–46.
- [140] S.C. Petitto, K.S. Tanwar, S.K. Ghose, P.J. Eng, T.P. Trainor, Surface structure of magnetite (111) under hydrated conditions by crystal truncation rod diffraction, *Surf. Sci.* 604 (2010) 1082–1093.
- [141] J.R. Rustad, E. Wasserman, A.R. Felmy, A molecular dynamics investigation of surface reconstruction on magnetite (001), *Surf. Sci.* 432 (1999) L583–L588.
- [142] J.R. Rustad, A.R. Felmy, E.J. Bylaska, Molecular simulation of the magnetite-water interface, *Geochim. Cosmochim. Acta.* 67 (2003) 1001–1016.
- [143] T.K. Kundu, K.H. Rao, S.C. Parker, Atomistic simulation studies of magnetite surface structures and adsorption behavior in the presence of molecular and dissociated water and formic acid, *J. Colloid Interface Sci.* 295 (2006) 364–73.
- [144] J. Ahdjoudj, C. Martinsky, C. Minot, M.A. Van Hove, G.A. Somorjai, Theoretical study of the termination of the Fe₃O₄ (111) surface, *Surf. Sci.* 443 (1999) 133–153.
- [145] G.J. Martin, R.S. Cutting, D.J. Vaughan, M.C. Warren, Bulk and key surface structures of hematite, magnetite, and goethite: A density functional theory study, *Am. Mineral.* 94 (2009) 1341–1350.
- [146] S.K. Shaikhutdinov, Y. Joseph, C. Kuhrs, W. Ranke, W. Weiss, Structure and reactivity of iron oxide surfaces, *Faraday Discuss.* 114 (1999) 363–380.

- [147] A. Barbieri, W. Weiss, M.A. Van Hove, G.A. Somorjai, Magnetite $\text{Fe}_3\text{O}_4(111)$: surface structure by LEED crystallography and energetics, *Surf. Sci.* 302 (1994) 259–279.
- [148] M. Ritter, W. Weiss, $\text{Fe}_3\text{O}_4(111)$ surface structure determined by LEED crystallography, *Surf. Sci.* 432 (1999) 81–94.
- [149] E. Heifets, J. Ho, B. Merinov, Density functional simulation of the $\text{BaZrO}_3(011)$ surface structure, *Phys. Rev. B.* 75 (2007) 155431.
- [150] P. V Kumar, M.P. Short, S. Yip, B. Yildiz, J.C. Grossman, High Surface Reactivity and Water Adsorption on $\text{NiFe}_2\text{O}_4(111)$ Surfaces, *J. Phys. Chem. C.* 117 (2013) 5678–5683.
- [151] A. Wander, I. Bush, N. Harrison, Stability of rocksalt polar surfaces: An ab initio study of $\text{MgO}(111)$ and $\text{NiO}(111)$, *Phys. Rev. B.* 68 (2003) 233405.
- [152] M. Schulze, R. Reissner, Adsorption of water on epitaxial $\text{NiO}(100)$, *Surf. Sci.* 482–485 (2001) 285–293.
- [153] Z. Łodziana, N.-Y. Topsøe, J.K. Nørskov, A negative surface energy for alumina., *Nat. Mater.* 3 (2004) 289–93.
- [154] P. Gumbsch, M. Daw, Interface stresses and their effects on the elastic moduli of metallic multilayers, *Phys. Rev. B.* 44 (1991) 3934–3938.
- [155] D. Walter, B. Collins, V. Petrov, B.K. Kendrick, A. Manera, T. Downar, High-fidelity Simulation of CRUD Deposition on A PWR Fuel Pin with Grid Spacers: A Proof-of-principle Using the Fully-coupled MAMBA/DECART/STAR-CCM+ Code, in: 15th Int. Top. Meet. Nucl. React. Therm., Pisa, Italy, 2013: p. 551.
- [156] V. Petrov, B.A. Kendrick, D. Walter, A. Manera, Impact of 3D Spatial Variations in Fluid Flow on the Prediction of CRUD Deposition in a 4x4 PWR Sub-assembly, in: 15th Int. Top. Meet. Nucl. React. Therm., Pisa, Italy, 2013: p. 543.
- [157] D. Lister, F. Cussac, Modeling of Particulate Fouling on Heat Exchanger Surfaces: Influence of Bubbles on Iron Oxide Deposition, *Heat Transf. Eng.* 30 (2009) 840–850.
- [158] R. V. Zucker, D. Chatain, U. Dahmen, S. Hagège, W.C. Carter, New software tools for the calculation and display of isolated and attached interfacial-energy minimizing particle shapes, *J. Mater. Sci.* 47 (2012) 8290–8302.

- [159] J.D. Nelligan, N. Kallay, E. Matijević, Particle adhesion and removal in model systems, *J. Colloid Interface Sci.* 89 (1982) 9–15.
- [160] D.E. Janney, D.L. Porter, Characterization of phases in “crud” from boiling-water reactors by transmission electron microscopy, *J. Nucl. Mater.* 362 (2007) 104–115.
- [161] S.A. De Waal, E.A. Viljoen, L.C. Calk, Nickel Minerals from Barberton, South Africa: VII Bonaccordite. The Nickel Analogue of Ludwigite, *Trans. Geol. Soc. South Africa.* 77 (1974) 375.
- [162] J. Fernandes, R. Guimarães, M. Continentino, H. Borges, A. Sulpice, J.-L. Tholence, et al., Magnetic interactions in the ludwigite $\text{Ni}_2\text{FeO}_2\text{BO}_3$, *Phys. Rev. B.* 58 (1998) 287–292.
- [163] D.A. Perkins, J.P. Attfield, Resonant powder X-ray determination of the cation distribution in FeNi_2BO_5 , *J. Chem. Soc. Chem. Commun.* 05 (1991) 229–231.
- [164] D. Li, W. Ching, Electronic structures and optical properties of low- and high-pressure phases of crystalline B_2O_3 , *Phys. Rev. B.* 54 (1996) 13616–13622.
- [165] Y. Ishii, J. Murakami, M. Itoh, Optical Spectra of Excitons in Lithium Oxide, *J. Phys. Soc. Japan.* 68 (1999) 696–697.
- [166] G.E. Gurr, P.W. Montgomery, C.D. Knutson, B.T. Gorres, The crystal structure of trigonal diboron trioxide, *Acta Crystallogr. Sect. B Struct. Crystallogr. Cryst. Chem.* 26 (1970) 906–915.
- [167] R.W.G. Wyckoff, *Crystal Structures*, 2nd ed., Interscience, New York, NY, 1963.
- [168] A. Kirfel, G. Will, R.F. Stewart, The chemical bonding in lithium metaborate, LiBO_2 . Charge densities and electrostatic properties, *Acta Crystallogr. Sect. B Struct. Sci.* 39 (1983) 175–185.
- [169] S.F. Radaev, L.A. Muradyan, L.F. Malakhova, Y.A. Burak, V.I. Simonov, Atomic-Structure and Electron-Density of Lithium Tetraborate $\text{Li}_2\text{B}_4\text{O}_7$, *Kristallografiya.* 34 (1989) 1400–1407.
- [170] V. Maslyuk, M. Islam, T. Bredow, Electronic properties of compounds of the $\text{Li}_2\text{O}-\text{B}_2\text{O}_3$ system, *Phys. Rev. B.* 72 (2005) 125101.

[171] U. Engberg, B_2O_3 crystals investigated by plane-wave pseudopotential calculations using the generalized-gradient approximation, Phys. Rev. B. 55 (1997) 2824–2830.

[172] G.M. Anderson, D.A. Crerar, Thermodynamics in Geochemistry The Equilibrium Model, 1st ed., Oxford University Press, New York, NY, 1993.

APPENDIX

Appendix A Effective Chemical Potentials

The effective standard state chemical potentials (ECPs) for the elements are fit to the function:

$$\mu^0(298.15 \text{ K} \leq T \leq 898.15 \text{ K}) \left[\frac{\text{kJ}}{\text{mol}} \right] = A + BT + CT \ln T + DT^2 + E \frac{1}{T} + FT^3. \quad (\text{A.1})$$

The coefficients of Eq. (A.1) were determined using the global fitting procedure for the effective chemical potentials of the elements in their standard states and are given in Table A.1.

Table A.1 Coefficients of Eq. (A.1) are provided to reproduce the effective standard state chemical potentials (ECPs) of the elements determined by the global fitting procedure. Standard state refers to the elements being in their equilibrium phase at the given temperature and pressure. The values are reported for a pressure of 1 Bar.

$\mu^0(T)$	A [kJ/mol]	B [kJ/mol·K]	C [10 ⁻³ kJ/mol·K]	D [10 ⁻⁵ kJ/mol·K ²]	E [kJ·K/mol]	F [10 ⁻⁷ kJ/mol·K ³]
Fe	-542.2234	-3.0562	579.0786	-137.5260	11166.2402	4.6487
Ni	-281.4639	-1.9781	374.1096	-88.6994	7509.7748	2.9938
Zn	-54.9384	-1.9691	371.2403	-85.3290	7512.9363	2.7094
Co	-455.2552	-3.0522	578.3376	-138.9698	11566.9879	4.6488
H ₂	-707.8309	-1.7026	315.5267	-91.5869	13267.8307	3.2427
O ₂	-974.8047	5.1079	-973.6217	214.8372	12378.7410	-6.9730

The aqueous species free energies are reported as *apparent* molal free energies which are defined according to the Benson-Helgeson convention [172]. The change in absolute Gibbs free energy of the component, at any temperature and pressure, from elements (*i*) at their standard state is expressed as:

$$\Delta_a G^0(T, P) = G^0(T, P) - \sum_i G_i^0(T_r, P_r). \quad (\text{A.2})$$

The apparent free energy can be written in terms of the standard free energy of formation and the absolute free energy of a species at a given temperature and pressure using the relationship:

$$\Delta_a G^0(T, P) = \Delta_f G^0(T_r, P_r) + (G^0(T, P) - G^0(T_r, P_r)). \quad (\text{A.3})$$

To convert the apparent to the standard free energy of formation, the free energy of formation at any temperature and pressure is written in terms of the free energy of formation at standard conditions and the change in the absolute free energy of a component and constituent elements from their standard state as

$$\begin{aligned} \Delta_f G^0(T, P) = \Delta_f G^0(T_r, P_r) + (G^0(T, P) - G^0(T_r, P_r)) \\ - \sum_i [G_i^0(T, P) - G_i^0(T_r, P_r)]. \end{aligned} \quad (\text{A.4})$$

Recognizing that the first two terms of Eq. (A.4) are the apparent free energy of formation, the standard free energy of formation is related to the apparent free energy according to:

$$\Delta_a G^0(T, P) = \Delta_f G^0(T, P) + \sum_i [G_i^0(T, P) - G_i^0(T_r, P_r)]. \quad (\text{A.5})$$

This relationship can be used to demonstrate that the free energy of a reaction is identical when using either free energy convention.

Conversion between the two conventions is accomplished using the tabulated Gibbs Energy Function, given in the JANAF tables [112], which are defined as

$$-\left(\frac{G^0(T) - H^0(T_r)}{T}\right) \text{ or } \left(\frac{H^0(T_r) - G^0(T)}{T}\right).$$

The apparent Gibbs free energy for a compound is calculated from the tabulated Gibbs energy function by canceling the enthalpy contribution for each element (i) at the reference temperature such that Eq. (A.5) can be written as

$$\begin{aligned} \Delta_a G^0(T, P) = \Delta_f G^0(T, P) \\ + \sum_i \left[\left(\frac{H_i^0(T_r, P) - G_i^0(T, P)}{T} \right) T - \left(\frac{H_i^0(T_r, P) - G_i^0(T_r, P)}{T_r} \right) T_r \right]. \end{aligned} \quad (\text{A.6})$$

SUPCRT92 [74,75] with the 2007 database does not contain all of the elements in their standard state. The JANAF tables were used to calculate the apparent free energy of formation of the missing elements at standard pressure and throughout the temperature range of interest. In the case of an element at reference pressure, Eq. (A.6)

can be used to find the apparent free energy of formation after recognizing that $\Delta_f G^0(T, P_r) = 0$, by definition, for an element in its standard state. The error between the apparent free energy of formation calculated from the JANAF tables and SUPCRT92 can only be determined for iron, being that it is the only metal in its standard state contained in SUPCRT92's 2007 database that is relevant to this study. The maximum error in the apparent free energy of formation calculated from the JANAF tables and SUPCRT92's 2007 database is less than 0.44% (0.12 kJ/mol) at the maximum temperature.

The standard free energy of formation for each aqueous metal species will be calculated using the definition and the apparent free energy values such that, for charged aqueous species,

$$\begin{aligned} \left(\Delta_f G_{M^{+z}}^0(T, P)\right)_{aq} &= \left(\Delta_a G_{M^{+z}}^0(T, P)\right)_{aq} + \frac{z}{2} \left(\Delta_a G_{H_2}^0(T, P)\right)_g - \left(\Delta_a G_M^0(T, P)\right)_s \\ &\quad - z \left(\Delta_a G_{H^+}^0(T, P)\right)_{aq}. \end{aligned} \quad (A.7)$$

The effective chemical potentials of all aqueous species are fit according to

$$\mu^0(298.15 \text{ K} \leq T \leq 617.15 \text{ K}) \left[\frac{\text{kJ}}{\text{mol}} \right] = A + BT + C T \ln T + DT^2 + E \frac{1}{T} + FT^3. \quad (A.8)$$

The coefficients of Eq. (A.8) are given in Table A.2.

Table A.2 Effective standard state chemical potentials (ECPs) of the aqueous species determined by the global fitting procedure. Coefficients are provided for use with Eq. (A.8). The values are reported for a pressure of 155 Bar.

$\mu^0(T)$ 155 Bar	A $\left[\frac{\text{kJ}}{\text{mol}}\right]$	B $\left[\frac{\text{kJ}}{\text{mol}\cdot\text{K}}\right]$	C $\left[10^{-3}\frac{\text{kJ}}{\text{mol}\cdot\text{K}}\right]$	D $\left[10^{-5}\frac{\text{kJ}}{\text{mol}\cdot\text{K}^2}\right]$	E $\left[\frac{\text{kJ}\cdot\text{K}}{\text{mol}}\right]$	F $\left[10^{-7}\frac{\text{kJ}}{\text{mol}\cdot\text{K}^3}\right]$
$(\text{H}_2\text{O})_l$	-1432.1355	0.3236	-63.2328	1.7607	2795.8512	0.3236
$(\text{H}_2\text{O})_g$	-1423.3658	3.0769	-61.2421	158.4713	-405.2578	-6.2195
Ni_{aq}^{+2}	380.2174	-0.5261	117.7779	-32.0450	-6651.1741	2.8394
Fe_{aq}^{+2}	73.6321	-2.0376	410.5225	-114.4011	-1180.3670	5.9501
Fe_{aq}^{+3}	501.5834	1.7384	-325.9208	122.2772	-19324.4212	-3.2589
Zn_{aq}^{+2}	505.2433	-0.8511	186.2069	-58.5909	-6173.7389	3.8531
Co_{aq}^{+2}	197.7945	-1.8542	373.2061	-101.3680	-1485.7017	5.2453
NiO_{aq}	-933.9167	1.1246	-221.3906	56.9659	-1164.4941	-2.2489
$(\text{H}_2)_{aq}$	-689.7183	3.0386	-614.1494	198.8776	-3884.0976	-9.9899
OH_{aq}^-	-1352.5976	-15.0713	3002.8552	-981.6527	42677.6623	46.0577